The Use of Long-Period Gratings to Detect Sulphur Hexafluoride.

by

Michael Barnes

October, 2007
Johannesburg, South Africa

Declaration

I declare that this research report is my own, unaided work, except where otherwise acknowledged. It is being submitted for the degree of Master of Science in Engineering in the University of the Witwatersrand, Johannesburg. It has not been submitted before for any degree or examination in any other university.

Signed this the ⎽⎽⎽ day of ⎽⎽⎽⎽⎽⎽⎽⎽⎽⎽⎽ 2007.

⎯⎯⎯⎯⎯⎯⎯⎯⎯⎯⎯⎯⎯⎯⎯⎯⎯⎯
Michael Robert Barnes

Abstract

The combination of the increase in cost of Sulphur Hexafluoride ("SF$_6$"), the registration of SF$_6$ as a greenhouse gas and the use of SF$_6$ at pressures above atmospheric has caused the need for SF$_6$ detection equipment to arise. This research report outlines and reviews past and present technologies utilised, together with presently available commercial systems. Along with the review of available technologies, a proposed system utilising opto-electronic sensors to provide real-time detection is discussed.

The proposed method investigated is the utilisation of Long-period gratings to detect slight refractive index changes of the ambient environment outside gas insulated systems and attempt to resolve the change in refractive index into detection mechanism for SF$_6$.

The method is shown to be possible, however currently not practically feasible. It is recommended that a practical investigation be undertaken to determine the real practical constraints theorised within but the magnitudes not yet established.

Contents

List of Figures

vi

List of Tables

List of Symbols and Abbreviations

SF_6	Sulphur Hexafluoride
GIS	Gas Insulated Systems/Substations
GIL	Gas Insulated Lines
n_1	Refractive index of the optic fibre core
n_2	Refractive index of the optic fibre cladding
a_1	Radius of the optic fibre core
a_2	Radius of the optic fibre cladding
LD	Laser Diode
λ	Wavelength
f	Frequency
c	Velocity of light in a vacuum
LIDAR	Light Detection and Ranging
DIAL	Differential absorption light detection and ranging
FTIR	Fourier Transform Infrared
N_{min}	Minimum detectable concentration
APL	Absorption Path Length
PBF	Photonic Bandgap Fibre
β	Propagation constant
ω	Angular frequency
n	Effective index of refraction
k	Free space propagation constant
κ	Cross coupling coefficient
Δ	Phase mismatch
Λ	Perturbation period
$\Delta\beta$	Differential propagation constant
δ	Detuning parameter
P_0	Incident power
n_{cl}	Effective index of the cladding
LPFGs	Long period fibre gratings
SMF	Single mode fibre
FBGs	Fibre Bragg Gratings
DSF	Dispersion shifted fibre
$\frac{\delta}{\kappa}$	Detuning ratio

Chapter 1

Introduction

Two basic human needs are energy and communication and as populations expanded, cities grew and industrial production expanded, the need for both commodities grew. While communication distances lengthened and data volumes grew exponentially, the requirements for energy and power were to provide compact substations within crowded cities and cramped environments.

Solutions for communications growth were to replace wire pairs with coaxial cables and develop microwave communication systems but eventually the costs exceeded the benefits and microwave systems reached their inherent limitation. This led to the development of optical communication systems.

In order to meet the requirements of compact power distribution substations, gas insulated substations and systems ("GIS") and gas insulated transmission lines ("GIL") were developed. Initially these systems and transmission lines were filled with pure Sulphur Hexafluoride ("SF_6") but advancements have led to the utilisation of gas mixtures of SF_6 and Nitrogen and the gas mixtures have been shown to perform as well as pure SF_6[1, 2].

1.1 Introduction to Fibre Optics

Today light has an information carrying capacity 10000 times than that of radio frequency communication systems. It also has the benefit of being immune to electrical and magnetic interferences and so the comparative bit error rate of optical communication systems are very low.

An optic fibre can be described by a simple three layer model as shown in Figure 1.1. A standard coating employed in the production of optic fibre is epoxy acrylate to provide stiffening and protection to the brittle silica fibre core and cladding.

1.1.1 Types of Optic fibres

Although hundreds, if not thousands, of different types and forms of fibres exist, most can be divided into two main categories of construction:
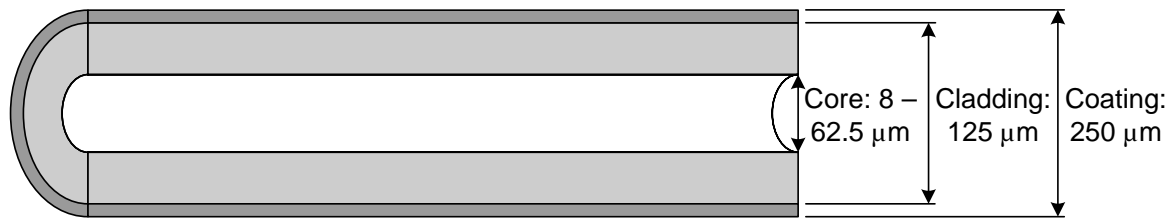
Figure 1.1: The three layer composition of an optical fibre together with typical dimensions

1. A step index fibre.

2. A graded index fibre.

Each of the above categories can be further divided into two types of fibre relating to the relative bandwidth transmission capability, namely:

1. A single-mode fibre.

2. A multi-mode fibre.

Step Index Fibre

A step index fibre has a step change in refractive index between the core and the cladding where the core refractive index, n_1, is greater than the cladding refractive index, n_2. This results in transmission down the length of the fibre utilising total internal reflection, as shown in Figure 1.2. Figure 1.2 also displays a graphical representation of a fibre profile and a typical refractive index profile.
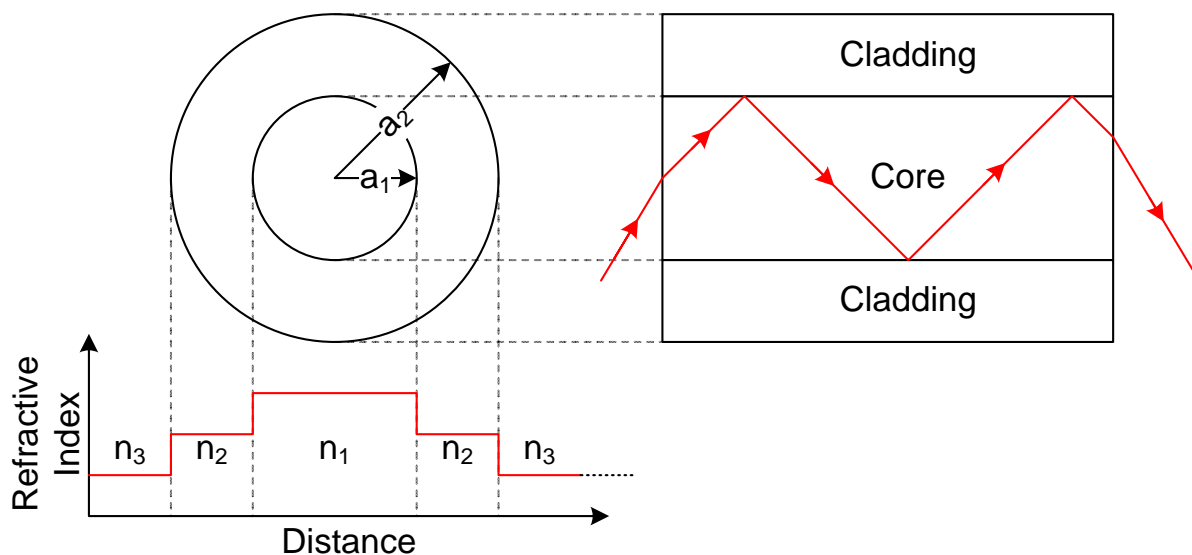
Figure 1.2: An optical fibre profile with dimension definitions, a typical refractive index profile and a profile displaying typical transmission by total internal reflection

Graded Index Fibre

A graded index fibre has a only one type of glass, as opposed to two, in a step-index fibre, but it is treated so that the index of refraction gradually decreases as the distance from the core increases. The result of this construction is that light continuously bends toward the center of the fibre much like a continuous lens.

Single and Multi-mode Fibres

Single and multi-mode fibres refer to the acceptance angle of a fibre, which is related to the radius of the fibre core. Figure 1.3 illustrates two rays of light (modes), M1, which enters the fibre parallel to the fibre core or at a slight angle, and M2 which enters the fibre at an angle close to the maximum acceptance angle. As a result of the entry angle, M1 has a shorter path length than that of M2.
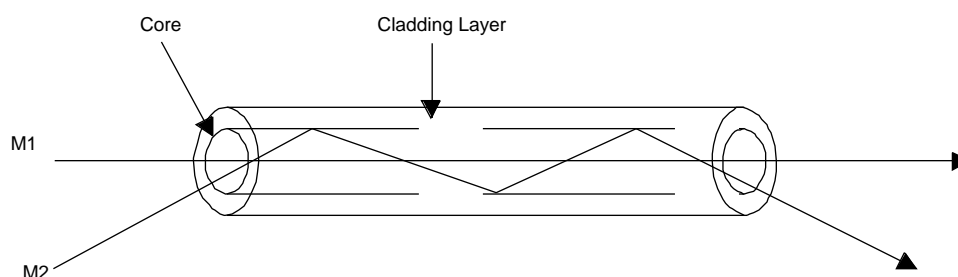
Figure 1.3: The bandwidth of an optical fibre is related to the acceptance angle of the fibre and different path lengths of modes

Figure 1.4 shows how, as the angle of the mode entry changes, the transmission path is altered, until the mode is either refracted into the cladding and lost, or the mode is reflected away from the fibre. Mode three demonstrates the first effect and mode four demonstrates reflection. The maximum angle at which a mode is still transmitted through the fibre is termed the maximum acceptance angle. One can see how as the radius of the fibre is increased so is the maximum acceptance angle.

A single-mode fibre has a smaller radius core and hence only transmits a single mode through the fibre while other modes are diffracted into the fibre cladding. Multi-mode fibres have larger cores and so transmit more modes. One can see from Figure 1.4 that the path lengths of transmitted modes differ and as a result of the differing path lengths of the modes, different modes of light reach the end of fibre at different times, even though the original source is the same light emitting diode (LED) or laser diode (LD). Typical dimensions of single mode fibres are core diameters of 8 to 10 μm whereas multi-mode fibres have diameters in the region of 50 to 62,5 μm.

1.2   Introduction to Sulphur Hexafluoride

A paper appearing in a journal of physics dedicated to atomic, molecular and optical physics states the following concerning Sulphur Hexafluoride (SF_6):
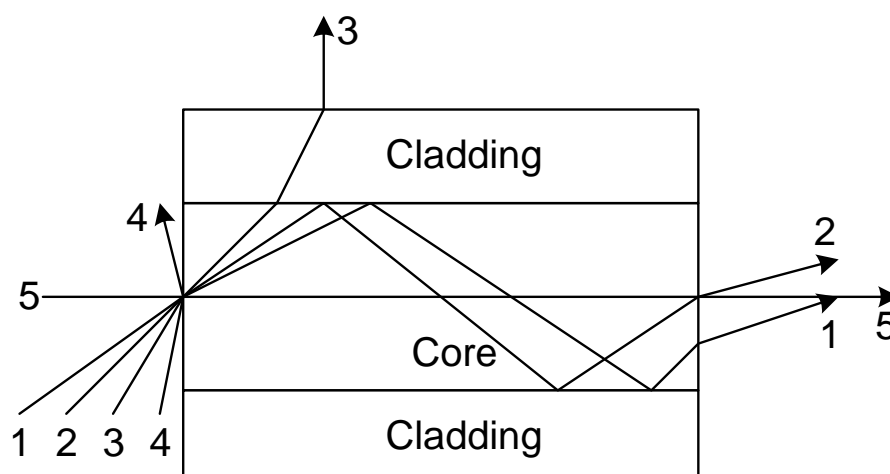
Figure 1.4: Maximum acceptance angle of a fibre is related to the radius of the fibre. Mode 1 and 2 demonstrate two paths of transmission, mode 3 a refracted and lost mode, mode 4 a reflected mode and mode 5 transmitted without any refraction. The maximum acceptance angle, in this case, would lie between mode 2 and 3

> "*From an academic point of view, the molecular structure of SF_6 shows fascinating characteristics due to its octahedral symmetry. Its double-well potential and shape resonances have become a challenge to and a test bench for molecular physicists. Thus, SF_6 has been and still is an object of many diverse studies.*"[3]

This statement sets the tone for the investigation into an SF_6 leak detection system and demonstrates how the molecule poses challenges to scientists and high voltage engineers alike. Some of the so called "fascinating characteristics" include: a molecular compound which is gaseous even at low temperature, chemically inert, non-flammable, non-toxic, non-corrosive and has a high dielectric strength through Fluorine's high electronegativity[4, 5, 6]. It also possesses arc quenching properties, high molar heat capacity, low viscosity and good heat transfer capabilities[6].

All these advantages make it an excellent dielectric gas for high voltage gas insulated systems (GIS) where it is utilised at pressures above atmospheric pressure. The use of the gas at pressures above atmospheric pressure ensures a minimal mean free path for free electrons and thus maximises the electron attachment capability of the gas[7, 8, 9].

SF_6 is regarded as a greenhouse gas[10] and the release of it into the atmosphere is not only illegal but also contributes to global warming. To maintain pressure integrity and to minimize atmospheric pollution, leaks in existing GIS must be minimised, if not entirely eradicated and so cost and accuracy of leak detection technologies are of the utmost importance. Appendix A details why SF_6 is regarded as a better insulator than air and also provides an in-depth understanding of breakdown mechanisms in air and SF_6.

1.2.1   SF$_6$ Absorption Characteristics

At this point the absorption characteristics of SF$_6$ must be briefly mentioned. SF$_6$ does not possess any absorption bands in the visible region of the electromagnetic spectrum between 400 and 700 nm[11]. A strong peak of absorption of SF$_6$ is recorded at 10,55 μm (947 cm^{-1}) and a weak absorption is recorded near 16 μm (666, 67 cm^{-1})[12, 13, 14].

Figure 1.5 shows a published absorption spectrum of SF$_6$ and one can see the absorption peak at 10,55 μm and a lesser peak near 16 μm. Figure 1.6 shows more detail of the absorbtion peak near 10,55 μm.
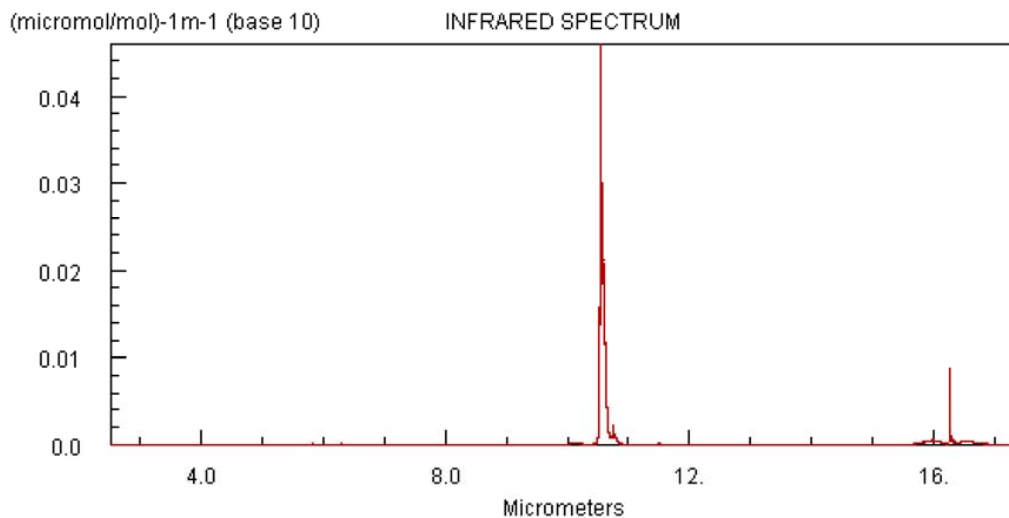
Figure 1.5: The absorption spectrum of SF$_6$ between 3 and 17 μm[14]
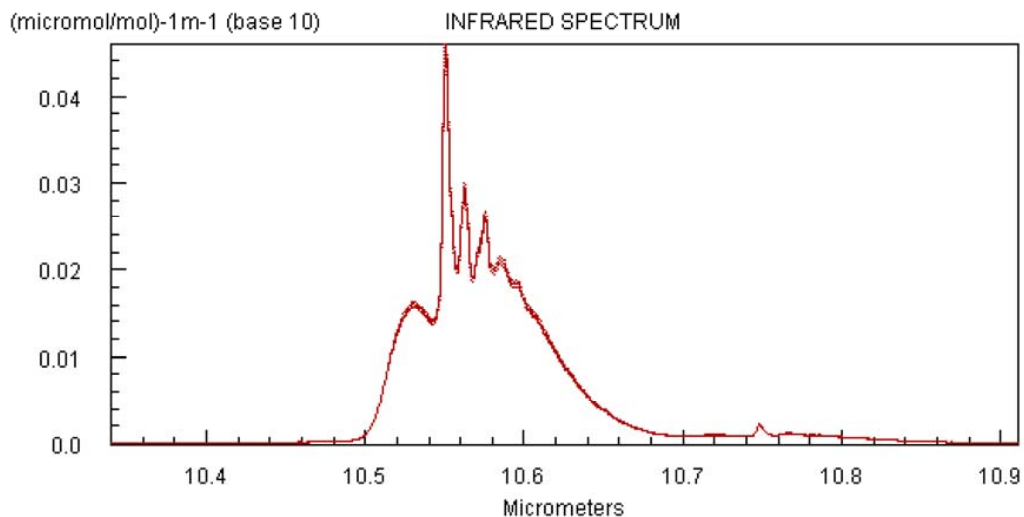
Figure 1.6: The absorption spectrum of SF$_6$ between 10,4 and 10,9 μm[14]

1.3 SF$_6$ Detection Methods

As SF$_6$ is chemically very inert, molecular detection through chemical reaction cannot be utilised and laser induced fluorescence in the visible or UV cannot be used due to a lack of absorption bands of SF$_6$[11]. Further research indicated that other laser based techniques are possible and include[11]:

1. Differential absorption light detection and ranging ("DIAL").

2. Raman Light Detection and Ranging ("Raman LIDAR").

3. Passive Remote Fourier Transform Infrared ("FTIR") spectroscopy.

4. SF$_6$ Fluorescence.

1.3.1 DIAL

This is an acronym for differential absorption LIDAR, where LIDAR is analogous to RADAR and stands for light detection and ranging. Prior to discussing DIAL an introduction to LIDAR is provided.

LIDAR uses a pulsed laser as the light emitting source and senses the presence and distance of gaseous molecules. The presence of the gaseous molecules is detected through the absorption of the emitted light by registering the intensity of the return signal[11]. The distance from the source is calculated through the time of the return signal[11]. A LIDAR system is thus made up of the following components: a powerful pulsed laser, a large aperture receiver and a detector to register the intensity of the returned signal.

While utilising LIDAR light could either be absorbed by molecules (the aim of the system) or the signal can be diminished through scattering by particles in the atmosphere. The latter effect renders LIDAR system ineffective and led to the development of DIAL.

DIAL both circumvents the problem of particle scattering of light and provides the capability of quantitative determination of gas concentrations[11]. The DIAL systems differs from LIDAR in that the return signal intensity is measured at two wavelengths, differing slightly so as to represent the signal at the peak of the absorption feature as well as the wing of the absorption line[11].

The principle behind the system is that it corrects for broadband extinction in the vicinity of the absorption line caused by particle scattering. A second modification is that the returned signal is evaluated at two distances from the site of evaluation which enables the molecular concentration to be evaluated in the range between the two positions[11].

In terms of the evaluation of the minimum detectable concentration (N_{min}) of SF$_6$, the dependent variable is the absorption path length ("APL") and for an APL of 10 cm in

the atmosphere N_{min} is approximately 1,5 ppm[11]. A 10 cm APL will, however, not generate sufficient backscatter signal and the minimum APL for a typical 100 ns pulsed CO_2 laser is 15 m[11]. This situation means that although the absorption is due to a gas column of 10 cm, the return signal from backscattering is due to a column of air 15 m long which decreases the sensitivity of the detection method by a factor of 150. The resulting minimum detectable concentration is in the region of 225 ppm and so the method is not suitable for specific leak detection although the method is employed in long range detection of chemical agents in the atmosphere[11].

1.3.2   Raman LIDAR

Raman LIDAR relies on the principles first identified by CV Raman in 1926 whereby scattering of light incident on molecules results in inelastic scattering at a series of wavelengths[11]. The series of wavelengths on the lower energy side of the exciting radiation are called Stokes shifted frequencies and it is these frequency shifts that enable the method to be used to detect the presence of molecules because the frequency shifts are equal to the vibrational-rotational frequencies of the individual molecules[11]. The intensity of the scattered wave can also be used to determine the concentration of the molecules.

Individual molecular vibrational-rotational frequencies determined through experimental differential scattering have been published including wavelength shifts for SF_6 as 12,95 μm[11]. There is a risk does exist that side band rotational frequency shifts of other molecules, or other vibrational frequencies, overlap with primary frequency shifts of SF_6, but it was found that it is only endangered by the NO_2 line at 13,39 μm and so impact can be avoided by utilising a spectral bandpass filter of smaller than 0,44 μm[11].

The method unfortunately still requires laser excitation of the gases and so the equipment is large and expensive and does not promote a continuous monitoring system due to a continuous monitoring system requiring multiple lasers to scan entire GIS or GIL installations.

1.3.3   Passive Remote FTIR Spectroscopy

Passive remote FTIR utilises the environmental radiation received by a detector and is measured and analysed for specific absorption or emission characteristics[11]. The sensitivity of the measurement technique decreases with the temperature difference between the background and the analytical compound due to background radiation from thermal radiation of any source.

Besides the disadvantage of the dependence on temperature differences between the analytical compound and background temperature, the method also has a problem in that spectral "fingerprints" of molecules may suffer from interferences from other atmospheric gases such as water vapour, ozone or carbon dioxide[11].

1.3.4   SF$_6$ Fluorescence

This method relies on detection through laser induced fluorescence at specific wavelengths. For fluorescence to occur there must be absorption of energy from a laser at the absorption band of the molecule and SF$_6$ does exhibit strong absorption in the vacuum ultraviolet("UV") region of the optical spectrum[11]. This region is inaccessible to commonly used lasers and excitation in this region of the spectrum is absorbed by Oxygen, Nitrogen and water vapour occurring in the atmosphere[11].

These observations rule out detection possibility through fluorescence in the UV and visible region of the spectrum. Another absorption feature exists at 10.5 μm but measurements in this region are impractical mainly due to low values of transition probability in the far infrared ("IR") which would result in the excitation being totally quenched through molecular collisions with atmospheric gases prior to spontaneous emission taking place[11].

1.3.5   Commercially Available Instruments

There does not seem to be commercial instrument utilising the DIAL method of detection available for for SF$_6$ detection. However, since DIAL relies on the tailoring of the instrument for a specific gas detection, and a working system is usually constructed by the user, the possibility of existence of detectors utilising the method cannot be ruled out.

Raman LIDAR, the same laser wavelength is used for all analytes and changing from one gas detected to another involves switching filters in front of the detector. Notwithstanding this fact Raman LIDAR applications are rarely utilised and once again commercial systems do not seem to be available for the detection of SF$_6$.

Passive FTIR systems are commercially available and two specific products are discussed below.

Block Engineering SF$_6$ Camera

The Block Engineering SF$_6$ camera provides a 10×14 degree field of view, can be used against machinery, sky or terrain backgrounds, can be used at ranges from 1,8 to 30 m and is claimed to be able to detect leaks as small as 0,45 kg per year[15]. As molecular weight of SF$_6$ is 146,06 g[14] 0,45 kg per year equates to 3,08 moles of gas per year.

The system locates gross leakage quickly but pinpointing the location of leaks within a few centimetres would need to be performed using alternative instruments once the general location of the leak was known. Such an apparatus costs approximately R1 million.

Bruker Instrument

Bruker Optics produces the OPAG 22 which is an automated broadband infrared detection system for the real-time remote sensing of hazardous atmospheric compounds[16]. The instrument provides analysis in less than 1 s and internal calibration sources provide

self-test and self-calibration[16].

The field of view of the OPAG 22 is approximately the same as the Block camera although the Block camera measures the field simultaneously, the OPAG has to cover the same area in 140 consecutive measurements[15, 16, 11]. A recent quote placed the cost of this instrument at approximately R600 000.

1.3.6 Possible Novel Detection Techniques

Random Hole Fibres

In contrast to conventional telecommunications-grade optical fibres, which rely on a compositional difference between the core and cladding regions to confine light to the central core, in random-hole optical fibres ("holy fibres") light is confined to the central core region of the fibre through a refractive-index difference produced by the porosity in the cladding region[17].

Gas molecules have a number of characteristic vibrational absorption bands in the near-IR region, corresponding to the transmission window for silica optical fibre. The sensors utilise evanescent-wave absorption in random-hole optical fibres and the presence of the gas molecules in the holes of the fibre appears as a loss at wavelengths that are characteristic of the specific gas species present in the holes[17].

A tunable laser source is used to interrogate the random-hole fibre sensor within the optical transmission range of silica and around the expected absorption peak of the gas being sensed. In the case of acetylene, with an absorption peak at 1530 nm the laser sourced would be scanned from 1520 to 1570 nm and the attenuation as a function of wavelength would be detected. Other gas absorption peaks and there associated absorption bands are shown in Table 1.1.

A major limitation of these sensors is the rate of diffusion of gas into the holes of the fibre. This limitation can be overcome by increasing the number and size of the holes and also as the gas penetration into the fibre is expected to be governed by gas phase diffusion kinetics, the rate of penetration will be exponentially dependent on temperature[17].

Photonic Bandgap Fibres

In a photonic bandgap fibre ("PBF") the light is confined within the air core by a two-dimensional photonic bandgap formed by the periodic structure of the cladding allowing transmission over a limited wavelength range[18]. As this method also relies on the gas species possessing an absorption band in the optical transmission range of silica, gases which do not possess absorption spectra within the 1500 to 1800 nm range cannot be detected using this method.

In order to minimise the response time of the sensor the fibre length should be as short as possible while still long enough to provide a sufficient signal. The optimal length depends on the molecular species to be monitored and the amount of gas present. For gases with

Table 1.1: Molecular species with absorption bands in the near-IR region[17]

Molecule	Absorption Peak (nm)
O_2	761
NO_2	800
HF	1330
HBr	1341
H_2O	1365
C_2H_2	1530
HI	1541
NH_3	1544
CO	1567
CO_2	1573
H_2S	1578
CH_4	1651
HCl	1747

weak absorption lines or in low concentration, an increased sensitivity can be achieved by using a longer fibre. However, the attenuation increases with the length of the fibre.

A further constraint on the use of PBFs for gas species detection is the limited wavelengths that PBFs are currently available in which are a range between 400 and 2550 nm with varying losses. This range could be extended by utilising special compound glasses that are transparent in the mid infrared range.

Conclusions with respect to SF$_6$ detection

In terms of both of the above mentioned methods their use for the detection of SF$_6$ is not possible due to the position of the absorption peaks. To the best of the authors knowledge, and research to date, the absorption peaks of SF$_6$ are at approximately 10,5 and 16,6 μm respectively[1, 2, 11, 14](Also refer to Section 1.2.1). Both of these absorption peaks are well above the optical transmission spectrum of silica and so also do not meet the requirements for the above mentioned methods and so these methods cannot be utilised.

1.4   Research Objectives

The objective of the research report is two-fold:

1. To provide the reader with an in-depth analysis of the properties of photo induced long-period gratings and their applications as fibre optic sensors.

2. To provide an analysis and design of a fibre optic sensor system to detect SF$_6$ leaking from GIS or GIL installations.

Item 1 also involves providing the reader with a basic introduction to fibre optic technology and terminology in order to assist the reader in understanding the in-depth analysis

of the gratings. The research report does not attempt to present a working system but rather a design for future implementation.

Chapter 2

Fundamentals of Long-Period Gratings

2.1 Introduction

This Chapter will describe long-period gratings (LPGs), their uses, advantages and disadvantages, a mathematical understanding will be derived and lastly a mathematical model developed to model the gratings.

2.2 Definition

A long-period grating is difficult to define comprehensively in a single sentence but in its simplest form it is a device created through a periodic modification of the refractive index of the fibre core which causes light to couple from the core to the cladding[19, 20]. It typically has a length of 2.5 cm and the periodic modification of the core has a periodicity of between 100 μm and 1 mm[19, 20].

The refractive index of the core can be modified in different ways (Discussed in Section 4.1) but usually through ultra-violet ("UV") exposure of a single mode optical fibre[20]. Typically the modulation depths induced through UV exposure are of the order of 100 μm. The core-cladding coupling caused through the grating fabrication results in discrete wavelength attenuation bands based on the physical properties of the grating[19].

The above mentioned fundamental concepts will be expanded upon and explained in subsequent sections and chapters.

2.3 Guided, Radiation and Cladding Modes

A mode in an optical fibre is a set of electromagnetic waves that participates in the propagation of energy in the fibre[21]. A finite number of guided modes travel in the fibre with discrete propagation constants (β) that are functions of the optical source

wavelength and fibre parameters[21]. Recall:

$$k = \frac{2\pi}{\lambda} \tag{2.1}$$

$$\text{and } c = f\lambda \tag{2.2}$$

$$\therefore \frac{f}{c} = \frac{1}{\lambda} \tag{2.3}$$

$$\text{and } \omega = 2\pi f \tag{2.4}$$

$$\text{and } \beta = \frac{\omega n}{c} \text{ where: } n_2 < |n| < n_1 \tag{2.5}$$

$$\text{Substituting 2.4 into 2.5 } \therefore \beta = \frac{2\pi f n}{c} \tag{2.6}$$

$$\text{Substituting 2.3 into 2.6 } \therefore \beta = \frac{2\pi n}{\lambda} \tag{2.7}$$

Where:
- λ is the wavelength of light
- k is the free space propagation constant at wavelength λ
- c is the velocity of light in a vacuum
- f is the frequency of the light
- ω is the angular frequency
- β is the propagation constant
- n is the effective index of refraction ($n_2 < |n| < n_1$)
- n_1 is the refractive index of the core
- n_2 is the refractive index of the cladding

It can be shown that the discrete values of propagation constants for the guided modes are confined to[21]:

$$n_2 k < |\beta| < n_1 k \tag{2.8}$$

Figure 2.1 shows the propagation constants of the forward-propagating ($\beta > 0$) and reverse-propagating ($\beta < 0$) guided modes as functions of the optical frequency. The simple pictorial representation of the modal propagation constants in terms of the angular frequency is termed a β-plot[22].
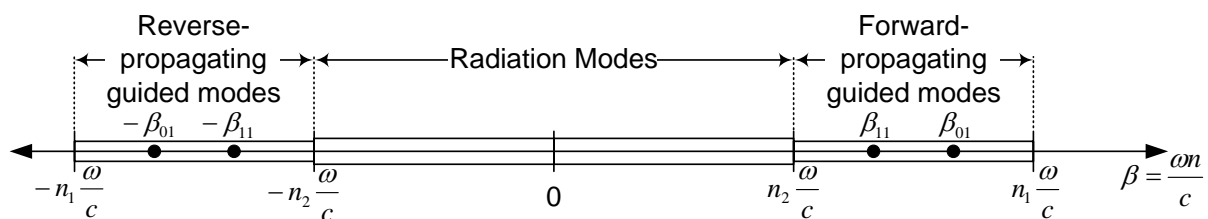
Figure 2.1: Propagation constants of the forward and reverse-propagating guided modes in an optical fibre. β_{01} and β_{11} are the propagation constants of the two lowest order forward-propagating guided modes. Also represented are the propagation constants of radiation modes[22].

Further analysis of Maxwell's equations using related boundary values reveals that another set of modes exist besides the guided modes. These modes are termed the radiation

modes and owing to the presence of waveguide imperfections, result in continuous loss of power from the guided modes[21]. Radiation modes can be simply described as modes which are not guided by the fibre. The radiation modes are also shown in Figure 2.1.

In order to conduct a simplified analysis of guided modes, the fibre cladding is assumed to extend to infinity[21]. As the guided modes have a rapidly decaying field outside the core and retain insignificant values of these fields at the outer boundary of the cladding, the assumption is justified. This assumption is not, however, justified when analysing radiation modes due to the fact that radiation modes extend to infinity and are strongly influenced by the outer cladding boundary[21]. Some of the radiation modes become trapped by the cladding due to the reflection at the outer cladding boundary and termed cladding modes. If we define n_3 as the index of medium surrounding the cladding, then the cladding mode propagation constants are bounded by:

$$n_3 k < |\beta| < n_2 k \tag{2.9}$$

Like the guided modes, cladding modes may travel in either forward or reverse direction and possess discrete propagation constants which are shown in a β-plot in Figure 2.2. Cladding modes attenuate rapidly due to bends in the fibre, scattering losses and absorption by the fibre jacket. The coupling between guided modes to discrete cladding modes forms the basic operating mechanism of fibre gratings.
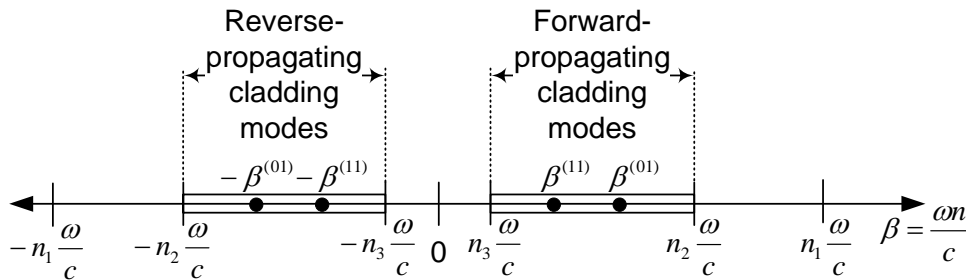
Figure 2.2: Propagation constant distribution of cladding modes in an optical fibre. $\beta^{(01)}$ and $\beta^{(11)}$ are the propagation constants of the two lowest order forward-propagating cladding modes[21].

The coupling of guided modes can result in either co-directional coupling, in which the cladding modes travel in the same direction as the guided modes, or counter-directional coupling, in which the cladding modes travel in the opposite direction to the guided modes from which they couple. This distinction forms the fundamental difference between Bragg or short-period gratings, which utilise counter directional mode coupling, and long-period gratings, which utilise co-directional coupling. Due to this project relying on long-period grating sensors further discussion toward coupling will be limited to co-directional coupling except for instances where understanding of concepts can be enhanced through descriptions of Bragg grating phenomenon.

2.3.1   Co-directional Coupling

The aim of this section is to arrive at solutions to coupled mode equations for two modes propagating in the same direction, under the influence of a periodic perturbation. Also emphasized is the use of coupled mode equations to depict the importance of the phase matching condition between the two modes in order for significant exchange of power to take place.

Consider an optical fibre that is disturbed by a perturbation of period λ along the fibre axis, originating at $z = 0$ and terminating at $z = L$. This perturbation could be caused by a periodic variation in the core index such as a refractive index grating or bends in the fibre. Next we consider two modes, denoted by a_1 and a_2, traveling in the -z direction such that[23]:

$$a_1(z, t) = A_1(z)e^{j(\omega t - \beta_1 z)} \tag{2.10}$$

$$a_2(z, t) = A_2(z)e^{j(\omega t - \beta_2 z)} \tag{2.11}$$

Where: β_1 is the discrete propagation constant of mode a_1
$\quad\quad\quad\quad\;\; \beta_2$ is the discrete propagation constant of mode a_2
$\quad\quad\quad\quad\;\; \omega$ is the angular frequency
$\quad\quad\quad\; A_1(z)$ is the complex normalised amplitude of mode a_1
$\quad\quad\quad\; A_2(z)$ is the complex normalised amplitude of mode a_2.

The presence of a disturbance or irregularity causes the two modes to exchange energy such that A_1 and A_2 become functions of the propagating distance. The objective of couple mode theory is to relate the variation in A_1 and A_2 to a function of z. By utilising the slowly-varying approximation to neglect the effect of second order derivatives of the complex amplitudes and integrating over the fibre cross section one obtains two coupled, first order differential equations[23]:

$$\frac{dA_1(z)}{dz} = \kappa_{12}A_2(z)e^{-j\Delta z} \tag{2.12}$$

$$\frac{dA_2(z)}{dz} = \kappa_{21}A_1(z)e^{+j\Delta z} \tag{2.13}$$

Where: κ_{12} and κ_{21} are termed the cross coupling coefficients, and
$\quad\quad\quad\quad\;\; \Delta$ is the phase mismatch between the propagating modes.

In Equations 2.12 and 2.13 above, Δ is typically the difference in the mode propagation constants[23] and can be modified to:

$$\Delta = \beta_1 - \beta_2 - \frac{2\pi}{\Lambda} \tag{2.14}$$

Where: Λ is the perturbation period.

Since both β_1 and β_2 are functions of frequency, the phase mismatch also has a strong spectral dependence. Ideally Δ should be zero to enable the synchronous transfer of power between the two modes[23] and so using Equation 2.14, one obtains what is commonly

termed the phase-matching condition between the two modes:

$$\Delta\beta = \beta_1 - \beta_2 = \frac{2\pi}{\Lambda} \tag{2.15}$$

Where: $\Delta\beta$ is the differential propagation constant of the two modes.

The total power carried by modes a_1 and a_2 is given by $|A_1(z)|^2$ and $|A_2(z)|^2$, respectively and since, in a lossless system, there is no variation in the total power in the z direction, Equations 2.12 and 2.13 can be manipulated to obtain[23]:

$$\kappa_{12} = -\kappa_{21}^* \tag{2.16}$$

Where: * denotes the complex conjugate.

If one assumes that only mode a_2 carries power at $z = 0$ then one obtains the following boundary conditions:

$$a_1(0) = 0 \tag{2.17}$$
$$a_2(0) = A \tag{2.18}$$

These boundary conditions can be used to solve the coupled mode equations and thus the complex modal amplitudes can be written as[23]:

$$A_1(z) = A\frac{2\kappa_{12}}{\sqrt{4\kappa^2 + \Delta^2}}e^{-j\left(\frac{\Delta z}{2}\right)}sin\left[\frac{1}{2}\left(\sqrt{4\kappa^2 + \Delta^2}\right)z\right] \tag{2.19}$$

$$A_2(z) = Ae^{j\left(\frac{\Delta z}{2}\right)}\left\{cos\left[\frac{1}{2}z\sqrt{4\kappa^2 + \Delta^2}\right] - j\frac{\Delta}{\sqrt{4\kappa^2 + \Delta^2}}sin\left[\frac{1}{2}z\sqrt{4\kappa^2 + \Delta^2}\right]\right\} \tag{2.20}$$

Where: $\kappa^2 = |\kappa_{12}|^2$.

The eigenmodes can now be obtained by substituting the values of the complex amplitudes $A_1(z)$ and $A_2(z)$ into Equations 2.10 and 2.11. The power in the two modes is given by[23]:

$$P_1(z) = |A_1(z)|^2 = P_0\left\{\frac{sin^2\left[\kappa z\sqrt{1 + \left(\frac{\delta}{\kappa}\right)^2}\right]}{1 + \left(\frac{\delta}{\kappa}\right)^2}\right\} \tag{2.21}$$

$$P_2(z) = |A_2(z)|^2 = P_0\left\{\frac{cos^2\left[\kappa z\sqrt{1 + \left(\frac{\delta}{\kappa}\right)^2}\right] + \left(\frac{\delta}{\kappa}\right)^2}{1 + \left(\frac{\delta}{\kappa}\right)^2}\right\} \tag{2.22}$$

Where: δ is termed the detuning parameter with $\delta = \frac{\Delta}{2}$
P_0 is the incident power in eigenmode a_2 ($P_0 = P_2(0) = |A|^2$)
$\frac{\delta}{\kappa}$ is the detuning ratio.

From Equations 2.21 and 2.22 one can see that the two modes have sinusoidal variations in propagating power and the frequency and magnitude of power coupling is a function

of the detuning ratio[23]. Figures 2.3 and 2.4 depict the variation in the normalised incident power values of $P_1(z)$ and $P_2(z)$ as functions of κz for two different values of the detuning ratio. From Figure 2.3 one observes that under the phase-mismatch condition, mode coupling is small and becomes negligible for $\frac{\delta}{\kappa} > 1$. One can also see that for the phase-matching condition, Equations 2.21 and 2.22 can be modified to yield:

$$P_1(z) = P_0 sin^2(\kappa z) \qquad (2.23)$$
$$P_2(z) = P_0 cos^2(\kappa z) \qquad (2.24)$$
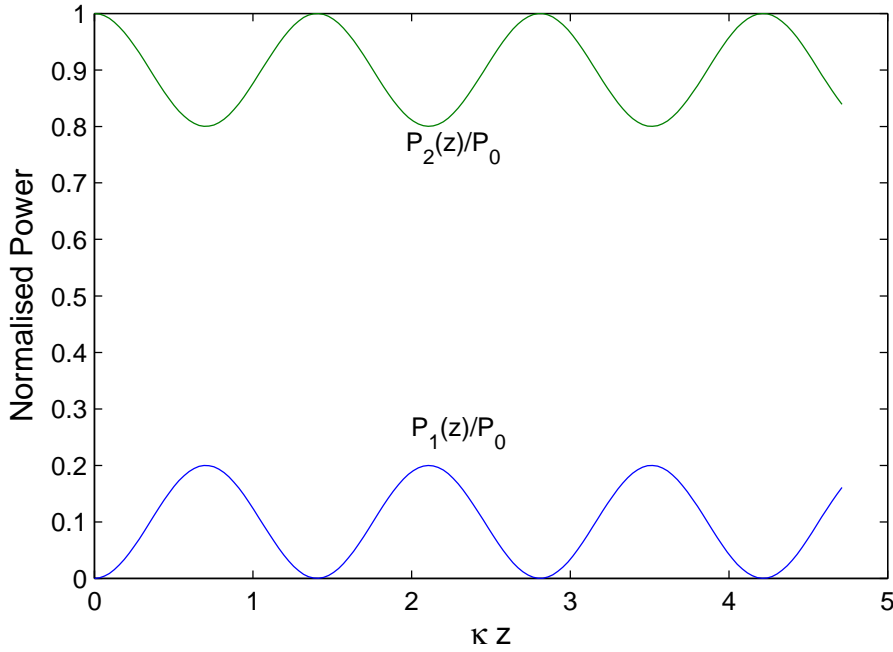
Figure 2.3: Variation of the power of the two co-propagating eigenmodes a_1 and a_2 involved in coupling for a phase-mismatched case ($\frac{\delta}{2} = 2$). The values are normalised to the incident power in mode a_2 ($P_2(0) = P_0$).

In this section the coupling between the two co-propagating modes in the presence of a perturbation was analysed. The power transfer was shown to be dependent on the degree of phase-matching between the modes and the power variation along the propagating direction was shown to be sinusoidal for the two modes.

2.3.2   Guided Mode Coupling Using Long-Period Gratings

In certain applications the need arises to couple light from the LP_{01} mode to other forward-propagating guided modes. This section outlines the operation and applications of gratings that implement the transformation of one guided mode to another.

Figure 2.5 is a β-plot depicting the mode-coupling mechanism between two forward-propagating guided modes. Since the differential propagation constant ($\Delta\beta$) is small in this case, large values of the grating periodicity are required to satisfy the phase-matching
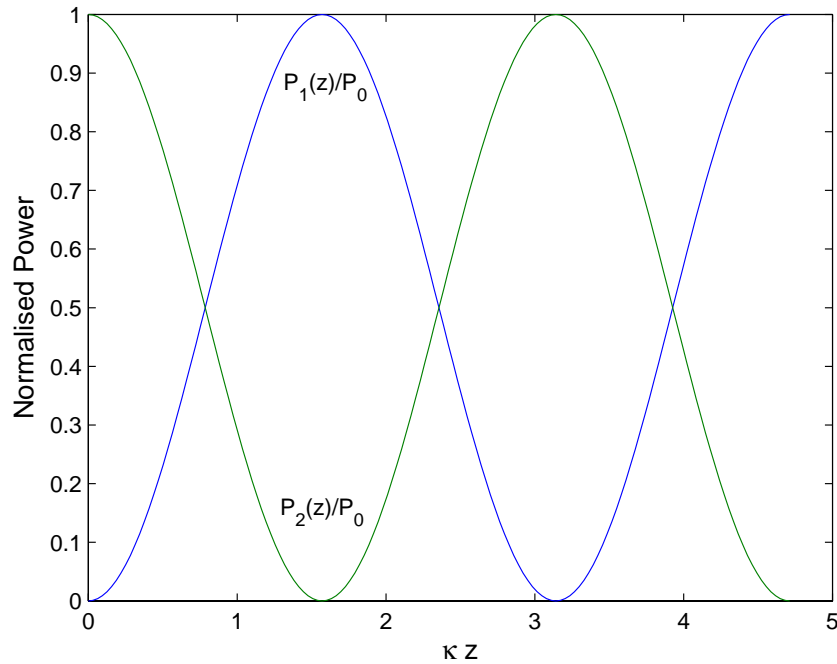
Figure 2.4: Variation of the power of the two co-propagating eigenmodes a_1 and a_2 involved in coupling for a phase-matched case ($\frac{\delta}{2} = 0$). The values are normalised to the incident power in mode a_2 ($P_2(0) = P_0$).

condition of Equation 2.15. The periodicity of the resulting devices are typically hundreds of micrometers and such gratings are termed long-period gratings. It is important to note at this stage that long-period gratings couple light between two guided modes[21].
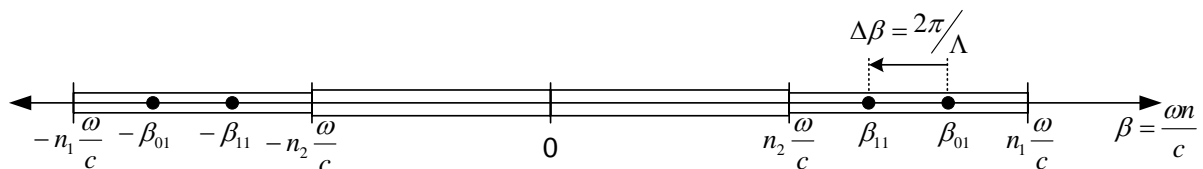
Figure 2.5: Mode coupling between two forward-propagating guided modes. The small value of $\Delta\beta$ results in a large value of the grating periodicity Λ.

A typical variation of the differential propagation constant ($\Delta\beta$) between two forward-propagating guided modes is shown in Figure 2.6. It can be seen that the value of $\Delta\beta$ can be equal at two different operating wavelengths and hence the same grating period might result in modal coupling at two values of wavelength as $\Delta\beta = 2\pi/\Lambda$. The spectral dependence of the coupling coefficient might cause a difference in the coupling magnitude at the two wavelengths. As indicated in Figure 2.6, the wavelength λ_0, at which the slope of the $\Delta\beta$ versus λ curve is zero, is termed the equalisation wavelength between the two modes and the polarity of the slope of the λ versus Λ curve will depend on the relative location of the operating wavelength with respect to λ_0.
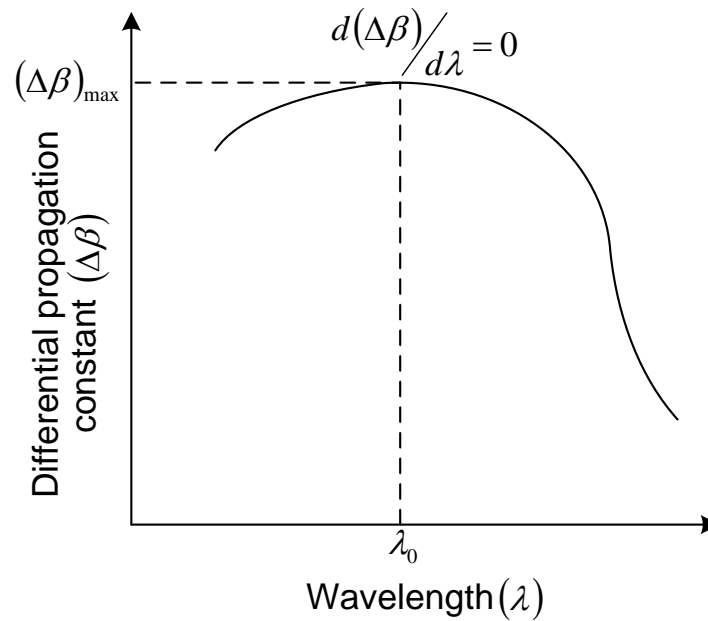
Figure 2.6: Typical variation of the differential propagation constant $(\Delta\beta)$ between two forward-propagating guided modes as a function of the operating wavelength. $\Delta\beta$ attains its maximum value $(\Delta\beta)_{max}$.

2.4 Principle of Operation

Long-period gratings, as discussed in Section 2.3, couple light from the fundamental LP_{01} mode to other forward-propagating cladding modes. The coupling occurs at wavelengths where the phase matching condition $(\Delta\beta = 2\pi/\Lambda)$ is satisfied, and the power is coupled from one mode to another. The forward-propagating $LP_{0,m}$ cladding modes of order m possess propagation constants that are denoted by $\beta^{(m)}$. The basic operating principle of long-period gratings can be explained using the β-plot introduced in Section 2.3. Figure 2.7 shows the simplified mode coupling mechanism in long period gratings[22]. The forward-propagating cladding modes actually fall within the range $\omega n_3/c < \beta^{(m)} < \omega n_2/c$ $(n_2 > n_3)$ (as is shown in Figure 2.2) but in order to keep the representation simple, the ambient external index of refraction n_3 is not depicted in the β-plot.
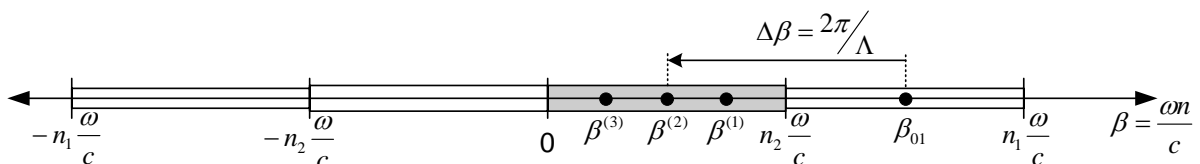
Figure 2.7: Mode coupling mechanism in a long-period grating[22]. β_{01} is the propagation constant of the fundamental guided mode. The shaded region represents a continuum of forward propagating radiation modes.

One can re-write the phase matching condition generically, in terms of the forward prop-

agating cladding modes, as:

$$\Delta\beta^{(m)} = \beta_{01} - \beta^{(m)} = \frac{2\pi}{\Lambda} \tag{2.25}$$

Where: $\Delta\beta^{(m)}$ is the differential propagation constant.

Figure 2.8 shows a transmission spectrum of a typical long-period grating and one can see the coupling of the fundamental guided mode to discrete cladding modes results in distinct resonance bands in the transmission spectrum. Also visible is the different peak values of attenuation and bandwidth due to dissimilar coupling coefficients and this concept will be explored further in due course.
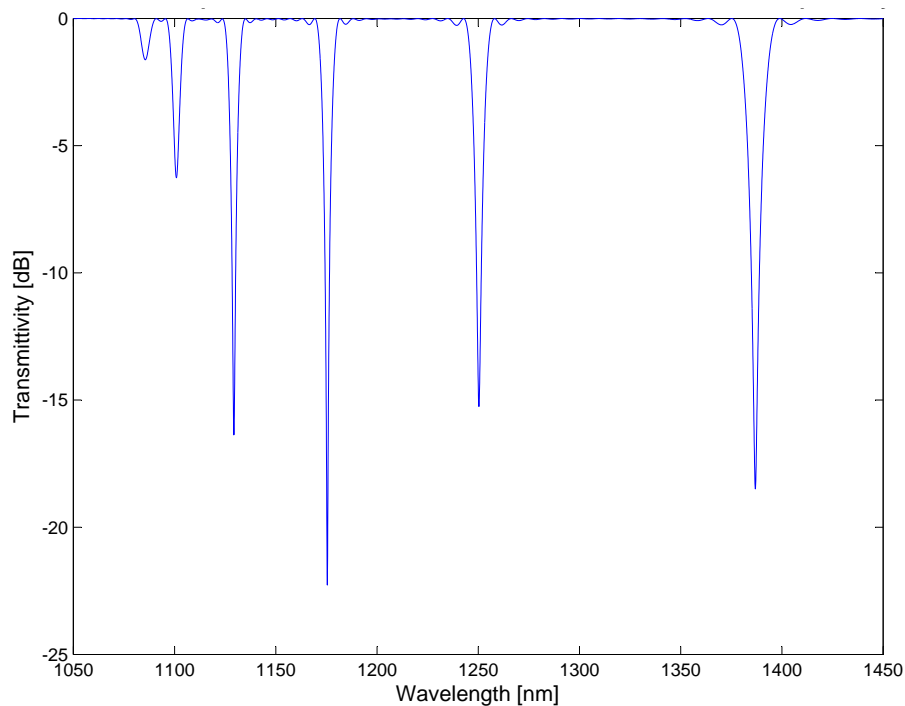
Figure 2.8: The transmission spectrum of a long-period grating with period 320 μm. The discrete, spiky loss bands correspond to the coupling of the fundamental guided mode to discrete cladding modes.

Recall that $\beta = \frac{2\pi n}{\lambda}$ and by defining the effective indices of the cladding and guided modes one can write:

$$\beta_{01} = \frac{2\pi n_{eff}}{\lambda^{(m)}} \text{ and} \tag{2.26}$$

$$\beta^{(m)} = \frac{2\pi n_{cl}^{(m)}}{\lambda^{(m)}} \tag{2.27}$$

Where: n_{eff} is the effective refractive index of the guided mode
$n_{cl}^{(m)}$ is the effective refractive index of the mth order cladding mode
$\lambda^{(m)}$ is the coupling wavelength of the mth order cladding mode.

One can also define the differential effective index, $\delta n_{eff}^{(m)}$, as:

$$\delta n_{eff}^{(m)} = n_{eff} - n_{cl}^{(m)} \tag{2.28}$$

The phase matching condition can be expressed in terms of the differential effective index, and hence in terms of the effective indices of the guided and cladding modes, through Equations 2.25, 2.26 and 2.27 as:

$$\lambda^{(m)} = \left(\delta n_{eff}^{(m)}\right)\Lambda \tag{2.29}$$

For standard optical fibres the differential effective index between the guided and cladding modes $(\delta n_{eff}^{(m)})$ is typically between 10^{-3} and 10^{-2}. This means for coupling to occur at wavelengths between 1200 and 1600 nm, the periods of these gratings must be hundreds of micrometers.

The relative location of the attenuation bands in a grating can be estimated and understood through the β-plot in Figure 2.9[22]. Consider a grating with periodicity Λ such that at a given wavelength, fixed ω, the coupling occurs to the cladding mode denoted by LP$^{(2)}$, or $\beta_{01} - \beta^{(2)} = 2\pi/\Lambda$, as shown in Figure 2.9 (a). For coupling to take place to the fundamental cladding mode, LP$^{(1)}$, for the same grating periodicity, the ω-axis needs to be stretched or expanded which results in the phase-matching vector extending from β_{01} to $\beta^{(1)}$ (Figure 2.9 (b)). The increase in ω corresponds to a decrease in wavelength and thus we expect the LP$^{(1)}$ coupling to occur at a wavelength lower than that for coupling to the LP$^{(2)}$ cladding mode. Due to the periodicity of the grating remaining unchanged, the length of the phase-matching vector remains unchanged for coupling to various cladding modes. Similarly, for power coupling from the guided mode to LP$^{(3)}$ cladding mode, the ω-axis needs to be compressed or contracted (Figure 2.9 (c)), and this results in the coupling wavelength for this mode to occur at wavelengths longer than that for the LP$^{(2)}$ mode.

Figure 2.9 demonstrates that, for a given grating, the phase-matching wavelength increases with the order of the resonance band, however, this analysis assumes that the differential propagation constant $\Delta\beta^{(m)}$ is a deceasing function of the wavelength for all m. This assumption will be shown to be incorrect under some circumstances in due course.

Figure 2.2 shows the cladding modes have propagation constants that lie in the range $\omega n_3/c < \beta^{(m)} < \omega n_2/c; (n_2 > n_3)$. If one utilises these two extreme values of $\beta^{(m)}$, one can calculate the range of coupling wavelength $\lambda^{(m)}$ for the cladding modes. The upper limit of the coupling wavelength that is found using $n_{cl}^{(m)} = 1$ lies far off the spectrum of optical sources and detectors and is hence not significant. The maximum value of the cladding mode propagation constant $\beta^{(m)} = \frac{\omega n_2}{c}$ yields a wavelength parameter termed λ_{cut}[22]. Figure 2.10 depicts the relative location of λ_{cut} with respect to the coupling wavelength $\lambda^{(2)}$ for the second order cladding mode and as expected λ_{cut} is less than the coupling wavelength for all the cladding modes.

Another use of the β-plot is in determining the shift in the spectral location of the resonance bands in long-periods with variation in the core and cladding propagation constants. Figure 2.11 (a) illustrates the coupling of the fundamental guided mode to a

$$\Delta\beta^{(2)} = \beta_{01} - \beta^{(2)} = \frac{2\pi}{\Lambda}$$

(a)

$$\Delta\beta^{(1)} = \beta_{01} - \beta^{(1)} = \frac{2\pi}{\Lambda}$$

(b)

$$\Delta\beta^{(3)} = \beta_{01} - \beta^{(3)} = \frac{2\pi}{\Lambda}$$

(c)
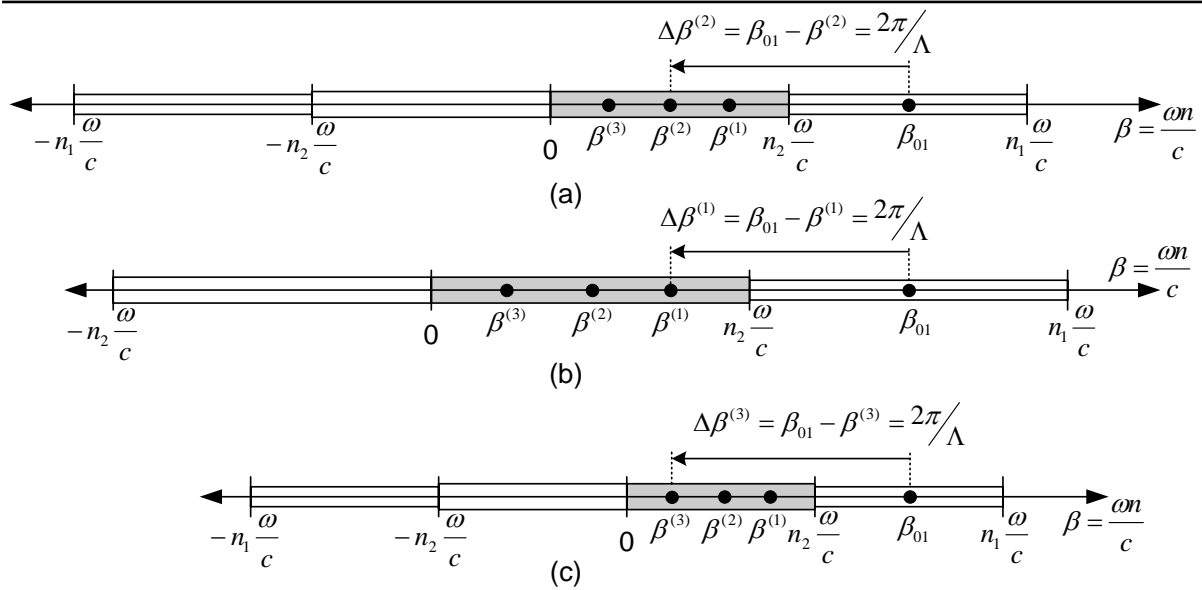
Figure 2.9: The coupling of LP_{01} guided mode to discrete, forward-propagating cladding modes. (a) The coupling to the $LP^{(2)}$ cladding mode. (b) A stretched ω-axis for coupling to the $LP^{(1)}$ cladding mode. (c) A compressed ω-axis for coupling to the $LP^{(3)}$ cladding mode.

$$\Delta\beta^{(2)} = \frac{2\pi}{\Lambda}$$
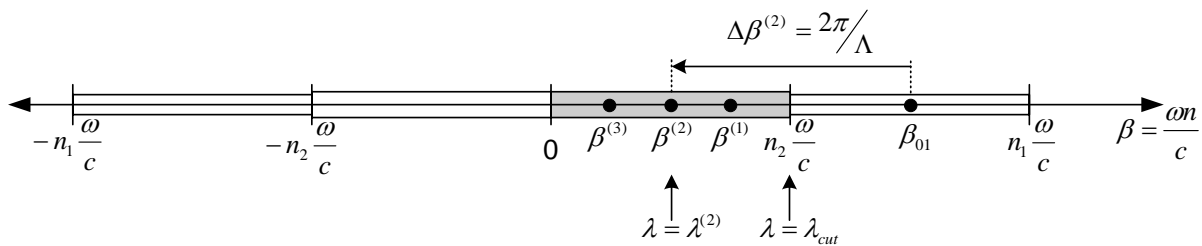
Figure 2.10: Depiction of the spectral location of λ_{cut} relative to wavelength $\lambda^{(2)}$ in a long-period grating ($\lambda_{cut} < \lambda^{(2)}$).

cladding mode of order m, with propagation constant $\beta^{(m)}$. If the value of the periodicity (Λ) remains constant, and the value of β_{01} is increased (Figure 2.11 (b)), the ω-axis has to be compressed to maintain the coupling between the LP_{01} guided mode and the $LP^{(m)}$ cladding modes. The compression of the ω-axis implies that an increase in the resonant wavelengths occur when the value of β_{01} increases. Increasing the value of the cladding mode propagation constant $\beta^{(m)}$ (Figure 2.11 (c)), requires the stretching of the ω-axis and results in lowering of the resonant wavelengths. This means that the increase in the guided and cladding mode propagation constants result in shifts of opposite polarities in the phase-matching wavelengths.

The effect of the change in the periodicity Λ on the refractive index modulation is also simple to predict using the β-plot. It can be shown that when the period is increased, the ω-axis has to be compressed to maintain coupling to the same cladding mode. Thus the coupling wavelength for a particular cladding mode is an increasing function of the

$$\Delta\beta^{(m)} = \frac{2\pi}{\Lambda}$$

$$\beta = \frac{\omega n}{c}$$

$$-n_1\frac{\omega}{c} \qquad -n_2\frac{\omega}{c} \qquad 0 \qquad \beta^{(m)} \quad n_2\frac{\omega}{c} \qquad \beta_{01} \qquad n_1\frac{\omega}{c}$$

(a)

$$\Delta\beta^{(m)} = \frac{2\pi}{\Lambda}$$

$$\beta = \frac{\omega n}{c}$$

$$-n_1\frac{\omega}{c} \qquad -n_2\frac{\omega}{c} \qquad 0 \qquad \beta^{(m)} \quad n_2\frac{\omega}{c} \qquad \beta_{01} \quad n_1\frac{\omega}{c}$$

(b)

$$\Delta\beta^{(m)} = \frac{2\pi}{\Lambda}$$

$$\beta = \frac{\omega n}{c}$$

$$-n_1\frac{\omega}{c} \qquad -n_2\frac{\omega}{c} \qquad 0 \qquad \beta^{(m)} \quad n_2\frac{\omega}{c} \qquad \beta_{01} \qquad n_1\frac{\omega}{c}$$

(c)
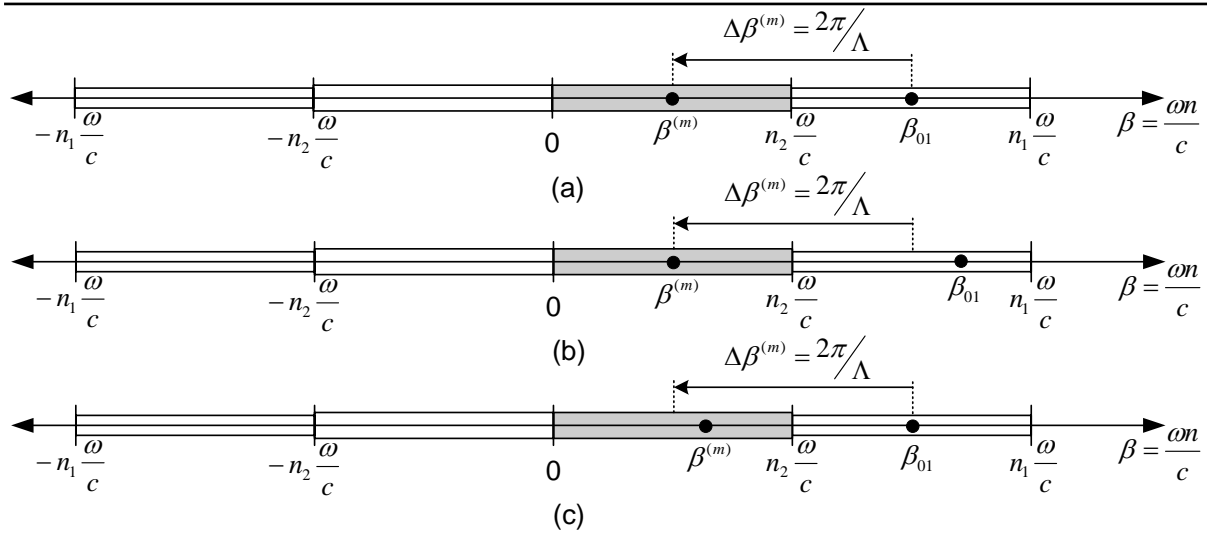
Figure 2.11: The effect of changes in propagation constants of the core and cladding modes. (a) Coupling of the fundamental guided mode (Propagation constant β_{01}) to a cladding mode (propagation constant $\beta^{(m)}$), (b) an increase in β_{01} and (c) an increase in $\beta^{(m)}$ [21].

grating period.

In this section the principle of operation of long-period gratings that couple the fundamental guided mode to circularly-symmetric cladding modes was discussed. These gratings were shown to have a different spectral response as compared to their short-period counterparts. Using β-plots we determined the direction of spectral shift when the grating period or the propagation constants are varied. It was assumed that the fibre is operating in the single-mode regime and hence only the fundamental guided mode was included in the analysis.

Chapter 3

Analytical Modelling and Simulations

This Chapter begins by developing a comprehensive theoretical model of long-period gratings and later, through it use, demonstrates simulation results. The basic concept of group index is utilised to explain the polarity of the slope of the coupling wavelength versus grating period curve. It is also shown that the refractive index of a material is a function of the operating wavelength and Sellmeier coefficients are employed to calculate the spectral variation of the index of refraction for different germania doping concentrations in a fibre.

3.1   Fundamental Concepts

We start by rewriting the phase-matching condition of Equation 2.29 as:

$$\Lambda = \frac{\lambda}{\delta n_{eff}} \tag{3.1}$$

Where: δn_{eff} is the differential effective index at wavelength λ ($\delta n_{eff} = n_{eff} - n_{cl}$).

To simplify the notation, the ordinal m, used to represent the order of the cladding mode, has been dropped. Since δn_{eff} is itself a function of the operating wavelength, differentiating both sides of Equation 3.1 with respect to wavelength yields:

$$\frac{d\Lambda}{d\lambda} = \frac{\delta n_{eff} - \lambda \left(\frac{d(\delta n_{eff})}{d\lambda} \right)}{(\delta n_{eff})^2} \tag{3.2}$$

We now define the group index of the guided (n_g) and cladding ($n_{g,cl}$) modes as[23]:

$$n_g = n_{eff} - \lambda \frac{dn_{eff}}{d\lambda} \tag{3.3}$$

$$n_{g,cl} = n_{cl} - \lambda \frac{dn_{cl}}{d\lambda} \tag{3.4}$$

By substituting Equations 3.3 and 3.4 into Equation 3.2, one obtains an expression for the slope of the coupling wavelength versus the grating period curve[24]:

$$\frac{d\lambda}{d\Lambda} = \frac{(\delta n_{eff})^2}{\delta n_g} \tag{3.5}$$

Where: δn_g is the differential group index ($\delta n_g = n_g - n_{g,cl}$).

Equation 3.5 reveals that the slope of the coupling wavelength versus period curve is not only dependent on the differential effective index, δn_{eff}, but also on the differential group index, δn_g, between the guided and cladding modes. The wavelength versus period curve is known as the characteristic curve of the grating.

Since δn_{eff} and δn_g are strong functions of the parameters of the optical fibre in which the grating is fabricated, the characteristic curves can be expected to be dependent on the properties of the host fibre. For most grating applications, the period is chosen so that the group index of the guided mode is larger than that of the cladding mode at the phase-matching wavelength ($\delta n_g > 0$), thus the local slope of the characteristic equation is typically positive.

The differential group index, δn_g, is a strong function of wavelength and since $\delta n_g(\lambda)$ is continuous with wavelength we deduce that there might exist a wavelength λ_0 in the optical spectrum where $\delta n_g(\lambda_0) = 0$. The wavelength at which the group indices of the guided and cladding modes are identical ($n_g = n_{g,cl} = n_0$) is termed the equalisation wavelength of the modes[23]. At this value of wavelength, the two modes travel with the same group velocity given by:

$$v_g = \frac{c}{n_0} \tag{3.6}$$

We can also represent the equalisation wavelength λ_0 in terms of the differential propagation constant $\Delta\beta$, as was shown in Section 2.3.2, where we showed that at the wavelength λ_0, the slope of the curve $\Delta\beta$ versus λ is zero.

The differential propagation constant is related to the grating period through the phase-matching condition and so it can be shown that:

$$\frac{d(\Delta\beta)}{d\lambda} = -\frac{2\pi}{\Lambda^2}\frac{d\Lambda}{d\lambda} \tag{3.7}$$

Hence at the equalisation wavelength, the slope of the characteristic curve is expected to be infinite, which follows from Equation 3.5 with $\delta n_g = 0$. One can thus conclude that the characteristic curves of long-period gratings may possess slopes of both polarities depending on the location of the coupling wavelength with respect to the equalisation wavelength of the two modes involved in coupling.

For a long period grating the magnitude and polarity of the slope of the characteristic curve is a function of the phase-matching wavelength and hence depends on the grating periodicity. This is an important difference between long and short-period gratings because it can be shown that the slope of the characteristic curve of a short-period grating

is positive and constant for all values of the coupling wavelength.

In the next section we will carry out a detailed waveguide analysis to determine the spectral dependence of the effective indices of the guided and cladding modes. Since these parameters are functions of the core and cladding refractive indices, it becomes important to include the material variation of the fibre indices in the analysis. A simple technique to predict the change in the core and cladding refractive indices with respect to wavelength if the germania concentration in the core is known is developed.

Material dispersion in optical fibres is caused by the variation in the refractive index of the host glass over the spectrum of the optical source[23]. The most common method of approximating the index $n(\lambda)$ as a function of wavelength λ for a particular material uses the Sellmeier equation[21]:

$$n^2(\lambda) = 1 + \sum_{i=1}^{M} \frac{A_i \lambda^2}{\lambda^2 - \lambda_i^2}$$ (3.8)

Where: A_i and λ_i are material dependent parameters.

Both A_i and λ_i are tabulated in technical literature, however, for most practical applications, only the first three terms ($M = 3$) are necessary to obtain an accuracy of about 10^{-5} in refractive index calculations[23]. Table 3.1 lists the first three Sellmeier parameters for quenched silica and 86,5% Silica 13,5% germanium oxide (GeO_2).

Table 3.1: Sellmeier parameters for bulk glass samples of different compositions[25].

Composition	A_1	A_2	A_3	λ_1 (μm)	λ_2 (μm)	λ_3 (μm)
Quenched SiO_2	0.696750	0.408218	0.890815	0.069066	0.115662	9.900559
13,5% GeO_2:86,5% SiO_2	0.711040	0.451885	0.704048	0.064270	0.129408	9.425478

The cladding in a majority of standard optical fibres is made of quenched silica whereas the core typically consists of quenched silica with an appropriate doping of GeO_2. The discussion will be limited to fibres with germanosilicate cores and silica cladding, although it is simple to modify the analysis for other materials.

The values of the Sellmeier parameters have been measured for only a few specific GeO_2 concentrations and hence the index variation for intermediate doping concentrations can be calculated by interpolation of the given parameters[23]. For example the Sellmeier parameters for a sample of 6,75% GeO_2 and 93,25% SiO_2 can be approximated by averaging the vlaues in Table 3.1. After obtaining the variation of refractive index from Equation 3.8, the group index, $n_g(\lambda)$, of the material can be obtained by:

$$n_g(\lambda) = n(\lambda) - \lambda \frac{dn(\lambda)}{d\lambda}$$ (3.9)

Figure 3.1 depicts the variation in the refractive index $n(\lambda)$ and group index of three different types of materials.
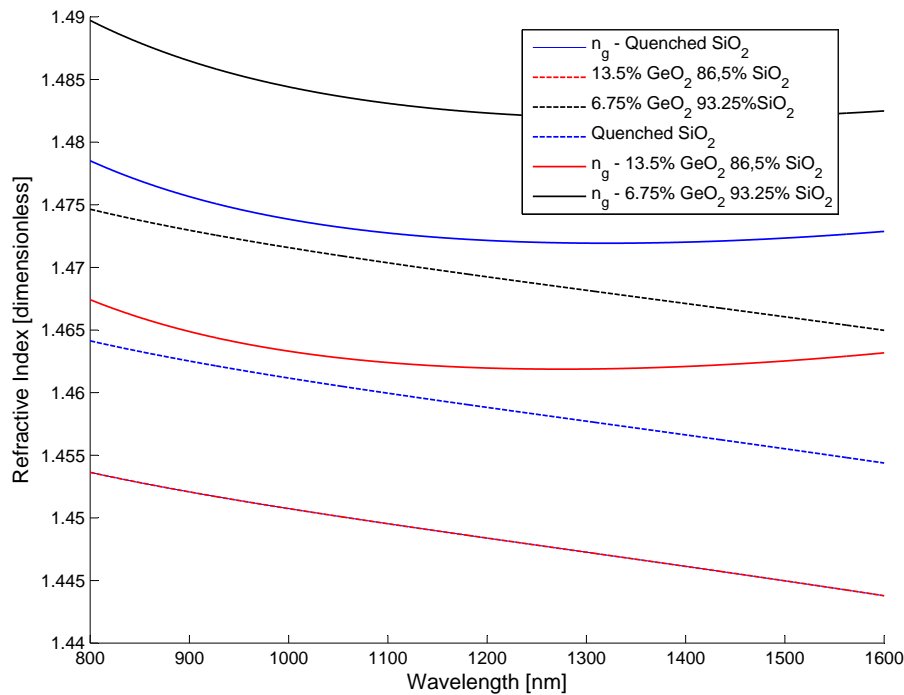
Figure 3.1: Variation of refractive index of three different materials as functions of wavelength. Also shown is the variation of the group indices of the three materials.

The group indices are found to initially decrease with wavelength, attain a minimum value and then increase toward higher wavelengths. The wavelength at which the slope of the group index versus the wavelength curve is zero $(dn_g(\lambda)/d\lambda = 0)$, is termed the zero material dispersion wavelength for the material[21, 23]. In an actual fibre, the presence of the cladding causes the waveguide effect to alter the wavelength at which the total dispersion is zero[21, 23].

3.2 Waveguide Analysis

In this section we develop techniques to determine the effective indices of the fundamental guided mode and the circularly-symmetric cladding modes for different fibres.

Although long-period gratings are fabricated in many different optical fibres, we will limit our discussion to only three types of fibres. The three fibres that will be used in the analysis have step-index, matched clad profiles with pure silica cladding and germania-doped core. The parameters of the three fibres, termed SMF-28[26], Flexcor 1060 nm [27] and Flexcor 780 nm [27] are listed in Table 3.2. The values tabulated are the typical values listed in the data sheets for the respective fibres.

During the analysis of cladding modes, the refractive index of the ambient medium will be shown to have a significant impact on their effective indices. Typically the bare cladding in the region containing the grating is surrounded by air and although the refractive index

Table 3.2: Typical parameters for the fibres used in the analysis of the long-period gratings[27, 26]

Type of fibre	Optimum Wavelength λ_{op} [nm]	Core Radius a [μm]	Core delta Δ [%]	Numerical Aperture	Cutoff Wavelength λ_{cutoff} [nm]
SMF-28	1310	4,15	0,36	0,13	<1260
Flexcor 1060	1060	2,5	0,45	0,14	920 ($\pm$50)
Flexcor 780	780	2,0	0,45	0,14	720 ($\pm$50)

Type of fibre	Mode Field diameter at λ_{op} [μm]	Attenuation at λ_{op} α [dB/km]	Cladding diameter $2b$ [μm]	Coating diameter $2c$ [μm]	Tensile proof stress F [psi]
SMF-28	9,3 ($\pm 0,5$)	$\leq 0,4$	125 ($\pm$1)	245 ($\pm$10)	100000
Flexcor 1060	6,2 ($\pm 0,5$)	$\leq 1,5$	125 ($\pm$2)	250 ($\pm$15)	100000
Flexcor 780	4,6 ($\pm 0,5$)	$\leq 3,0$	125 ($\pm$2)	250 ($\pm$15)	100000

of air is also a function of the operating wavelength, its variation in the region 700 to 1700 nm can be considered to have a negligible influence on the grating properties[23]. It is for this reason, that during the analysis of long-period gratings, the spectral variation of its refractive index will be ignored.

3.2.1   Fundamental Guided Mode Analysis

Within this Section we obtain the variations of the effective index n_{eff} and group index n_g of the fundamental LP_{01} guided mode as functions of wavelength. Since all three fibres have step-index refractive index profiles, we will consider the fibre geometry shown in Figure 3.2. The amplitude of the guided mode decays rapidly as a function of increasing penetration into the cladding and causes it to possess negligible value at the outer cladding boundary. Thus for fibres that have a significantly thick claddings, the analysis becomes simpler if the cladding is assumed to extend to infinity. In Figure 3.2, a is the core radius, n_1 is the core index and n_2 is the cladding index and as discussed previously both n_1 and n_2 and dependent on the operating frequency. The normalised frequency or V-number of the fibre is given by[21]:

$$V = \frac{2\pi a}{\lambda} \sqrt{n_1^2 - n_2^2} \qquad (3.10)$$

The normalised index difference Δn between the core and cladding is defined as[21]:

$$\Delta n = \frac{n_1 - n_2}{n_1} \qquad (3.11)$$

The normalised index difference depends on the germania concentration in the core[21]. Since the cladding in the three fibres under discussion are made from quenched silica, we can calculate the material dispersion for both the core and cladding if the normalised
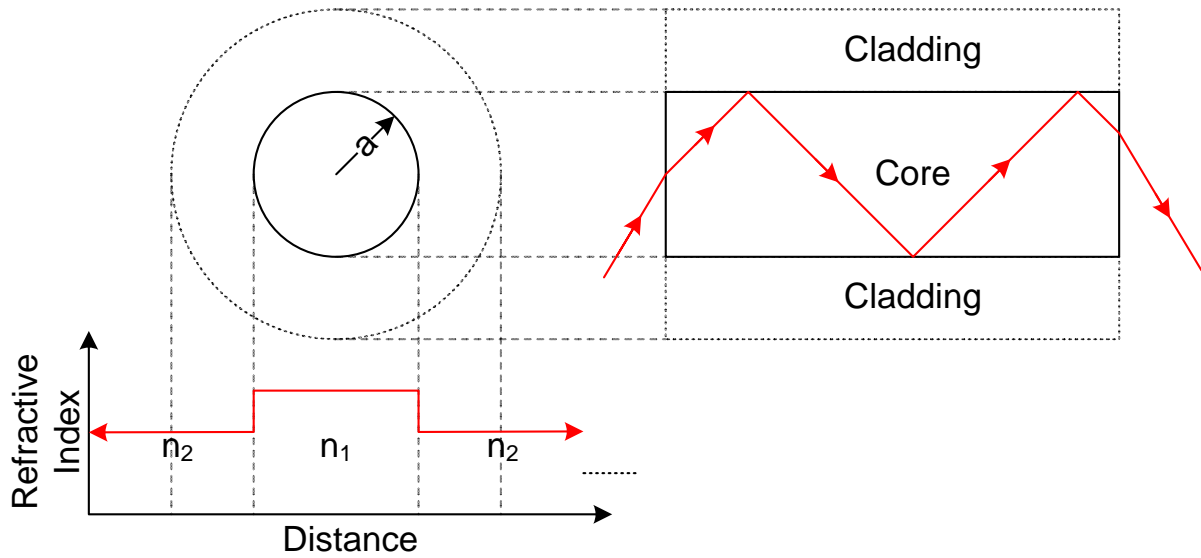
Figure 3.2: Fibre geometry used in the analysis of the fundamental guided mode. The core has a radius a, whereas the cladding is assumed to extend to infinity

index difference, Δ, is known. In order to obtain Δ, the Sellmeier parameters are interpolated.

One will recall that:

$$\beta_{01} = \frac{2\pi n_{eff}}{\lambda}$$

$$\text{and } k = \frac{2\pi n}{\lambda} \tag{3.12}$$

Now one may define k for both core and cladding by:

$$k_1 = \frac{2\pi n_1}{\lambda} \tag{3.13}$$

$$\text{and } k_2 = \frac{2\pi n_2}{\lambda} \tag{3.14}$$

$$\tag{3.15}$$

β_{01}, k_1 and k_2 jointly define the waveguide parameters u and w by[28]:

$$u = \sqrt{k_1^2 - \beta_{01}^2} \tag{3.16}$$

$$\text{and } w = \sqrt{\beta_{01}^2 - k_2^2} \tag{3.17}$$

The characteristic equation for an LP_{0m} guided mode propagating in a fibre with the profile shown in Figure 3.2 is given by[21]:

$$\frac{1}{u}\frac{J_1(ua)}{J_0(ua)} = \frac{1}{w}\frac{K_1(wa)}{K_0(wa)} \tag{3.18}$$

Where: m is the radial order of the mode

J_p is the Bessel function of order p

K_p is the modified Bessel function of order p.

The complete process of calculating the effective index as a function of the operating wavelength can be outlined as follows:

1. Given the normalised index difference Δ of the fibre, the germania concentration in the core can be approximated.

2. Using linear interpolation of the Sellmeier parameters in Table 3.1, the spectral variation of n_1 and n_2 can be obtained at discrete wavelengths.

3. The characteristic equation is then solved at these discrete wavelengths to determine the effective index.

Germania Concentration

By rearranging Equation 3.11 one obtains an expression for the refractive index of the core, given n_2 and Δ as:

$$n_1 = \frac{n_2}{1 - \Delta} \tag{3.19}$$

The spectral variations of various concentrations of Germania in Silica are known from Figure 3.1. This means the concentrations of Germania required to obtain specific values of Δ can be plotted against wavelength. This process has been performed for the two values of Δ from Table 3.2 and the plots are shown is Figures 3.3 and 3.4.
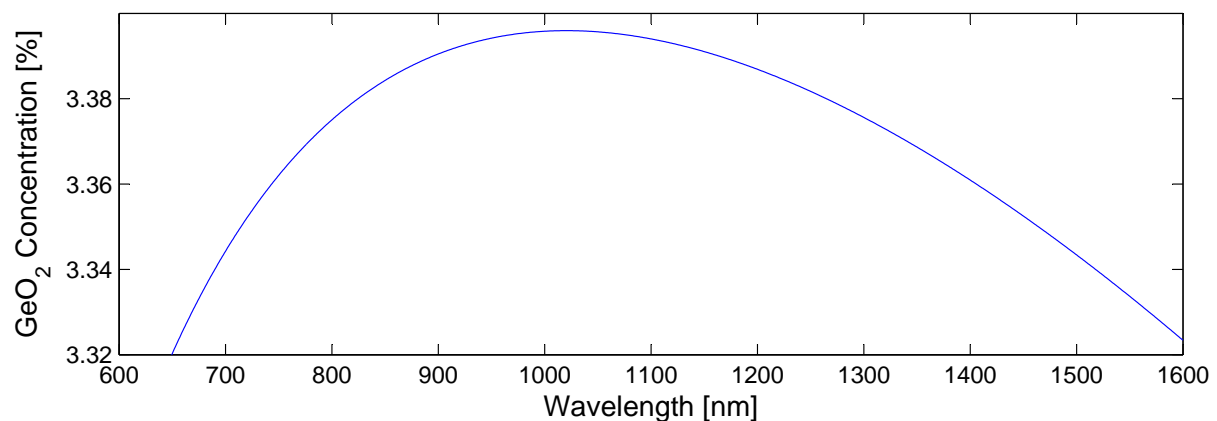
Figure 3.3: The spectral variation of the concentration of Germania required to maintain a specific index difference $\Delta = 0,36\%$ plotted against wavelength

From Figures 3.3 and 3.4, the Germania concentration for the SMF-28, optimised for 1310 nm from Table 3.2, is calculated to be 3,374% Germania. Similarly for Flexcor 1060, optimised for 1060 nm, is calculated to be 4,248% Germania and lastly Flexcore 780, optimised for 780 nm, is calculated to be 4,217%.
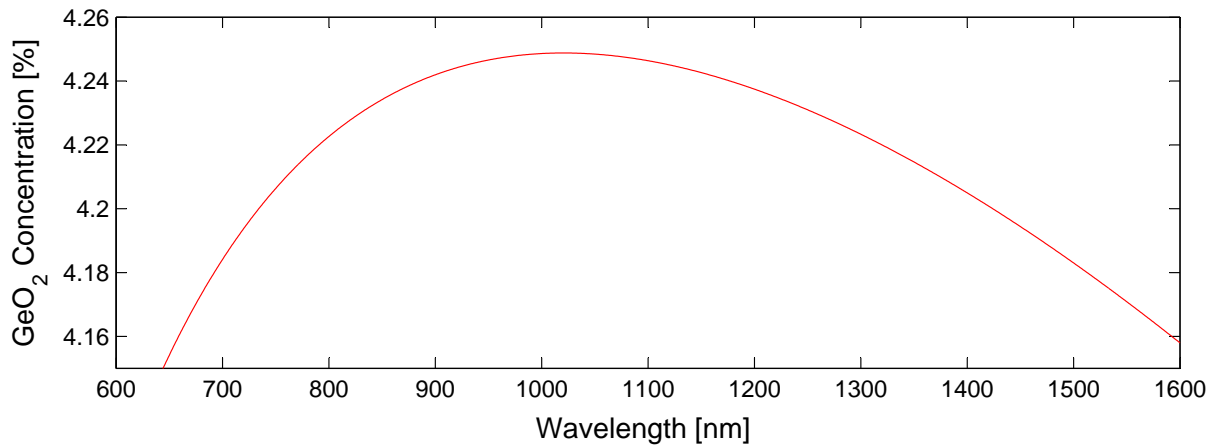
Figure 3.4: The spectral variation of the concentration of Germania required to maintain a specific index difference $\Delta = 0,45\%$ plotted against wavelength

Interpolation of Sellmeier Parameters

The values in Table 3.1 are linearly interpolated between 0 and 13,5% Germania and co-efficients for concentrations obtained above are calculated. These are then substituted into Equation 3.8 to calculate the specific spectral variations of the refractive indices of the cores of the three fibres under investigation.

The graph in Figure 3.5 shows the spectral relationship between the quenched silica cladding refractive index and the refractive indices of the germania doped core's of the 3 fibres between 600 and 1600 nm. One can see how the two Flexcor fibres have very similar refractive index profiles given they have the same normalised index difference Δ but are optimised for different wavelengths.

Solving the Characteristic Equation

At this stage one knows the spectral relationships of the core and cladding refractive indices of all three fibres and can proceed with a solution of the characteristic equation in Matlab. The characteristic equation was solved numerically for its first root ($m = 1$) using the Newton-Raphson method. The solution was sought till the effective index n_{eff} converged to 6 decimal places to reduce errors in further simulations. In order to solve the characteristic equation utilising the Newton-Raphson method initial starting values need to be supplied. The estimated value for n_{eff} is the average value of n_1 and n_2 based on the fact that the effective refractive index will always lie between n_1 and n_2.

Figure 3.6 shows the spectral variation in the effective index n_{eff} for the SMF-28 fibre following the solution of the characteristic equation at discrete wavelengths. Also shown are the core and cladding material indices as functions of wavelength.

The results of Figure 3.6 are for an unperturbed fibre, or one with no refractive index modulation of the core. The values utilised above are also typical values specified by
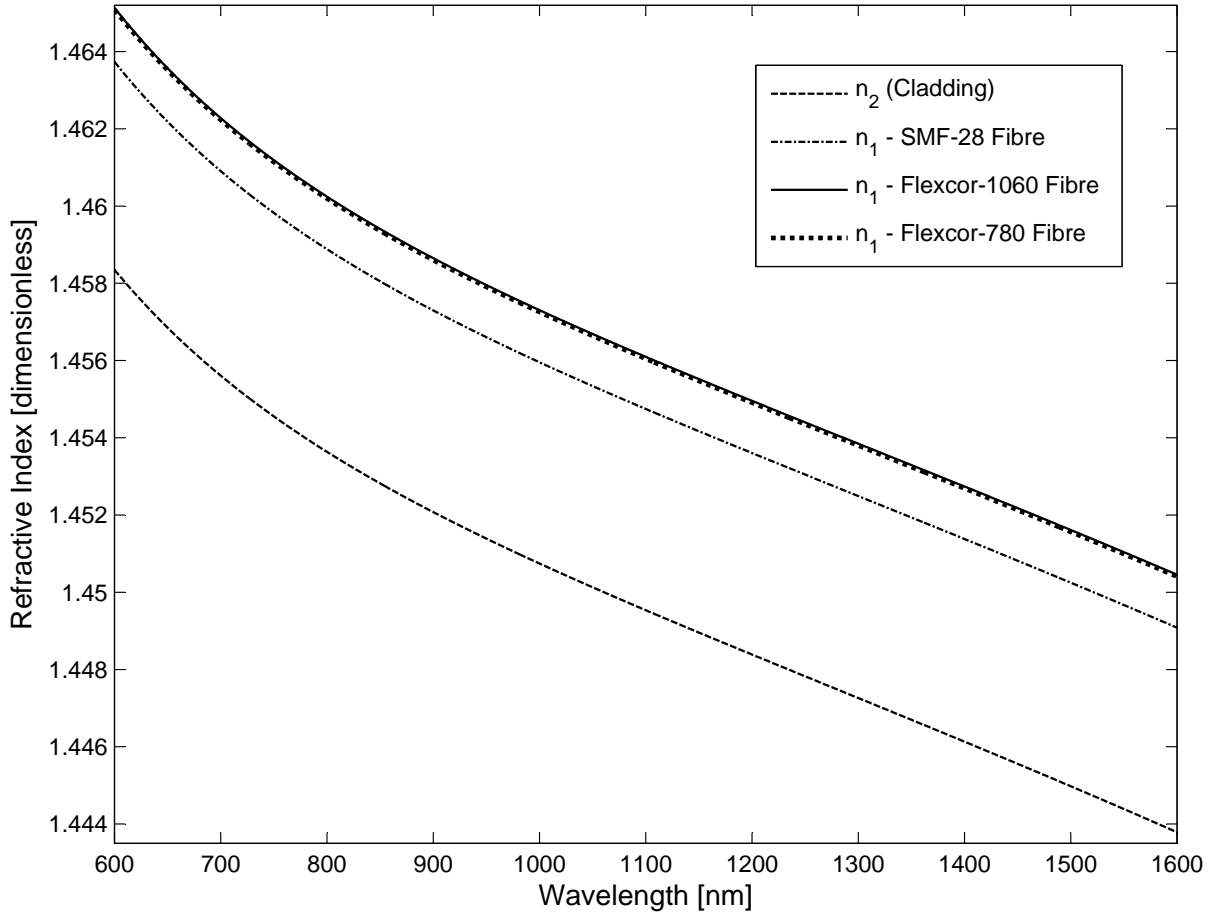
Figure 3.5: Spectral relationships between the refractive indices of 3 germania doped cores and the quenched silica cladding

manufacturers and n_{eff} is found to be an increasing function of the core diameter and index difference[23]. A core radius change of 1% equates to an approximate change of 3×10^{-5} in n_{eff}, whereas a 1% change in normalised index difference equates to an approximate change of 4×10^{-5}[23].

The electric field of the fundamental guided mode $E_{01}(r)$ is given by the expression[21]:

$$E_{01}(r) = AJ_0(ur)e^{j(\omega t - \beta_{01} z)} \text{ for } r < a \qquad (3.20)$$
$$E_{01}(r) = BK_0(wr)e^{j(\omega t - \beta_{01} z)} \text{ for } r < a \qquad (3.21)$$

Where: u is defined in Equation 3.16.
w is defined in Equation 3.17.
J_0 is the Bessel function of the zeroth order.
K_0 is the modified Bessel function of the zeroth order.

The mode confinement within the core decreases as the wavelength is increased and the modal amplitude is almost negligible at the outer cladding boundary[23]. The fact of the almost negligible modal amplitude at the outer cladding boundary lends credibility to
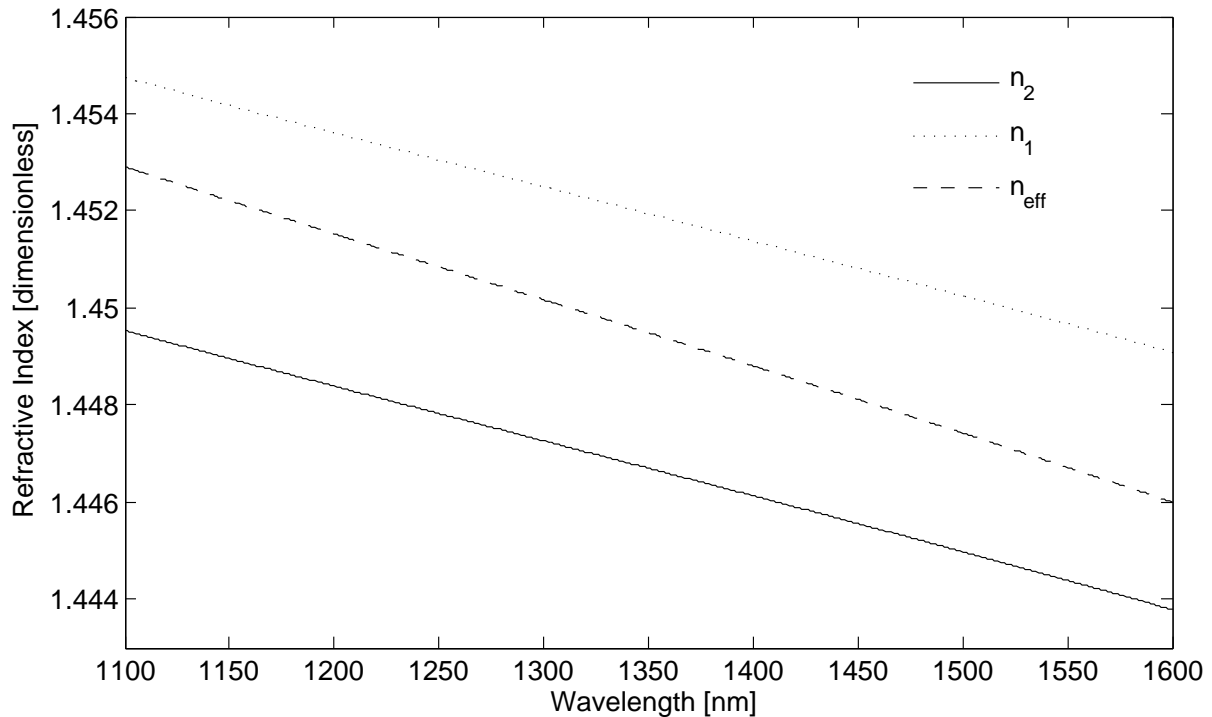
Figure 3.6: Variation of the effective refractive index n_{eff} of the fundamental LP_{01} guided mode versus wavelength for Corning SMF-28 fibre. Also shown are the core (n_1) and cladding (n_2) refractive indices.

the approximation of an infinite cladding during the guided mode analysis.

In this section we have discussed the analysis of the fundamental guided mode in optical fibres assuming the cladding extends to infinity. The variation of the effective and group indices with respect to wavelength was obtained for various types of fibres and it was observed that deviations of about 1% in the typical core radius and normalised indices result in an average change of the order of $3,5 \times 10^{-5}$ in the calculated effective index.

3.2.2   Cladding Mode Analysis

This stage in the analytical modelling involves the calculation of the effective indices of the circularly-symmetric, forward propagating cladding modes. This section investigates the spectral variations of the effective indices, group indices and modal fields for cladding modes of different orders.

The evaluation of the cladding modes uses the approximation that the fibre can be considered as a multi-mode step-index structure ignoring the presence of the core[22, 23], in order to simplify the analysis of the cladding modes. For a weakly guiding fibre with closely matched values of the core and cladding indices this assumption yields a fair approximation of the cladding mode propagation constants.

The fibre geometry to be analysed thus reduces from that in Figure 3.2, to the profile shown in Figure 3.7, where the core radius a has been replaced by the cladding radius b, and the cladding index n_2 substitutes the core index n_1. The refractive index of the medium surrounding the fibre cladding, n_3 replaces n_2 in Figure 3.2.
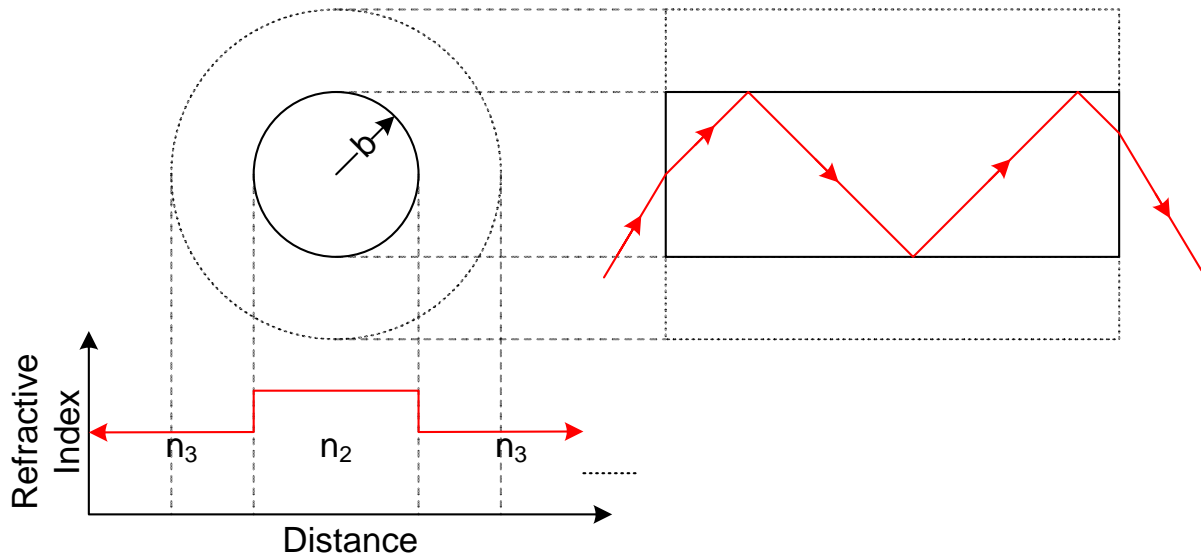
Figure 3.7: Fibre geometry used in the analysis of the cladding modes. The core index is substituted with the cladding refractive index, n_2, and the core radius is replaced by the cladding radius, b. n_3 is the refractive index of the medium surrounding the fibre cladding.

The effective index of the mth order cladding mode is denoted by $n_{cl}^{(m)}$ and the free space propagation constants of the core and surrounding medium are given by:

$$k_2 = \frac{2\pi n_2}{\lambda} \tag{3.22}$$

$$k_3 = \frac{2\pi n_3}{\lambda} \tag{3.23}$$

Also the propagation constant of the LP_{0m} cladding mode with effective index $n_{cl}^{(m)}$ is given by:

$$\beta^{(m)} = \frac{2\pi n_{cl}^{(m)}}{\lambda} \tag{3.24}$$

Equations 3.22, 3.23 and 3.24 can be utilised to define the waveguide parameters $u_{cl}^{(m)}$ and $w_{cl}^{(m)}$ for the cladding which are defined by[21]:

$$u_{cl}^{(m)} = \sqrt{k_2^2 - (\beta^{(m)})^2} \tag{3.25}$$

$$w_{cl}^{(m)} = \sqrt{(\beta^{(m)})^2 - k_3^2} \tag{3.26}$$

Using the assumptions and approximations in Figure 3.7, the eigenvalue equation for the LP_{0m} cladding mode can then be approximated by that of a uniform dielectric cylinder surrounded by an infinite medium[21]:

$$\left(\frac{J_1'\left(u_{cl}^{(m)}b\right)}{u_{cl}^{(m)}J_1\left(u_{cl}^{(m)}b\right)} + \frac{K_1'\left(w_{cl}^{(m)}b\right)}{w_{cl}^{(m)}K_1\left(w_{cl}^{(m)}b\right)} \right) \left(k_1^2 \frac{J_1'\left(u_{cl}^{(m)}b\right)}{u_{cl}^{(m)}J_1\left(u_{cl}^{(m)}b\right)} + k_2^2 \frac{K_1'\left(w_{cl}^{(m)}b\right)}{w_{cl}^{(m)}K_1\left(w_{cl}^{(m)}b\right)} \right)$$
$$= \left(\frac{\beta_{cl}^{(m)}}{b} \right)^2 \left(\frac{1}{\left[\left(u_{cl}^{(m)}\right)^2 + \left(w_{cl}^{(m)}\right)^2 \right]} \right)^2 \quad (3.27)$$

Where: $\quad '\quad$ denotes differentiation with respect to the argument.

$\qquad u_{cl}^{(m)} \quad$ is defined in Equation 3.25.

$\qquad w_{cl}^{(m)} \quad$ is defined in Equation 3.26.

$\qquad J_1 \quad$ is the Bessel function of the first order.

$\qquad K_1 \quad$ is the modified Bessel function of the first order.

$\qquad b \quad$ is the radius of the core as shown in Figure 3.7.

The equation was solved for n_{cl} at a finite number of wavelengths using the Newton-Raphson method and the initial estimation required for the Newton-Raphson method of solution was found using[23]:

$$n_{cl}^{(m)} = \sqrt{n_2^2 - \left(\frac{\lambda}{2\pi} \right)^2 \left(\frac{j_m}{b} \right)^2} \quad (3.28)$$

Where: $\quad j_m \quad$ are the roots of the Bessel function of order zero ($J_0(j_m) = 0$).

The spectral results of the solution to Equation 3.27 using initial estimations from Equation 3.28 are shown in Figure 3.8 for even order modes from $m = 2$ to $m = 16$ (top to bottom) with the ambient refractive index $n_3 = 1$. Figure 3.8 shows that for a fixed wavelength, the effective index is a decreasing function of the order of the cladding mode m.

In this section we analysed the important characteristics of forward-propagating cladding modes of different orders. The spectral variation of the effective index was obtained and it was shown that that the effective index is a decreasing function of the order of the cladding mode m.

3.2.3 Characteristic Curves of Long-Period Gratings

In Section 3.2.1 we determined the spectral dependence of the effective index of the fundamental guided mode and those of the circularly symmetric cladding modes in Section 3.2.2. The next step in the complete characterisation of long-period gratings is the evaluation of the set of periods that would induce coupling between the guided mode and cladding modes of different orders at a particular wavelength.
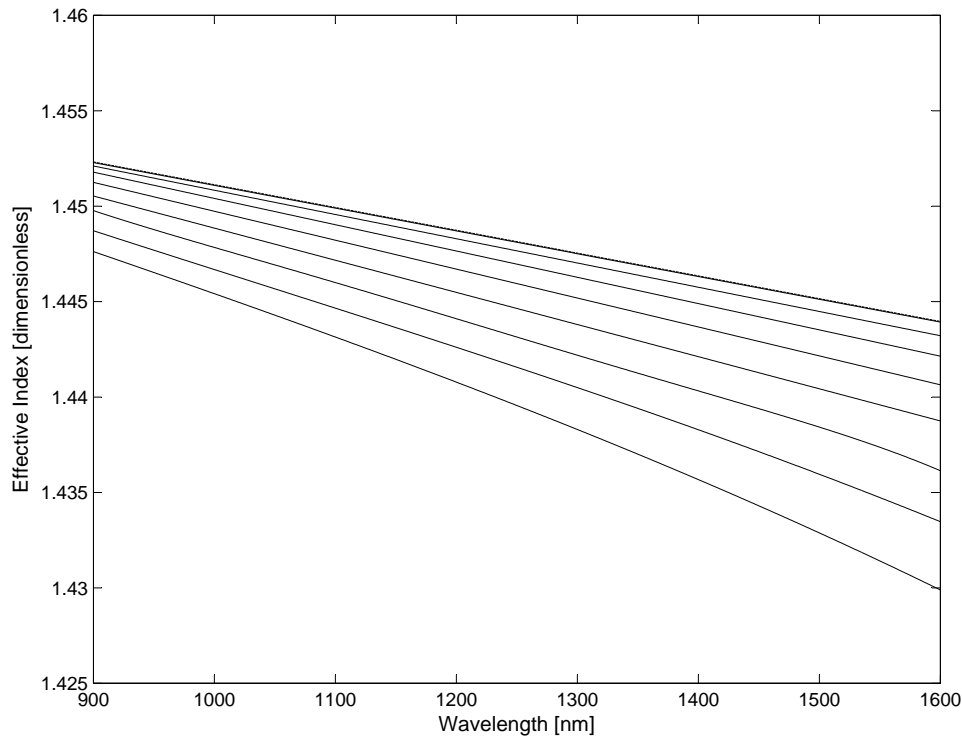
Figure 3.8: Spectral variation of the effective index $n_{cl}^{(m)}$ of $\text{LP}_{0,m}$ cladding modes (m = 2 through 16 in steps of 2) in optical fibres with quenched silica and b = 62,5 μm. The ambient medium is assumed to be air and the dashed (topmost line) line represents the refractive index of the cladding. The bottom line represents the m = 16 cladding mode.

We begin by re-writing the phase-matching condition of Equation 2.29 to determine the grating period Λ required to produce coupling between the guided mode and a cladding mode of order m as:

$$\Lambda = \frac{\lambda^{(m)}}{\left(\delta n_{eff}^{(m)}\right)} \tag{3.29}$$

Where: $\lambda^{(m)}$ is the coupling wavelength
$\delta n_{eff}^{(m)}$ $= n_{eff} - n_{cl}^{(m)}$.

In order to realise the nature of accuracy required in the analysis of long-period gratings, we consider a small error $\Delta\left(\delta n_{eff}^{(m)}\right)$ in the calculation of the differential effective index $\delta n_{eff}^{(m)}$. If the period Λ can be determined accurately, the overall error in the coupling wavelength $\Delta\lambda^{(m)}$ is then given by:

$$\Delta\lambda^{(m)} = \Delta\left(\delta n_{eff}^{(m)}\right)\Lambda \tag{3.30}$$

The expression in Equation 3.30 implies that for a grating with a period $\Lambda = 100\ \mu$m the differential effective index needs to be measured with an accuracy of 1×10^{-5} to achieve an error less than 1 nm in the calculation of the coupling wavelength. Hence it

is expected that small deviations in the fibre parameters that serve to produce changes in the effective indices of the guided and cladding modes may severely alter the values of the coupling wavelengths.

The high sensitivity to slight variations in the differential effective index can be attributed to the coupling mechanism in long-period gratings. Since the coupling occurs between two forward-propagating modes with very close values of effective indices, very small errors in their analysis can result in large discrepancies between the actual and calculated values of coupling wavelengths.

Differential Propagation Constant

In this section we determine the differential propagation constant as a function of wavelength for a cladding mode of order m. Recall the differential propagation constant $\Delta\beta^{(m)}$ is given by:

$$\Delta\beta^{(m)} = \frac{2\pi\delta n_{eff}^{(m)}}{\lambda} \tag{3.31}$$

From Figure 3.6 the spectral variation of n_{eff} is known and from Figure 3.8, the spectral variation of the cladding modes is known. Recall:

$$\delta n_{eff}^{(m)} = n_{eff} - n_{cl}^{(m)} \tag{3.32}$$

Substituting Equation 3.32 into Equation 3.31, one obtains:

$$\Delta\beta^{(m)} = \frac{2\pi(n_{eff} - n_{cl}^{(m)})}{\lambda} \tag{3.33}$$

From Equation 3.33, the spectral variation of the differential propagation constant can be obtained. Figure 3.9 depicts the spectral variation of the differential propagation constant between the fundamental guided mode and the $LP_{0,12}$ cladding mode for an unperturbed SMF-28 fibre. The propagation constant difference initially decreases with wavelength, reaches a minimum and then starts increasing with wavelength.

Recall that the equalisation wavelength λ_0 is defined as the wavelength at which the differential propagation constant does not change with the operating wavelength. Since the equalisation wavelength is a function of the order m of the cladding mode, we will denote it by $\lambda_0^{(m)}$. From Figure 3.9 λ_0^{12} is found to be 1488 nm.

From Equation 3.7 we observe that the slope of the characteristic curve, a plot of coupling wavelength versus grating period, is of opposite polarity to the slope of the curve in Figure 3.9. Hence for wavelengths less than the equalisation wavelength, the characteristic curve for the $LP_{0,12}$ cladding mode is expected to have a positive slope and vice-versa.

The curve in Figure 3.9 also reveals the effects of changing the differential propagation constant between the guided and cladding modes. If the coupling wavelength is less than the equalisation wavelength, $\lambda^{(m)} < \lambda_0^{(m)}$, an increase in the value of $\Delta\beta^{(m)}$ causes the
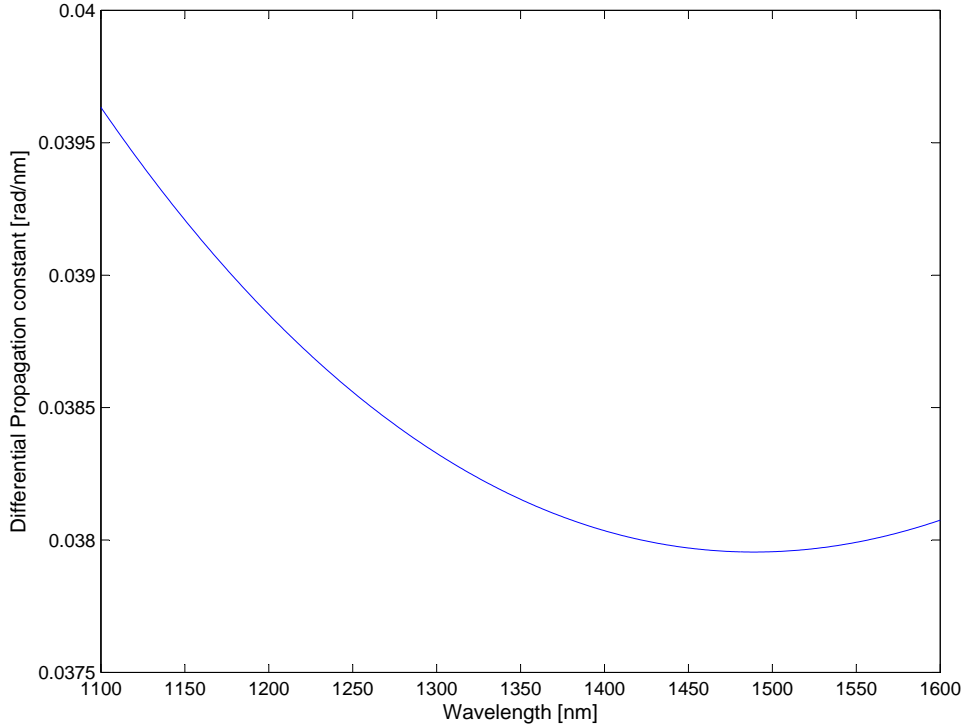
Figure 3.9: Variation of the differential propagation constant with wavelength for the $LP_{0,12}$ cladding mode for an unperturbed SMF-28 fibre

phase-matching wavelength to shift to a higher value because the period of the grating is unchanged. This is equivalent to compressing the ω-axis in a β-plot that results in a wavelength shift to higher values.

On the other hand, operation at wavelengths longer than the equalisation wavelength, $\lambda^{(m)} > \lambda_0^{(m)}$, causes the phase-matching wavelength to shift to smaller values. Thus in order to use the β-plots one has to know the relative location of the coupling wavelength with respect to the equalisation wavelength. The wavelength shifts predicted by the β-plots are only valid if the coupling wavelength is smaller than the equalisation wavelength[23].

The above discussion is clearer if we consider the relationship between the coupling wavelength and the grating period. By substituting Equation 3.29 into 3.31 and re-arranging for Λ, one obtains:

$$\Lambda = \frac{2\pi}{\Delta\beta^{(m)}} \tag{3.34}$$

Hence from $\Delta\beta^{(m)}$ versus wavelength one can obtain a spectral variation of grating period. This is shown in Figure 3.10. To obtain the coupling wavelengths for a given grating period we draw vertical lines from the x-axis to intersect the curve. As expected the curve has a positive slope for $\lambda^{(m)} < \lambda_0^{(m)}$ and a negative slope for $\lambda^{(m)} > \lambda_0^{(m)}$. One terms the range of wavelengths at which the slope of the characteristic curve is positive

as the "normal" region of operation, while the part of the spectrum where the slope of
the characteristic curve is negative, is termed the "anomalous" region[23].
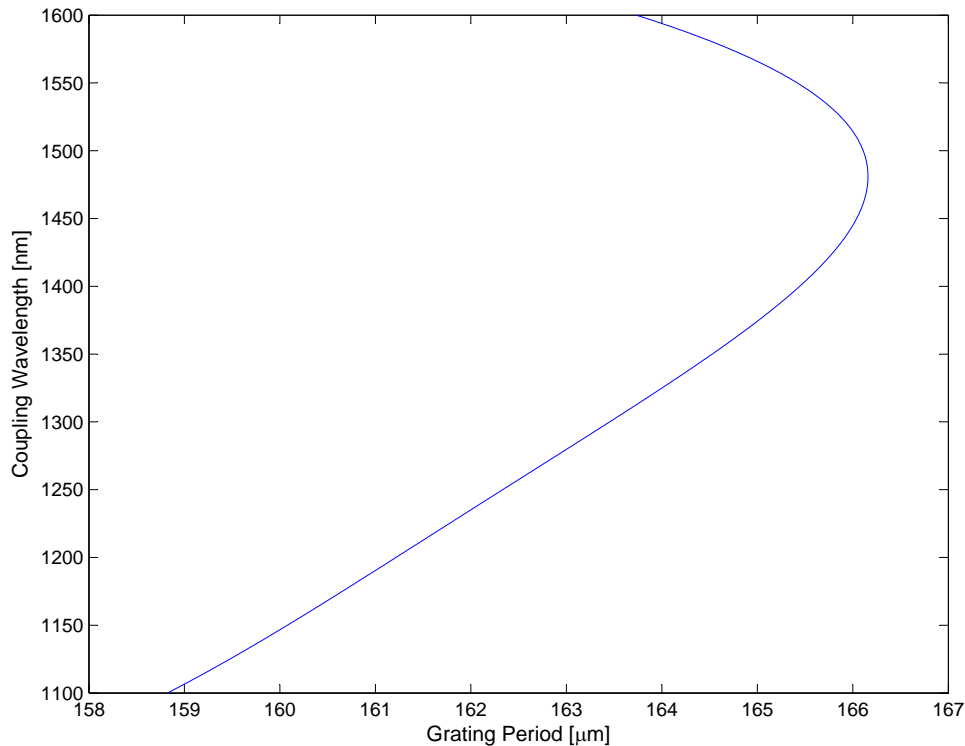
Figure 3.10: A characteristic curve for m = 12 in an SMF-28 Fibre

The above argument and Figures imply that a particular choice of grating periods can
result in two resonance bands - one in the normal region and one in the anomalous region.
Typical long-period gratings possess periods that induce coupling to cladding modes in
the normal region. Figure 3.10 reveals there is a maximum grating period that can induce
coupling from the guided mode to a given cladding mode and we will call this maximum
period the equalisation period for the mode order m, $\Lambda_0^{(m)}$, since it corresponds to the
equalisation wavelength for an unperturbed fibre[23]. For the $LP_{0,12}$ cladding mode this
period is $\Lambda_0^{(12)} = 166, 1$ μm.

We thus see that the characteristic curves provide a useful tool to analyse the properties
of gratings. For a given period, the location of the resonance bands can be found and if a
band is desired at a certain wavelength, the appropriate period can be selected to obtain
a particular separation between any two bands[22].

3.3   Conclusions

This chapter discussed the principle of operation of long-period gratings that couple the
fundamental guided mode to discrete forward propagating cladding modes[22]. The con-
cept of β-plots were used to explain the operating mechanism of these gratings. An

analytical model was discussed which enables one to obtain the characteristic curves for different fibres. It was shown that the long-period gratings can operate in two spectral regions - normal and anomalous.

For most applications, the grating period is selected such that the coupling wavelength grows on increasing the periodicity. In this case, the normal region of operation, the group index of the guided mode is larger than that of the corresponding cladding mode involved in coupling. For the anomalous region, the cladding mode has a higher group index and thus the slope of the coupling wavelength versus grating period curve is negative.

Chapter 4

Properties of Long-Period Gratings

This chapter outlines the different methods of fabricating long-period gratings. The effects of Hydrogen diffusion from the grating after fabrication is analysed and it is shown that the grating spectrum can be stabilised by annealing it at high temperatures[22]. Also discussed is the etching of long-period gratings.

4.1   Fabrication Methods

Three methods of fabrication are discussed. The first two involve the use of ultra-violet radiation while the third employs a CO_2 laser for grating production. The fabrication set ups are illustrated and the relative advantages and limitations of the three methods are investigated.

The germanium-doped fibres used for grating fabrication are Hydrogen loaded to enhance the index change during the photo sensitivity process. The loaded fibres are stored at either low temperature or high pressure to prevent out-diffusion of Hydrogen[23].

4.1.1   Excimer Laser Method

The most popular method used to fabricate long-period gratings is by employing a pulsed excimer laser as is illustrated in Figure 4.1[22]. Amplitude with rectangular transmittance functions are imprinted on chrome-plated glass and have a 100 mJ/cm^2/pulse optical threshold damage level[22].

Masks with different periods can be produced on the surface of a glass plate resulting in economical mask fabrication and provide easy access to different periodicities. Typically the duty cycle of the rectangular function is about 50% and the length of the mask can be varied bwteeen 1 and 3 cm.

A length of between 3 and 4 cm of the acrylate jacket is removed in the middle of a hydrogen-loaded fibre and the fibre is aligned behind the amplitude mask of appropriate period. The fibre is supported on both sides of the bare region to prevent bends from influencing the coupling to cladding modes. Light from a broadband source such as an LED is launched from one end of the fibre while the normalised transmission spectrum is
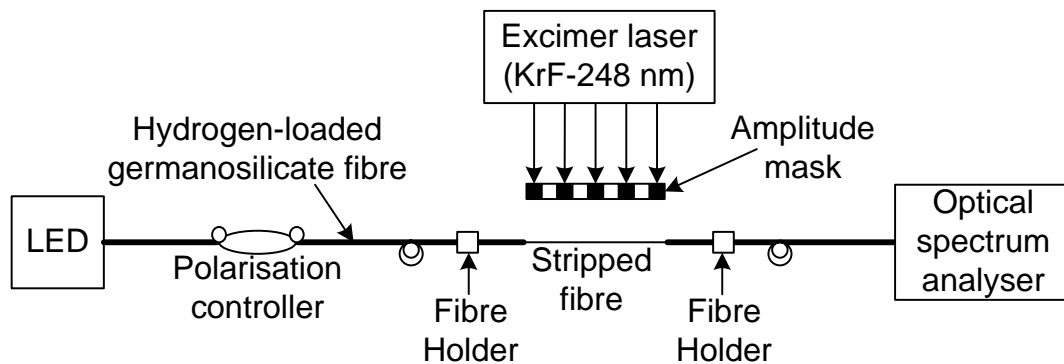
Figure 4.1: Setup to fabricate long-period gratings using an excimer laser[22]

obtained on an optical spectrum analyser (OSA) display[22]. During the writing process the resonance bands shift to longer wavelengths and this shift can be attributed to the increase in guided mode effective index[23].

The major advantage of using the excimer laser-based method is that a number of gratings with the same period may be easily batch produced[22]. The mass production is done by placing more than one single fibre behind the amplitude mask.

4.1.2   Continuous-Wave Laser Method

This method utilises a continuous-wave (CW) UV source to manufacture the gratings. The dimensions of the CW beam in a frequency-doubled (FRED) argon-ion laser typically range in the hundreds of micrometers[23]. By placing the fibre behind an amplitude mask of rectangular transmittance function, refractive index modulation of the core can only be achieved over the length equal to the beam dimension of the UV source along the fibre axis[23]. Thus the small beam size of the CW laser can severely limit the grating length and result in location of the resonance bands at undesired wavelengths. This limitation can be overcome by scanning the UV beam along the axis of the amplitude mask of the fibre.

The method, due to the translation of the CW beam laser, has the advantage that any non-uniformity in its profile along the axis of the fibre will be averaged out over the length of the grating. The disadvantage of the method is the laser translation and writing time is approximately 10 to 20 minutes and the method is limited to one grating at a time.

4.1.3   CO$_2$ Laser Method

This technique uses the concept that refractive index changes can be introduced in hydrogen-loaded germanosilicate fibres by simple thermal treatment[23]. The set up required to fabricate long-periods gratings using thermal exposure is shown in Figure 4.2.

The CO$_2$ output through the lens simply serves to increase the temperature of the fibre
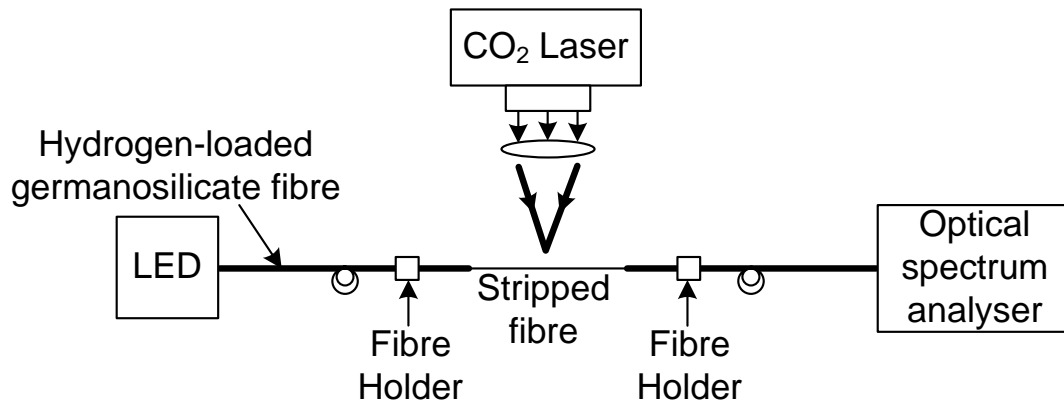
Figure 4.2: Setup to fabricate long-period gratings using a CO_2 laser

and hence index changes are produced due to thermal effects[23]. The use of cheap CO_2 lasers without resorting to UV-based lasers and amplitude masks drastically reduces the cost of manufacturing of gratings.

The method can be used to manufacture a number of gratings simultaneously by arranging the fibres parallel to one another and translating the CO_2 beam across the fibres, forward and then across once again.

The disadvantage of the method is the inability to precisely control the grating period due to the diffusion of thermal energy and this effect is expected to be more pronounced for smaller gratings.

Another method utilising the CO_2 laser is a two step process where the pulsed laser is used to create periodic removal of material in the outer cladding surface[23]. The separation between the resulting V-grooves determines the period Λ of the grating. The second step is to anneal the fibre with an electric arc which causes the core to deform in the regions of the grooves[23]. The periodic micro bending of the core causes the light to couple to forward-propagating cladding modes that are not circularly-symmetric.

We thus see that long-period gratings can be fabricated by a number of methods. Pulsed and continuous-wave exposure from UV sources can be used to write gratings using inexpensive amplitude masks.

4.2   Annealing of Long-Period Gratings

Typically the amount of hydrogen present in an optical fibre for grating manufacture is far in excess of that required to achieve a given refractive index change[23]. Thus following the completion of the writing process there is a finite amount of unused hydrogen remaining in the cladding that can significantly influence the grating transmission spectrum. This section analyses the effect of residual hydrogen and shows that the grating

spectrum can be stabilised by annealing it at high temperatures[22].

Before modulating the index of the fibre core, the hydrogen concentration in the core can be assumed to be uniform. The process of index modulation uses hydrogen in only the regions exposed to UV radiation or thermal energy. This means the cladding and the unexposed parts of the core possess higher concentrations of hydrogen once the writing process is terminated. To maintain equilibrium hydrogen starts to diffuse from the high concentration regions to the exposed areas of the core and also out to the surroundings[23].

The diffusion process raises the average index of the core and results in an increase in the value of effective index of the guided mode[22]. The diffusion into the exposed part of the core lasts a few hours at room temperature until equilibrium is reached. At equilibrium, hydrogen concentration is uniform throughout the fibre but still larger than that in the surroundings. The concentration imbalance causes hydrogen to diffuse from the fibre into the atmosphere. The diffusion from the fibre reduces the average index of both the core and the cladding. The process of out-diffusion is very slow at room temperature and usually takes hundreds of hours to be completed.

The diffusion process in which hydrogen initially reaches equilibrium in the fibre and then moves to the outer atmosphere, introduces a time delay of a few weeks between the fabrication process and the instant when the grating spectrum stabilises. The prolonged waiting period might not be feasible during commercial production of these gratings if production time needs to be minimised. To overcome this limitation, hydrogen can be removed from the fibre in a matter of a few hours by high temperature annealing[22].

The annealing serves to diffuse hydrogen from the grating into the atmosphere more than two orders of magnitude faster than at room temperature and hence provides short-term stability to the grating spectrum. The annealing of of long-period gratings following the writing process is an integral part of the complete manufacturing process.

Annealing the grating essentially serves two major purposes - removal of residual hydrogen as well as decay of unstable UV sites in the grating[22]. The annealing process involves heating the gratings to an elevated temperature for a period dependent on the expected lifetime of the device. The annealing temperature varies from 150 °C to 200 °C, while the duration of this thermal treatment is between 10 and 20 hours.

In this section we discussed the fabrication of long-period gratings. Three different methods of manufacture were outlined and their limitations and advantages were discussed. High temperature annealing was discussed which stabilises the grating spectrum and removes the residual hydrogen and certain UV-induced defects[22].

4.3   Etching of Long-Period Gratings

One recalls that the effective index of the cladding modes is a strong function of the cladding diameter. Thus chemically etching the cladding in the region surrounding the

grating is expected to alter its transmission spectrum by reducing the effective indices of the cladding modes.

One can etch gratings using a strong solution of hydrofluoric acid (HF) for a period of approximately 90 seconds. The effective indices of the higher order cladding modes undergo a larger change with change in the cladding diameter[23]. The magnitude of the shift is a function of the fibre parameters, the etching depth and the order of the resonance bands[23]. Etching a grating will enhance the refractive index sensitivity of long-period gratings which will discussed in more detail in due course.

4.4   Conclusions

In this chapter the three different methods of fabricating long-period gratings were outlined. The first two use radiation from pulsed or continuous-wave UV laser and require either amplitude masks or slits to obtain the rectangular index modulation in the fibre core. The third technique uses the thermal sensitivity of hydrogen-loaded fibre to obtain long-period grating and employs inexpensive CO_2 lasers for batch-production of gratings.

The effects of residual Hydrogen diffusion from the grating after fabrication was analysed and it was shown that the grating spectrum can be stabilised by annealing it at high temperatures. Also discussed was the etching of long-period gratings and the effect this has on the grating transmission spectrum.

Chapter 5

Long-Period Grating Sensors

5.1 Introduction

In Chapter 2, the basic properties of long-period gratings were introduced. These fundamentals were then extended in Chapter 3 to develop an analytical model of long-period gratings. One can now summarise the functioning of long-period gratings as devices that couple light from the guided mode to discrete cladding modes and result in attenuation bands whose spectral locations are functions of the grating period and the differential effective index. Thus any variation in the effective indices of these modes or in the grating period serves to modulate the phase-matching wavelengths. This chapter introduces the sensing capabilities of long-period gratings based on the above mentioned principle.

Firstly the basic operating principle of long-period grating sensors is discussed and the mechanism behind the spectral shifts in the resonance band is explored. It is shown that for a given fibre the wavelength shifts are strong functions of the grating period and the order of the corresponding cladding mode. The dependence of the temperature sensitivity on the grating period and the order of the cladding mode is investigated and furthermore long-period gratings are shown to be highly sensitive to index changes of the medium surrounding the bare cladding[29] - their intended application in this instance.

Also demonstrated is the spectral shift induced by ambient index variations can be enhanced by etching the cladding surrounding the long-period grating. Typically, an optical spectrum analyser is required at the output end to determine the wavelength shift and hence the magnitude of the applied perturbation. A simple demodulation scheme for long-period grating sensors that employs the conversion of the spectral shift to an intensity modulation is demonstrated[29].

5.1.1 Principle of Operation

Typically, the periodicity of long-period gratings range between 100 μm to 1 mm and this results in a segment of optic fibre where light can either be propagated through the fibre core, as normal, or coupled into the cladding and propagated through the cladding. Once in the cladding, the light decays quickly due to scattering losses, leaving loss bands in the guided core mode observed at the output and as a result, dips are created in the

transmission spectrum at wavelengths where coupling occurs. Each attenuation band where coupling occurs is referred to as a resonance wavelength.

An unusual, but useful, feature of LPGs is their sensitivity to the index of refraction of the material surrounding the cladding glass in the grating region. This arises from the dependence of the attenuation band wavelengths on the effective index of refraction of the cladding modes, which depends on the index of refraction of the surrounding environment[19, 22].

Regarding the depth of the attenuation bands, different factors influence this value but the two most important ones are[20]:

1. The cross coupling coefficient between the core mode and the cladding mode that couples at that resonance wavelength.

2. The length of the grating.

Two specific cases exist:

1. That the ambient refractive index is lower than that of the cladding. As the ambient refractive index approaches that of the cladding, the sensitivity of the resonance wavelength to variations of the ambient refractive index is higher[20].

2. That the ambient refractive index exceeds that of the cladding. The core couples with radiation modes and the dependence of the resonance wavelength on the ambient refractive index is not so as acute. Instead, the resonance depth is more dependent on this parameter for values close to the refractive index of the cladding[20].

The sensing mechanism can be explained on the basis of the phase-matching condition which results in a coupling wavelength λ:

$$\lambda = (\delta n_{eff})\Lambda \qquad (5.1)$$

Where: Λ is the grating periodicity

            δn_{eff} is the differential effective index at wavelength λ between the guided and cladding mode. $(\delta n_{eff} = n_{eff} - n_{cl})$.

For a fibre with n_1, n_2 and n_3 ($n_1 > n_2 > n_3$) as the core, cladding and ambient indices, $n_2 < n_{eff} < n_1$ and $n_3 < n_{cl} < n_2$. Equation 5.1 reveals that the coupling wavelength is a function of the effective indices of the guided and cladding modes and the grating period. The effective indices depend on the fibre parameters such as the core and cladding refractive indices and the radii. External perturbations such as strain and temperature modulate various optical fibre parameters and the grating period, and hence induce displacements in the coupling wavelengths.

Since the spectral variation of the effective indices of the cladding modes involved in coupling are unique, the corresponding resonance bands are expected to possess distinct wavelength shifts. The effective index of the cladding modes are also functions of the

ambient index of refraction and hence ambient index changes are also expected to shift the phase-matching wavelengths of different resonance bands. Since each cladding mode has a unique change in the value of its effective index, the spectral shift of a band will depend on the order of the corresponding mode. Thus the principle operating mechanism of long-period grating sensors is based on the modulation of the effective indices of the core and cladding modes and/or the grating periodicity by the external perturbation[23]. Also the sensitivity to the external index increases with decreasing cladding radius[30].

Consider a perturbation ξ that acts on the region of fibre that contains a grating with period Λ. The objective is to find the wavelength shift per unit perturbation change $\frac{d\lambda}{d\xi}$ for the given grating. Using the chain rule of derivatives in Equation 5.1 one obtains[23]:

$$\frac{d\lambda}{d\xi} = \frac{d\lambda}{d\left(\delta n_{eff}\right)} \frac{d\left(\delta n_{eff}\right)}{d\xi} + \frac{d\lambda}{d\Lambda} \frac{d\Lambda}{d\xi} \tag{5.2}$$

As expected, the wavelength shift is a function of the change in the differential effective index per unit perturbation $\frac{d\left(\delta n_{eff}\right)}{d\xi}$, and also of the change in the grating period per unit perturbation $\frac{d\Lambda}{d\xi}$. The factor $\frac{d\lambda}{d\Lambda}$ is a function of the fibre parameters, the grating period, the order of the resonance band and the writing and annealing conditions[30].

The dependence on the writing conditions arises from the fact that for a given modal order, the coupling wavelength is a function of the peak UV or thermal-induced index change Δn, which in itself is dependent on the laser power, the time of exposure and the annealing temperature and duration. The analysis, unless otherwise stated, will consider only gratings with the same Δn for all values of periods and lengths, and hence the focus will be on analysing the differential response based on grating periodicity and other factors such as ambient index of refraction.

In Section 3.2.3 we had shown that the characteristic curves of gratings written in different fibres are dependent on fibre parameters such as the core and cladding indices and radii. Hence the slope of a characteristic curve $\frac{d\lambda}{d\Lambda}$ is a function of the various fibre parameters and can be expressed as[23]:

$$\frac{d\lambda}{d\Lambda} = \frac{\left(\delta n_{eff}\right)^2}{\delta n_g} \tag{5.3}$$

Where: δn_g is the differential group index between the guided and cladding modes given by Equation 3.3.

Thus, if the effective indices of the guided and cladding modes and their spectral variation are known, the parameters $\frac{d\lambda}{d\left(\delta n_{eff}\right)}$ and $\frac{d\lambda}{d\Lambda}$ in Equation 5.2 can be determined. Assuming then that the effect of the perturbation on the differential effective index $\frac{d\left(\delta n_{eff}\right)}{d\xi}$ and on the grating period $\frac{d\lambda}{d\Lambda}$ are known, the induced wavelength shift can be determined. This will be the main principle behind analytical modelling of long-period grating sensors.

The differential group index δn_g between the guided mode and a particular cladding mode can be positive or negative depending on the fibre parameters and the coupling wavelength. The part of the spectrum where the value of δn_g is positive is called the normal region of operation while the spectral range with negative δn_g is termed the anomalous operating region. Using Equation 5.3, we observe that if $\frac{d\Lambda}{d\xi}$ maintains its sign, the second terms on the right hand side of Equation 5.2 will have opposite polarity for these two different regions[23]. Furthermore, for operation around the equalisation wavelength, this term will be larger for the same change in period since the slope of the corresponding characteristic curve approaches infinity[23].

Equation 5.2 can be divided into two categories of influence on the spectral shift. The first term on the right-hand side of the equation is termed the material contribution since the change in the differential effective index typically arises from the modulation of the material properties of the fibre such as the core and the cladding refractive indices[23]. The second term is called the waveguide contribution since it affects the guiding properties of the fibre by introducing a change in the grating periodicity[23]. The overall shift per unit perturbation $\frac{d\lambda}{d\xi}$ depends on the relative magnitudes and polarities of the material and waveguide contributions. For a fibre with a given period, these two effects might counter-balance to result in gratings that are independent of a certain perturbation.

5.1.2 Refractive Index Sensors

In this section we introduce long-period gratings as highly sensitive refractive index sensors. The principle of operation of such sensors is described and we show that etching the cladding radius enhances the wavelength shift due to ambient index changes in long-period gratings. The response of temperature-insensitive gratings to changes in ambient index is also analysed.

Conventional fibre optic refractive index sensors typically use some form of modification of the cladding to gain access to the evanescent field of the guided mode. For example, surface plasmon sensors require polishing the fibre cladding and depositing a thin layer of appropriate metal (such as aluminium) on the polished surface[31]. Limitations of this device include strong polarisation sensitivity and questionable repeatability and mechanical strength. In a subsequent section we will show that long-period gratings are highly sensitive refractive index sensors and can be implemented without sacrificing the integrity of the fibre[29].

Theoretical Analysis

In Chapter 3, we demonstrated that the effective indices of the cladding modes are strong functions of the index of refraction of the medium surrounding the cladding (n_3). Any change in this ambient index serves to modulate the effective index of the cladding modes (n_{cl}), with the higher order modes undergoing larger variations.

Since the coupling wavelength λ corresponding to a particular cladding mode is dependent on n_{cl} through the phase matching condition (Equation 5.1), a change in n_3 will

effectively vary the value of λ. The shift in the coupling wavelength can be determined using an optical spectrum analyser to produce a simple index of refraction sensor. For most applications, the index of refraction measurements need to be performed in the range 1,33 (refractive index of water) to about 1,45[23], in other words the sensing capability is most effective in the region in which the ambient index is less than the effective index of the cladding mode. In this particular intended application, however, the region of sensing is lower than the effective index of the cladding mode but also much lower than the refractive index of water. In Section 6.2, it is shown that for a 1% concentration of SF_6, the expected refractive index would be 1,00001677 - very close to the refractive index of air.

To begin we will assume that the fundamental guided mode is well confined to the fibre core and is not influenced by changes in the ambient index. This approximation is well justified for the large cladding radii of standard fibres ($b = 62,5$ μm). Also since the grating period remains unchanged under the effect of the ambient index n_3 ($\frac{d\Lambda}{dn_3} = 0$), the shift in a band is given by[23]:

$$\frac{d\lambda}{dn_3} = \frac{d\lambda}{dn_{cl}} \frac{dn_{cl}}{dn_3} \qquad (5.4)$$

Since the change in the effective index of a particular cladding mode with the ambient index ($\frac{dn_{cl}}{dn_3}$) is dependent on the order of the cladding mode, each resonance band of a grating is expected to undergo a distinctive shift. Furthermore, the polarity of the wavelength shift will be a function of the region of grating operation[23]. For operation in the normal region, the increase in the effective index of the cladding mode serves to decrease the coupling wavelength ($\frac{d\lambda}{dn_{cl}} < 0$), whereas the effect is opposite in the anomalous region ($\frac{d\lambda}{dn_{cl}} > 0$)[23]. The increase in n_3 towards the value of the effective index enhances n_{cl} ($\frac{dn_{cl}}{dn_3} > 0$) and thus results in shifts in opposite directions for the two regions of operation.

The magnitude of the shift is expected to increase as n_3 approaches n_{cl}, due to the non-linear change in $\frac{dn_{cl}}{dn_3}$[23]. When the ambient index equals the effective index of the cladding mode, the outer cladding interface disappears and the coupling of the guided mode is expected to occur to a continuum of guided modes[23]. Since each cladding mode has a unique effective index, the corresponding resonance bands should disappear at different values of the ambient index. For example, the higher order cladding modes will encounter the matched cladding interface at smaller values of ambient indices, as compared to modes with lower m.

We will now use the analytical model to predict the effect of the grating period, the order of resonance band, the writing conditions and the cladding radius on the sensitivity to surrounding refractive index changes. In the following analysis, we assume that the medium outside the cladding extends to infinity, so that the simplified model to evaluate cladding mode effective indices can be employed.

Figure 5.1 shows the ambient index induced wavelength shift in the resonance band corresponding the the 7th order mode. The shifts are plotted as a function of the grating period for three distinct values of n_3 assuming a peak index change $\Delta n = 5 \times 10^{-4}$.

As can be seen, the wavelength shift is negative for these values of ambient index and increases with grating period. The enhancement in the refractive index sensitivity can be attributed to the greater increase in the cladding mode effective index at longer wavelengths and hence at larger periods, for the normal region of operation[23]. The shift with increase in ambient index is also non-linear since the sensitivity to index changes grows as the effective index of the cladding mode is approached.
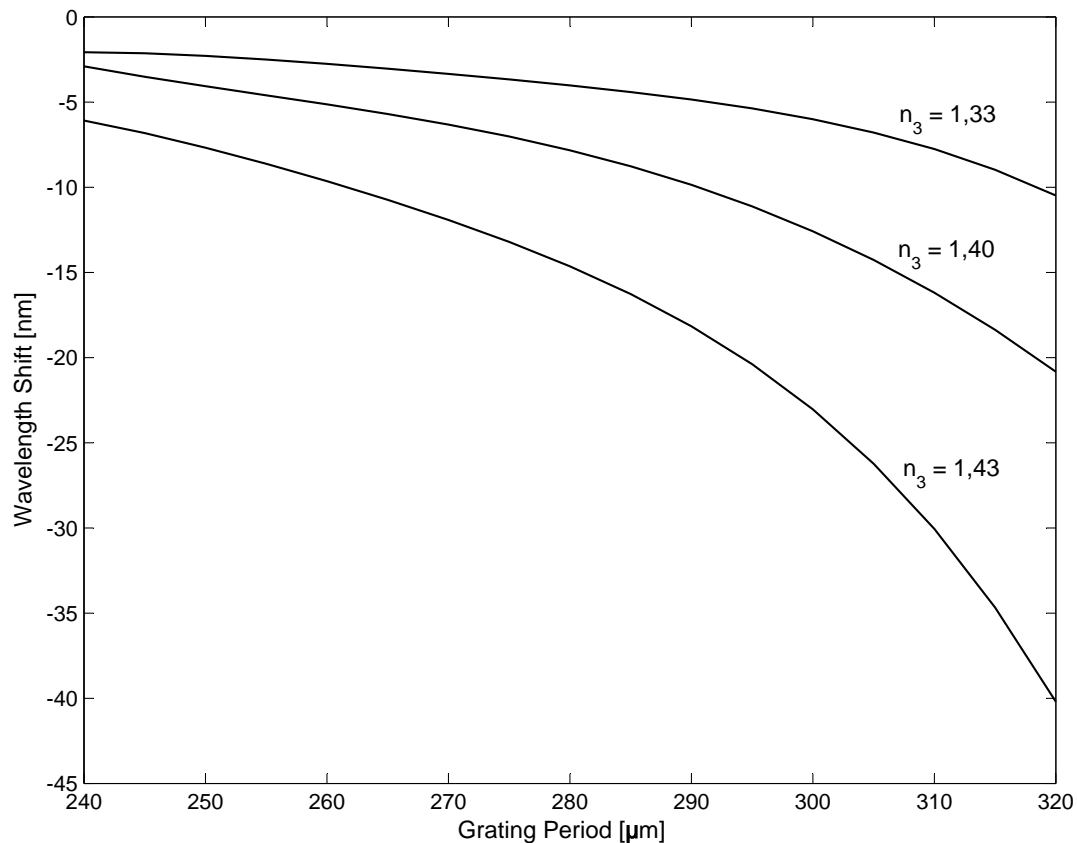
Figure 5.1: Wavelength shift as a function of period for three different values of ambient index n_3. The shift for each index value is measured with respect to the wavelength location at $n_3 = 1$.

For a given wavelength, the effective index of cladding modes reduces with an increase in the modal order m, which predicts that the matching of the ambient index and the cladding mode effective index will occur at smaller and smaller values as m increases[23]. Thus the distinct resonance bands corresponding to higher order modes will disappear for smaller values of n_3, than those for modes with smaller mode orders. This can help the designer tailor the refractive index sensitivity of the fibre depending on the application. For example, if the maximum refractive index sensitivity occurs for $n = 1, 44$, this value can be lowered by using gratings with smaller periods. The ability to selectively tune the overall refractive index induced shifts and the index corresponding to the maximum sensitivity, is an attractive feature of long-period grating-based refractive index sensors.

Figures 5.2 and 5.3 show shifts in a spectrum of a grating of $\Lambda = 320\ \mu$m. Figure 5.2 shows the grating subjected to ambient refractive indices of $n_3 = 1$ and $n_3 = 1,44$ while Figure 5.3 shows the shifts under influence of refractive indices between $n_3 = 1,3$ and $n_3 = 1,44$. The spectral shifts in all resonance bands are toward shorter wavelengths since a grating with the given period operates in the normal region. The wavelength displacements are measured with respect to the locations of the unperturbed bands ($n_3 = 1$). As predicted, the magnitude of shift increases with the order of the resonance band, from A to F.
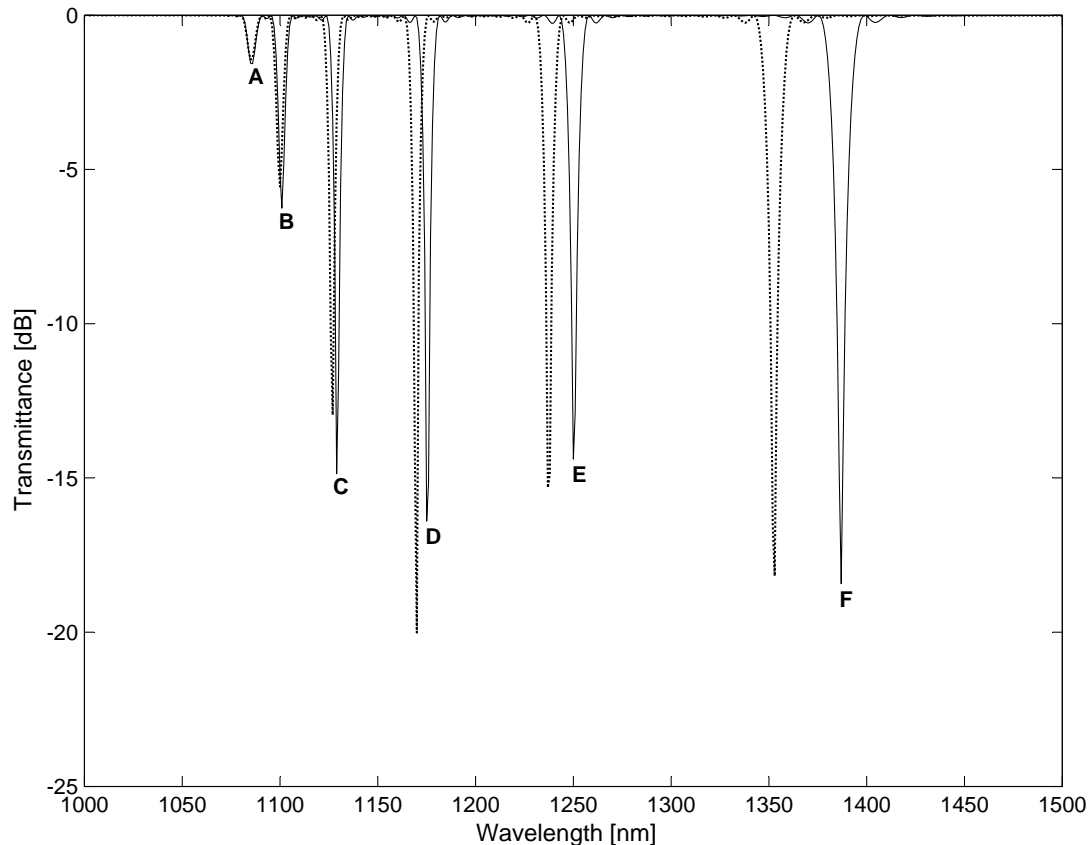
Figure 5.2: Transmission spectrum of a long-period grating of $\Lambda = 320\ \mu$m plotted at refractive indices of 1,0 (Solid) and 1,44 (Dotted). Clearly visible are the greater shifts in higher order modes (For example resonance band F).

The effective index of the cladding mode is a strong function of the cladding radius[23], hence the response to ambient index changes is expected to depend on the size of the cladding. For instance, reducing the cladding diameter, will offer greater access to the modal fields of the cladding modes and result in larger spectral shifts with changes in the index of the surrounding medium. This is assuming that the guided mode is itself not affected by the etching process.

Figure 5.4 displays the spectra from a grating equivalent to Figure 5.2 except for the fact that the cladding diameter has been reduced to 100 μm. One can see, when comparing Figures 5.2 and 5.4, that the resonance peaks have shifted to higher wavelengths with
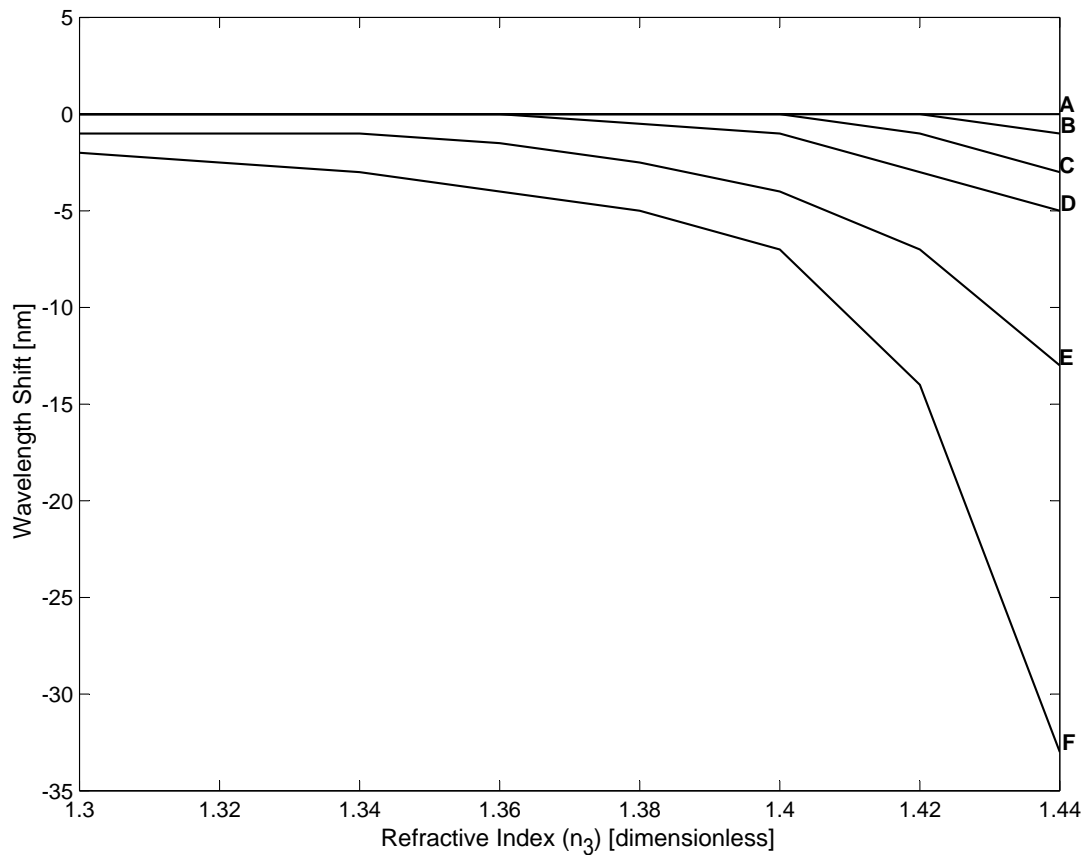
Figure 5.3: Theoretically determined shifts in six resonance bands of a long-period grating of $\Lambda = 320 \ \mu$m. The resonance bands A, B, C, D, E and F are shown in Figure 5.2 and are located at 1086 nm, 1101 nm, 1129 nm, 1175 nm, 1250 nm and 1387 nm respectively. The shifts are measured with respect to the location at $n_3 = 1$ and the graph is composed of a few points due to the calculation involved in establishing each point.

reduced cladding radius due to the increased access to the modal fields. Also the relative shifts of the 6th order cladding mode is equivalent in the two notwithstanding the fact that the change in refractive indices are not equivalent. This demonstrates how the sensitivity of a refractive index long-period grating sensor can be increased by etching of the cladding and thus chemical etching of the cladding diameter is a simple method to manipulate the refractive index sensitivity of a long-period gratings following the fabrication process[30].

In this section we carried out a detailed investigation of the sensitivity of long-period gratings to index of refraction changes of the medium surrounding the bare fibre. It was shown that the wavelength shift is a function of the grating period, the order of the cladding mode and the cladding diameter.
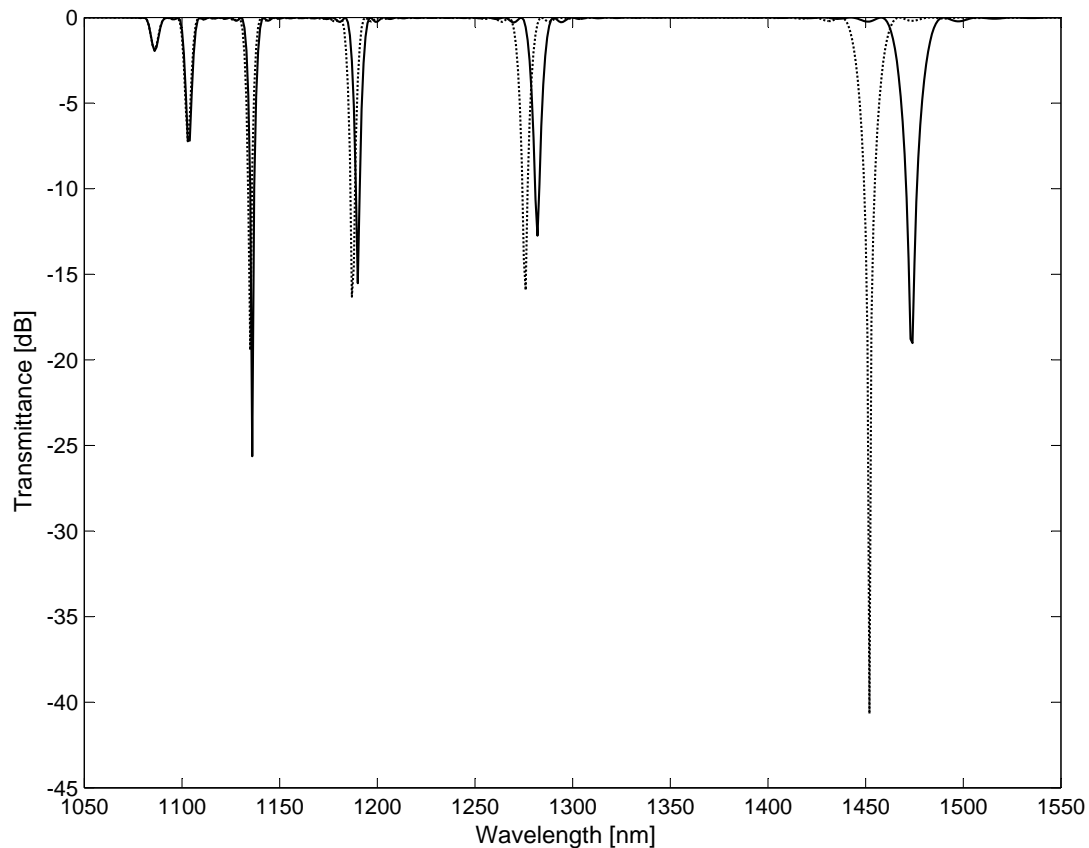
Figure 5.4: The transmission spectrum of a $\Lambda = 320$ μm with a reduced cladding diameter = 110 μm. The solid spectrum is for $n_3 = 1$ and the dotted spectrum represents $n_3 = 1,42$.

5.1.3   Temperature-Insensitive Gratings

Many researchers have investigated the temperature sensitivity of long-period gratings and have obtained varying degrees of success regarding temperature insensitivity of long-period gratings[23, 24, 29, 32, 33]. As an example of the sensitivity and the resulting impact on the refractive index sensing, the author of [23] presents a grating with a peri-odicity $\Lambda = 280$ μm and shows for a high order mode coupling a shift of 0,093 nm/°C.

In this sub-section the operation of gratings with reduced temperature sensitivity operating in the anomalous region in standard telecommunications fibres is discussed. A grating operating in the anomalous region experiences shifts to lower wavelengths with increased temperature[29], thus if the refractive index sensitivity can be enhanced through the use of gratings operating in the anomalous region, temperature effects will be reduced.

A grating with $\Lambda = 166$ μm operates in the anomalous region. With an increase in ambient refractive index the wavelength shift that occurs, occurs to longer wavelength due to the operation in the anomalous region. The resonance shifts experienced by this grating are larger than gratings operating in the normal region, as the coupling is to higher order

cladding modes and so undergoes larger shifts in its effective index, as compared to lower order modes[23]. Due to the larger shifts due to ambient refractive index changes and shifts due to temperature fluctuations having reduced shifts, in the opposite direction, sensing is possible provided calibration is provided. This calibration will depend on the specific environment the sensor is intended for.

In this section we have shown that gratings fabricated with appropriate periods in standard optical fibres can be made to have very small temperature sensitivity. These gratings typically have periods less than 200 μm and hence operate in the anomalous region.

5.2   Demodulation and Multiplexing

In the preceding section in this chapter the sensitivity of long-period gratings to external perturbations, especially refractive index, was discussed. It was shown that these devices possess large measurand-induced spectral shifts in the unperturbed locations of the resonance bands. Also these sensors are simple and economical to mass produce and hence incorporate numerous desired characteristics of fibre optic sensors. The overall cost of a system using long-period gratings will be a function of the signal processing required to extract the perturbation and the ease of multiplexing a number of such transducers[29]. In this section we show that long-period grating-based sensors can be implemented with simple demodulation methods. A few methods to effectively multiplex these gratings are also proposed.

5.2.1   Demodulation

In the previous sections we had restricted our discussion to the use of optical spectrum analysers to determine the shifts in the resonance bands of long-period gratings under the influence of a perturbation. Although modern day spectrum analysers are smaller than their traditional counterparts, the cost of these measurement systems is still a major limitation. In this sub-section a few schemes are discussed which convert the wavelength shifts of the bands into intensity modulations which can be measured using a simple photo-detector.

The wide resonance bands in long-period gratings can be used advantageously to implement a number of different methods to monitor the shift. The basic setup for the first scheme is shown in Figure 5.5. Light from an LED is launched into the fibre with a long-period grating. Let a resonance band of the long-period grating be centred at a wavelength λ_1, as depicted in Figure 5.6.

At the output of the fibre an optical band-pass filter is placed to transmit a small spectrum of the grating signal. The pass-band of the optical filter is centred at a wavelength λ_f, on one side of λ_1, such that it can extract a shift in the transmitted intensity of the LED[23]. The exact spectral position of the filter determines the resolution and dynamic range of the sensor. If the filter is located in the region where the grating spectrum has a high slope or variation, highly sensitive measurements can be made[29]. For example
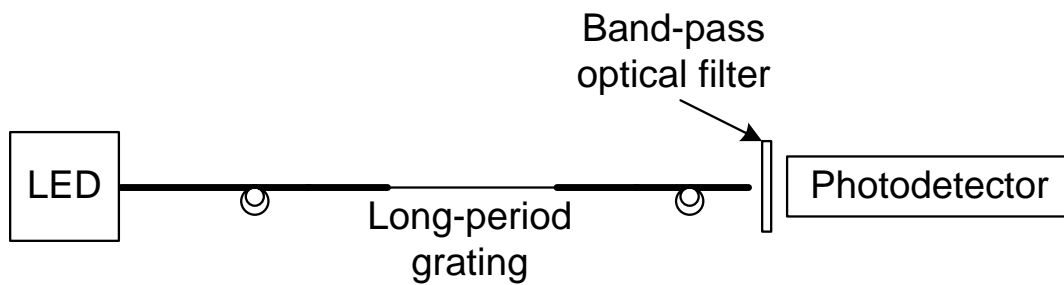
Figure 5.5: Simple demodulation scheme for long-period grating sensors.
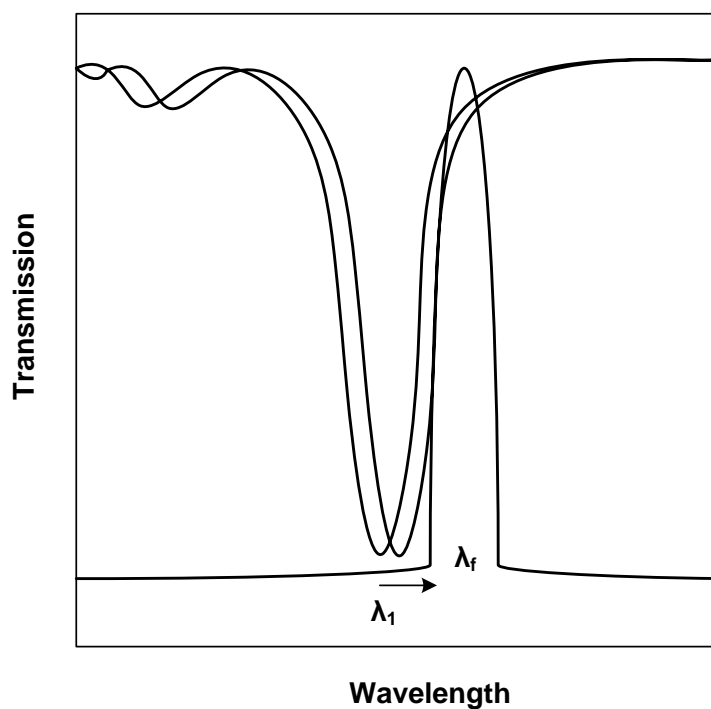
Figure 5.6: Shift in the spectral position of the resonance band (centred at λ_1) to a higher wavelength under external perturbation. The transmission spectrum of the optical filter, with pass-band centred at λ_f is also shown.

in Figure 5.5, the decrease in the output intensity with a shift in the band to longer wavelengths can be detected by simply employing a photo detector.

Another similar demodulation scheme uses a 3-dB coupler to interrogate a long-period grating in series with a spectrally overlapping fibre Bragg grating, as shown in Figure 5.7[23]. The Bragg grating is shielded from the ambient perturbation and thus a shift in the long-period grating band is converted to an intensity change in the return leg of the coupler. The advantage of using a reflective configuration is that since the light makes a double pass through the long-period grating, the sensitivity of the system is effectively doubled[23]. Optical band-pass filters can be expensive and might be susceptible to tem-

perature changes. Bragg gratings, on the other hand, are themselves sensitive to strain and temperature changes, and hence need to be isolated from such perturbations.
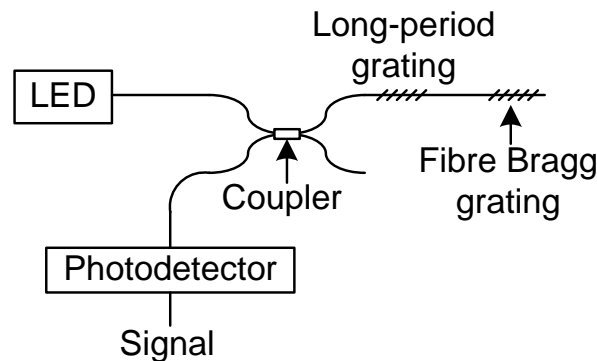
Figure 5.7: Demodulation of a long-period grating by employing a fibre Bragg grating. The reflection spectrum of the Bragg grating overlaps the resonance band in a manner similar to the optical filter in Figure 5.6[23].

The second method to effectively detect the shift in the resonance bands involves the use of a laser diode as an optical source. The narrow line width laser source replaces the LED and the optical filter in the first method. The centre wavelength of the laser diode is located on the region of a resonance band that undergoes a change in the transmitted intensity when the perturbation is applied[29]. Although a laser diode is typically more expensive than a standard LED, the temperature-induced shifts in its centre wavelength can be detected and controlled using a number of schemes that employ feedback[34].

It has thus been demonstrated that long-period gratings sensors can be used in conjunction with simple demodulation schemes. The wide spectral width of these gratings permits the use of laser diodes at specific wavelengths as optical sources[29]. The signal processing components may simply include a photo detector with an integrated circuit that converts the intensity change into the magnitude of the applied perturbation on the basis of a calibration curve[23]. The limitation of this scheme is that the system is now susceptible to all external factors that change the transmitted intensity and furthermore, a separate calibration curve might be required for each sensor.

The first drawback can be overcome by normalising the sensing signal to a reference signal from another laser diode that is located at a wavelength outside the resonance band of the grating[23]. A big advantage of these demodulation schemes is that the bandwidth of the sensing system is increased a number of times over the methods that employ a spectrum analyser, thus these techniques enable real-time measurements of perturbations that change rapidly with time.

The temperature-insensitive gratings discussed previously can also be used with this demodulation scheme to minimise thermal cross-sensitivity. Such gratings can be employed with simple demodulation schemes to yield inexpensive sensors.

Long-period gratings can also be employed as simple filters to demodulate the output of Bragg grating sensors[23]. In such a case, the reflection from a perturbed Bragg grating acts as a narrow band optical source and by properly controlling the location of the bands of the long-period and Bragg gratings, a highly sensitive demodulation system can be obtained[23]. The limitation of this system is the inherent susceptibility of the long-period gratings to external perturbations such as temperature[23].

5.2.2   Multiplexing

To reduce the cost of a sensing system it is important that a number of long-period gratings be multiplexed using the same optical source and detection scheme. In this subsection we outline a few methods to multiplex long-period grating sensors. The simplest method to multiplex long-period gratings is illustrated in Figure 5.8.
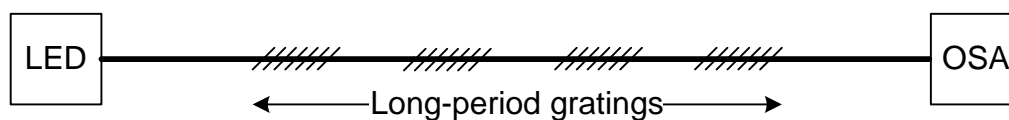
Figure 5.8: Multiplexing of spectrally offset long-period gratings using an LED and a optical spectrum analyser (OSA)

The long-period gratings are written on a single fibre with the physical separation determined by the intended application. The resonance bands of the gratings within the LED spectrum are offset to prevent cross-talk between sensors[23]. The spectral shifts in these wavelength-multiplexed sensors is detected by the OSA. Due to the large spectral width of these gratings only a limited number of sensors may be multiplexed using a single LED[23]. The problem can be overcome by combining the spectra of a number of LEDs with different centre wavelengths using multiplexers, or by employings gratings with longer lengths and hence smaller bandwidths.

Figure 5.9 shows a scheme to multiplex two long-period gratings located at distinct wavelengths, using fibre Bragg gratings and band-pass filters[23].

The Bragg gratings reflect a part of the corresponding long-period gratings spectrum in the return leg of the coupler (See Figure 5.7). Band-pass filters matched to the Bragg grating resonant wavelengths are used to detect the intensity change along with a pair of photo detectors[23]. The long-period and Bragg grating pairs can also be placed serially in the same output leg of the coupler and the scheme can be modified to multiplex more than two gratings[23].

The limitation of the system is that intensity changes due to fibre bends and source fluctuations can modify the sensor outputs and result in erroneous measurements. Furthermore, temperature variations that shift the Bragg grating and the fibre spectra can influence the output.
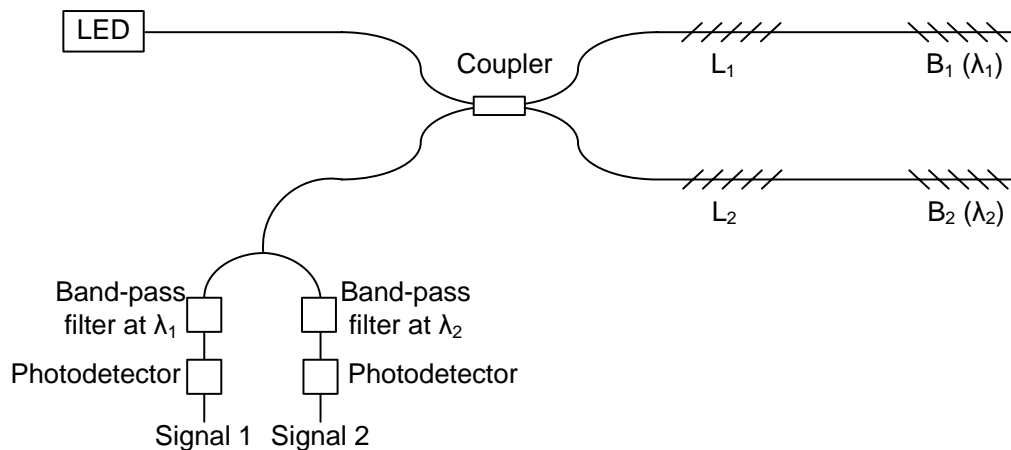
Figure 5.9: Multiplexing of two long-period gratings (denoted by L_1 and L_2) using a pair of Bragg gratings (B_1 and B_2). The centre wavelength of the two band-pass filters are matched to the resonant wavelengths of the Bragg gratings (λ_1 and λ_2).

Figure 5.10 depicts a method to time-division multiplex two long-period grating sensors. A laser diode that spectrally overlaps the resonance band of both the gratings is used as a source.
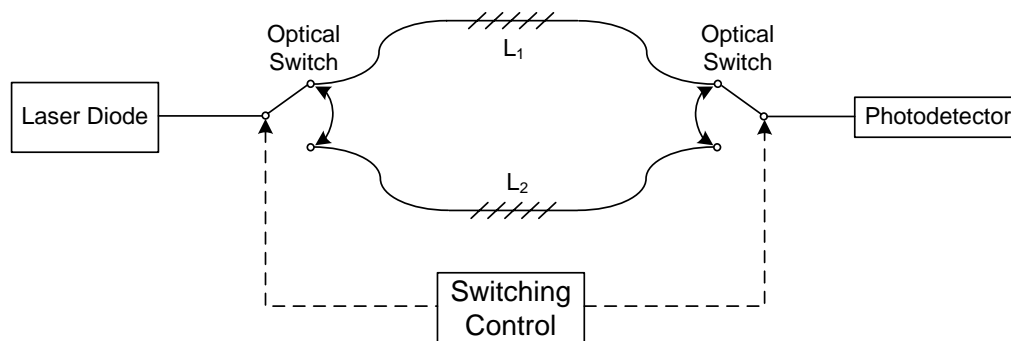
Figure 5.10: Time-division multiplexing of two long-period gratings (Denoted by L_1 and L_2) using a single laser diode and photodetector.

Two synchronised optical switches regulate the input and output signals between the two gratings. The system uses the demodulation scheme proposed in Section 5.2.1 and eliminates the requirement of optical band-pass filters[23]. The time division multiplexing can easily be extended to interrogate more than two gratings. The limitation is, once again, the sensitivity to fibre bends and intensity fluctuations of the source, and hence the sensing output has to be normalised to a reference signal that accounts for these effects.

In this section a few techniques for wavelength and time-division multiplexing of long-period grating sensors were proposed. The limitation imposed by the wide bandwidth of the bands may be overcome by fabricating gratings with longer lengths. The multiplexing

of gratings will enable reduction in cost per channel of the system. A number of gratings in the same or different fibres can be used for distributed sensing of the same perturbation or for simultaneous measurement of multiple parameters.

Chapter 6

Detection Mechanism and Constraints

6.1 Introduction

Section 1.3 deals with commercially available detection methods, as well as some other possible detection methodologies. This led to an investigation into possible SF_6 detection through refractive index sensing and possible methods of implementing refractive index sensing technologies within the high voltage environment in which SF_6 is utilised. Due the constraint of high electric and magnetic fields within substations a solution was sought that would be immune to these influences. It was found that long-period gratings utilised to detect ambient refractive index changes may suit the application and so further investigation was conducted.

A major constraint through the use of long-period gratings is the temperature sensitivity of the devices which cannot be distinguished from the refractive index sensing capabilities. This was discussed in Section 5.1.3 and is discussed further in Chapter 7 where the application specific data is applied to this constraint.

Obviously, to design a sensor of this type one is required to know the scale of magnitude change in refractive index when SF_6 mixes with air. This aspect is discussed at length in Section 6.2 which is followed with some preliminary results based on the analytical models.

6.2 Refractive Index of SF_6 − Air Mixtures

A dilute gases refractive index is related to its temperature, pressure and molar refractivity through the Lorentz-Lorenz formula, or the Clausius-Mossotti equation[35]:

$$n \approx \sqrt{1 + \frac{3AP}{RT}} \qquad (6.1)$$

Where: n is the refractive index of the gas
A is the molar refractivity of the gas
P is the pressure of the gas
R is the universal gas constant
T is the absolute temperature of the gas.

In [36], Equation 6.1 is re-written to include the gas density and so becomes:

$$\frac{n^2 - 1}{n^2 + 2} = A_R \rho + B_R(T) \rho^2 \tag{6.2}$$

Where: A_R is the first refractive virial coefficient
ρ is the gas density in moles per unit volume
$B_R(T)$ is the second virial coefficient.

Whereas A_R depends only on wavelength, $B_R(T)$ is a function of both wavelength and temperature[36] and both coefficients are determined experimentally.

The gas density is given by the virial equation of state[37]:

$$\frac{P V_m}{RT} = 1 + \frac{B}{V_m} + \frac{C}{V_m^2} + \frac{D}{V_m^3} + \dots \tag{6.3}$$

$$\text{with: } B = -V_c \tag{6.4}$$

$$\text{and } C = \frac{V_c^2}{3} \tag{6.5}$$

Where: V_m is the molar volume of gas, $V_m = \frac{V}{n}$
V_c is the critical molar volume
V is the volume of gas
n is the number of moles of gas
B & C are the first and second virial coefficients of state respectively.

The authors of [36] show that higher order terms can be neglected and, again including the gas density, Equation 6.3 can be simplified to yield:

$$\frac{P}{RT} = \rho + B_P(T) \rho^2 \tag{6.6}$$

Where: $B_P(T)$ is the second virial coefficient of state.

In [36] it is also shown that Equation 6.2 can be manipulated to yield:

$$n - 1 = A \left(\frac{P}{RT} \right) + B(T) \left(\frac{P}{RT} \right)^2 \tag{6.7}$$

Where: $n - 1$ is the refractivity of the gas.
A is related to A_R in Eqn. 6.2 through: $A_R = \frac{2}{3} A$.
$B(T)$ is related to $B_R(T)$ in Eqn. 6.2 and $B_P(T)$ in Eqn. 6.6 through Eqn. 6.8:

$$B_R(T) = \frac{2}{3} B(T) + \frac{2}{3} A B_P(T) - \frac{1}{9} A^2 \tag{6.8}$$

Now, in order to calculate a working range of expected refractive index shifts we begin with the ideal gas law:

$$PV = nRT \tag{6.9}$$

Where: V is the volume the gas occupies
             n is the number of moles constituting the gas.

Now if we assume that 1 m^3 is filled with SF_6 at 20 ° C (293 K), at atmospheric pressure (101,325 kPa), the conditions expected within a gas insulated substation, and recalling R = 8,3145 J.mol^{-1}.K^{-1}, from Equation 6.9 we can compute n as:

$$n \;=\; \frac{PV}{RT} \tag{6.10}$$
$$\;=\; 41,59 \text{ moles} \tag{6.11}$$

From the above result we can conclude that the maximum number of moles of SF_6 that can occupy in a 1 m^3 space without altering the temperature or pressure is 41,59 moles of gas. Also, as we are considering a volume of 1 m^3, we can also conclude that the maximum gas density is 41,59 moles.m^{-3} which is the gas density defined above as ρ.

Now as $\rho = \frac{n}{V}$, from above, and $\frac{P}{RT} = \frac{n}{V}$, $\frac{n}{V}$ may be substituted into Equation 6.7 to obtain:

$$n - 1 = A\left(\frac{n}{V}\right) + B(T)\left(\frac{n}{V}\right)^2 \tag{6.12}$$

Finally utilising experimental data, contained in [36], for A and $B(T)$ at 1300 nm, in Equation 6.12, one calculates:

$$
\begin{aligned}
n - 1 &= (1,676 \times 10^{-05})(41,59) + (52 \times 10^{-10})(41,59)^2 \\
n - 1 &= 706,043 \times 10^{-06} \\
\therefore n &= 1,000706
\end{aligned}
\tag{6.13}
$$

This value is clearly the maximum refractive index that can be achieved from pure SF_6 assuming no diffusion and no mixture with air so practically it is not achievable. This does, however, give a range of refractive index changes that theoretically can be expected and is repeated here for clarity:

$$1 \leq n \leq 1,000706 \tag{6.14}$$

In order to obtain an estimate for the resolution required by a sensor in order to detect a change in refractive index MATLAB was used to plot the concentration versus refractive index over the range between 0 and 1%. This is shown in Figure 6.1.

From the graph, one can see that for a concentration of 1% SF_6 in air the resulting refractivity is:

$$n - 1 = 1,677 \times 10^{-05} \tag{6.15}$$

Equation 6.15 also defines a resolution required for the sensor in order to be able to detect a concentration of 1%.
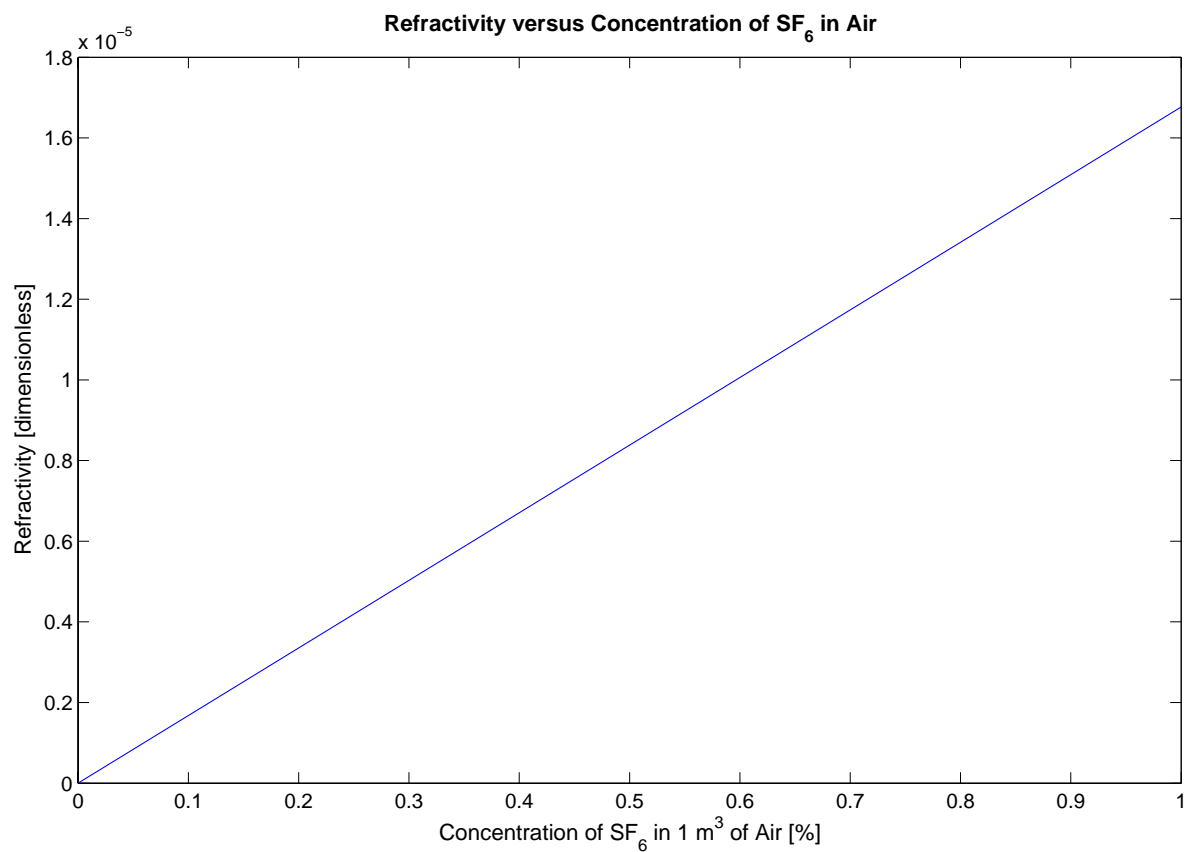
Figure 6.1: The linear relationship of varying concentrations of SF_6 in Air versus the resulting refractivity.

Chapter 7

Design Specifications

7.1 Introduction

Up until this point the fundamentals and properties of long-period gratings have been discussed. Further discussion into the analytical modelling of long-period gratings was then entered into and the principles behind long-period grating sensors was presented together with multiplexing and demodulation schemes. An analysis was conducted into the refractive index change caused by SF_6 mixing with air and so finally the culmination of the previous chapters is a possible design to implement an SF_6 detector based on principles discussed in previous chapters.

This chapter discusses a design based on fundamental principles of long-period gratings together with the constraints on the system. To begin with we must summarise the previous chapters before outlining possible design strategies:

1. Long-period gratings consist of a modulated modification of the refractive index of a section of the core of an optical fibre.

2. A long-period grating is sensitive to strain, temperature and ambient refractive index changes where the sensitivity depends on both the physical nature of the fibre and the periodicity and modulation depth of the core refractive index modulation.

3. SF_6-air mixtures were shown to have a very small modification to the ambient refractive index of air and so a highly sensitive gratings would be required.

To understand the sensitivity required by the system a simulations were performed using OptiGrating commercial software and self-written MATLAB programs to evaluate wavelength shifts under ambient refractive index changes. As expected from analyses performed in previous chapters, higher order modes undergo relatively higher wavelength shifts when compared to lower order modes. Figure 7.1 shows the shifts undergone by the 5th, 6th and 7th order modes through a change in ambient refractive index from 1,0 to 1,1.

Simulation studies utilising OptiGrating Commercial Software revealed very small wavelength shifts for small refractive index changes, as expected. The higher order modes
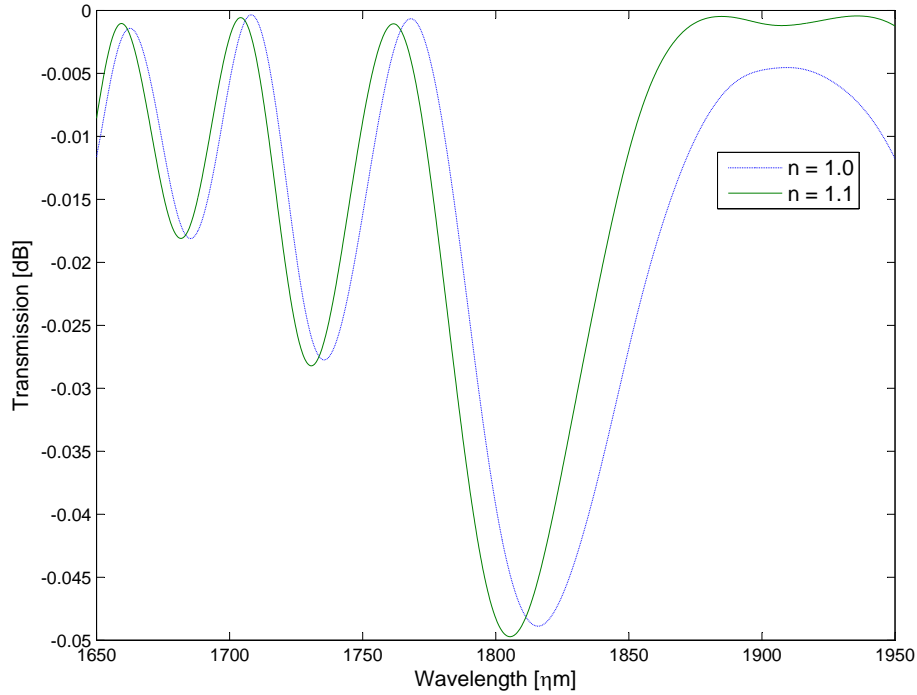
Figure 7.1: Transmission spectrum of a $\Lambda = 320$ μm grating between 1650 and 1950 nm. A wavelength shift of 11 nm from 1816 to 1805 nm can be observed in the 7th order mode.

undergo relatively more shift than lower order modes and so investigation into higher order mode wavelength shifts was undertaken. Also investigated was the use of relatively long gratings with apodisations and chirp with specific grating shapes which have been shown to increase sensitivity to external ambient refractive index sensing[38, 39, 40, 41].

7.1.1   Average Index Modulation

The average index modulation is defined as the average index change along the grating length, L[39]. Two grating shapes are regularly used to define gratings: uniform and linear average index modulations. A uniform average index modulation is defined by[39]:

$$\Delta n_0 = \Delta \qquad \Delta << n_0 \tag{7.1}$$

Where: Δ is is the total index change along the grating
          n_0 is the waveguide refractive index.

A linear average index modulation is defined by[39]:

$$\Delta n_0(z) = -\frac{z - \frac{L}{2}}{L}\Delta \qquad \Delta << n_0 \tag{7.2}$$

Where: z is a variable used to describe any point along the length, L, of the grating.

7.1.2   Grating Period Chirp

Grating period chirp defines a distance-dependent grating period modulation[38]. Various grating period chirps are possible and these are listed below:

No Chirp (Constant Period):

$$\Lambda(z) = \Lambda_0 \tag{7.3}$$

Linear:

$$\Lambda(z) = \Lambda_0 - \frac{z - \frac{L}{2}}{L}\Delta \qquad \Delta << n_0 \tag{7.4}$$

Quadratic:

$$\Lambda(z) = \Lambda_0 - \left[\left(\frac{z}{L}\right)^2 - \frac{1}{4}\right]\Delta \qquad \Delta << n_0 \tag{7.5}$$

Square Root:

$$\Lambda(z) = \Lambda_0 - \left[\sqrt{\frac{z}{L}} - \frac{1}{\sqrt{2}}\right]\Delta \qquad \Delta << n_0 \tag{7.6}$$

Cubic Root:

$$\Lambda(z) = \Lambda_0 - \left[\sqrt[3]{\frac{z}{L}} - \frac{1}{\sqrt[3]{2}}\right]\Delta \qquad \Delta << n_0 \tag{7.7}$$

7.1.3   Grating Apodisation

The grating apodisation is the slowly varying envelope of the grating profile[40]. Various grating apodisations are possible and these are listed below:

Uniform (no apodisation)

$$A(z) = 1 \tag{7.8}$$

Gaussian Apodisation

$$A(z) = exp\left\{-ln2\left[\frac{2(z - L/2)}{sL}\right]^2\right\} \tag{7.9}$$

Where: $A(z)$ is the slowly varying envelope of the grating profile
  s is the taper parameter
  L is the grating length.

The apodisation taper parameter, s, defines the rate at which the extremities of the apodisation profile taper[40].

Hyperbolic Tangent

$$A(z) = \tanh\left(\frac{sz}{L}\right)\tanh\left[s\left(\frac{1-z}{L}\right)\right] + 1 - \tanh^2\left(\frac{s}{2}\right) \qquad (7.10)$$

7.1.4   Grating Shape

The grating shape is the profile of index modulation within one grating period Λ[40]. Two grating shapes are regularly used to define gratings: rectangular and sine grating shapes. A rectangular grating is defined by:

$$f(z) = \left(\begin{array}{ll} +1 & 0 < z < \frac{\Lambda}{2} \\ -1 & \text{elsewhere} \end{array}\right) \qquad (7.11)$$

A sine grating shape is defined by[40]:

$$f(z) = sin\left(\frac{2\pi}{\Lambda}z\right) \qquad (7.12)$$

A simulation study was conducted using various combinations of length, taper parameter, grating periodicity, grating shape, different induced indices, various uniform average index modulations and different grating period chirps. The results of this study is detailed in Section 7.2.

7.2   Simulation Results

Many different combinations of the parameters mentioned in Sections 7.1.1 to 7.1.4 were simulated with varying ambient refractive indices. One will recall from Section 6.2 that the sensor was required to detect a refractive index shift of $n = 1$ to $n = 1,00001677$. The combination of grating parameters which provided the best sensing results was a grating with a sine grating shape, $L = 40000$ μm or 40 mm, a Gaussian apodisation with a taper parameter of 1, $\Lambda = 320$ μm, average linear induced index modulation of 0,0002 and no grating chirp.

Figure 7.2 shows the transmission spectrum of the above mentioned grating for external refractive indices of $n = 1$ and $n = 1,42$. The sixth order mode shows a shift of 12 nm, however, as mentioned above, the intended sensing range of the Sulphur Hexafluoride detector is calculated to be between $n = 1$ and $n = 1,00001677$. Simulation results indicate that the seventh order mode ($\lambda = 3129,8$ nm) undergoes a wavelength shift in the region of 350 pm. This mode is not displayed on the graph as the wavelength is not within fibre transmission spectra and so is not feasible to be used for sensing.

The shift of the seventh order mode, although a shift, is very small and would be almost undetectable in practical environments. The shift is also equivalent to a 3,76 °C temperature change in a temperature insensitive grating which this grating is not as it functions in the normal region. Temperature insensitive gratings were simulated but were found to
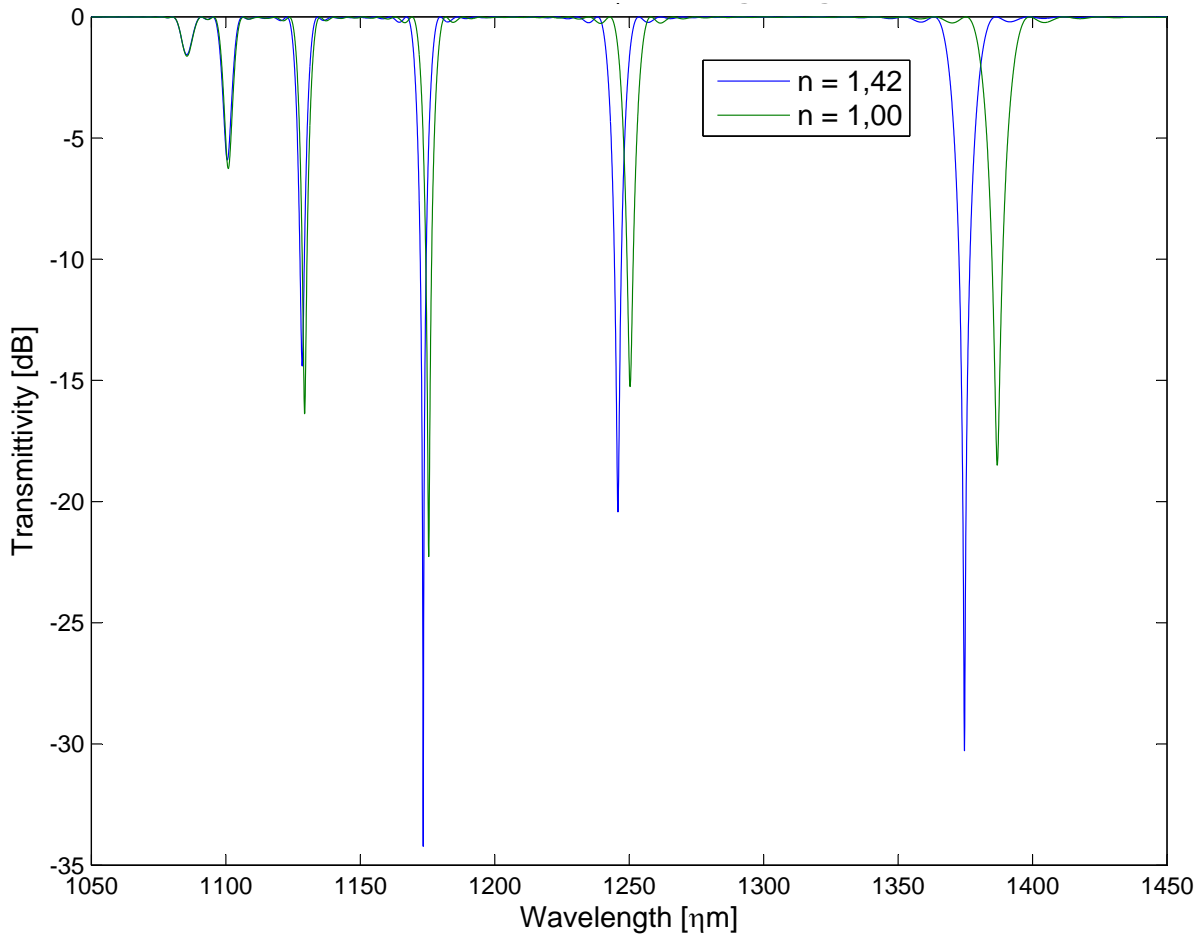
Figure 7.2: The transmission spectrum of the proposed long-period grating ($\Lambda = 320$ μm) for external refractive indices of $n = 1$ and $n = 1,42$. A wavelength shift of 12 nm is experienced by the sixth order cladding mode.

be insensitive to the very small ambient refractive index changes.

Two problems also exist with sensing at $\lambda = 3129, 8$ nm the first is the transmission losses of fibre in the wavelength region and the second is that we know, from Section 3.2.1, that the mode confinement within the core decreases as the wavelength is increased. This means that the utilisation of the coupling to the seventh order mode will thus cause great losses and affect the practical sensing capability of the device.

7.3   Experimental Results

No specific experimentation was entered into regarding the manufacture and testing of long-period grating sensors due to the above mentioned practical constraints. Many authors have presented experimental results show that minimal detectable refractive index changes are $4,49 \times 10^{-4}$, $1,77 \times 10^{-4}$, $1,86 \times 10^{-5}$ in the range $1,33 - 1,398$; $1,398 - 1,426$ and $1,426 - 1,444$ respectively, with all indices specified at a wavelength of 1500

nm[22, 23, 29]. The increased resolution of the sensor in the range of the effective index of the cladding modes was discussed above and as this intended application is far from the refractive index of the cladding the resolution is not expected to be high enough to detect SF_6.

Chapter 8

Conclusions

In this chapter we present an overview of the study on long-period gratings and their intended use for detection of SF_6 in GIS and GIL installations. Also presented is future research areas and topics to possibly enable the implementation of a real-time detection system for SF_6 systems.

One may recall from the introduction that the objective of the research report was two fold:

1. To provide the reader with an in-depth analysis of the properties of photo induced long-period gratings and their applications as fibre optic sensors.

2. To provide an analysis and design of a fibre optic sensor system to detect SF_6 leaking from GIS or GIL installations.

8.1   Summary

Chapter 1 provided the reader with a basic understanding of fibre technology, an introduction to the uses and advantages of SF_6 and a review of SF_6 detections methods together with their advantages and disadvantages. It was observed that current detection technologies suffer from high cost and so are not implemented in permanent sensing capacity but rather in a maintenance capacity. This provided the basis for the need for an implementation of existing technology in a new application to solve a real problem and hence clarified the goals of the research.

Chapter 2 introduces the reader to a throrough definition of a long-period grating: an ultraviolet (UV) induced periodic index modulation of the refractive index of the core of a single mode fibre[20]. LPGs couple light from the core into the fibre cladding at discrete wavelengths producing one or more attenuation bands in the fibre transmission[19]. Typically modulation depths are of the order of 10^{-4} m, with periods between 100 - 500 μm and lengths of 2,5 cm are common[19].

This definition leads into the discussion of guided, radiation and cladding modes, the principle of operation and concludes with a discussion of the sensitivity of long-period gratings. With the basic operating principles and sensitivity discussed, the reader is led

into the principles behind SF_6 detection and the constraints in Chapter 6.

Chapter 3 reviewed the phenomena of photosensitivity and mode coupling in optical fibres. The periodicity of the refractive index modulation characterises the spectral properties of the device through the phase-matching condition. Coupled mode theory was employed to investigate the coupling between co and counter-propagating modes in a perturbed system.

Once the basic understanding of the concepts of mode coupling and photosensitivity had been developed, it was extended to the investigation of the fundamental characteristics of long-period gratings. We presented an anlaytical model to explain the spectral modulation offered by these devices. It was shown that the multiple loss bands in a grating result from coupling to discrete forward-propagating cladding modes. Characteristic curves that predict resonance wavelength for different grating periods were discussed.

It was demonstrated that the location of the bands are strong functions of the properties of the host fibre, the grating period and the writing and annealing conditions. The notation of normal and anomalous regions were introduced to differentiate the operation at wavelengths with positive and negative slopes of the characteristic curves, respectively. The spectral width of the resonance bands was found to depend on the grating length and the peak index change induced during the fabrication process[22].

Chapter 4 reviewed three different methods of fabricating long-period gratings in hydrogen-loaded germanosilicate fibres. These included a method utilising a low power CO_2 laser to induce periodic index changes in the fibre core. Also discussed was the importance of correct high temperature annealing of the gratings and improvement in sensitivity gained through chemical etching of the fibre cladding.

Chapter 5 discussed long-period gratings as index of refraction sensors[29]. An analytical model was presented and it was shown the the sensitivity is a complex function of many different parameters such as grating period, the order of the cladding mode and the writing and annealing conditions. The large temperature sensitivity of long-period gratings is a limitation during their implementation as a index of refraction measurement device. It was shown that this drawback can be overcome by fabricating gratings in fibres with special refractive index profiles.

Long-period gratings were demonstrated as highly sensitive index of refraction sensors. It was shown that for a given fibre, the spectral shift due to index changes in the medium surrounding the bare cladding is a strong function of the grating period and the order of the resonance band[23]. Although these sensors can be implemented without violating the integrity of the fibre, it was shown that their sensitivity may be tuned by selectively etching the cladding diameter.

Chapter 6 discusses refractive index sensing and influences of the refractive index. An in-depth analysis is then given of the anticipated alteration of the refractive index of air once mixed with low concentrations of SF_6. One specific limitation of the system, tem-

perature variations, is briefly discussed here, but covered in more detail in later sections.

It was shown that long-period grating sensors can be implemented with simple demodulation schemes[29]. Techniques to wavelength and time-division multiplex these devices were also proposed and discussed in Chapter 5.

We hence conclude that long-period gratings are versatile devices that can be employed for a multitude of sensing applications however the intended use a detection system for the presence of SF_6 is possible but not practical. The small alteration in the ambient refractive index of air when combined with small concentrations of SF_6 is barely detectable with the use of specific long-period gratings. The cause of the alteration of the refractive index of the ambient cannot be conclusively linked to SF_6 detection as the change could plausibly be caused through an alteration in the atmospheric pressure or a temperature alteration.

For example authors have demonstrated the use of long-period grating sensors to detect various solutions of analytes such as butane/propane, sucrose solutions and others but in these case the only influence on the refractive index, besides temperature, is the solution concentration itself. In the case of detecting SF_6 many different external factors can influence the refractive index of the air surround GIS or GIL installations and the exact cause of a change detected by a long-period grating sensor may not be SF_6 and incorrectly trigger alarms.

The investigation and research report has provided a thorough background to optical sensing technologies, the associated analysis of long-period gratings and provides sufficient basis for a reader to understand and construct a long-period grating refractive index sensor for other applications where the refractive index changes can be conclusively linked to a specific measurand.

Appendix A

Breakdown in Sulphur Hexafluoride

A.1 Introduction

This appendix attempts to explain the breakdown science in SF_6 as compared to air. First described is the streamer breakdown and this is further extended to avalanche-to-streamer conversion and a comparison between the occurrences in air and SF_6.

A.2 Streamer Breakdown

Free electrons exist due to cosmic radiation and other factors. The force on an electron in an electric field is given by the product of the electron charge (q_e) and the electric field (ε), therefore:

$$F = q_e \varepsilon \tag{A.1}$$

For each free electron generated, they accelerate, collide with molecules and produce more electrons. These then accelerate, collide and form more electrons and the process continues which results in an electron "avalanche". The positive ions that are formed when an electron is emitted following a collision move toward the cathode(Negative electrode) but the velocity of these ions is much slower than the velocity of the electrons. The positive ion velocity is approximately $1 \times 10^3 m.s^{-1}$ whereas the velocity of the electrons is approximately $1 \times 10^5 m.s^{-1}$.

As this "group" of negative charge moves towards the anode(Positive electrode) it expands(As likes charges repel) and produces a local electric field given by the formula for a spherical electrical field:

$$\varepsilon = \frac{Q}{4\pi\epsilon r^2} \tag{A.2}$$

Where r is the distance from the centre of the "group" to the outside. This local field is referred to as a space charge field. The group then attracts more positive ions and cause more detachment of electrons. This process continues and when the energy within the space charge field reaches a critical level and the process becomes self-propagating, the avalanche forms a plasma of charge (Effectively a conducting path of negligible resistance)

and a streamer results. A streamer can be defined as a breakdown caused by a single electron avalanche[42].

To limit the possibility of streamer breakdown occurring electro-negative gases are employed. These gases have the property to form negative ions upon collision with an electron. Electro-negativity implies an affinity for electrons OR the ability of the gas to attract and "capture" electrons.

To describe the process mathematically some definitions need to be given:

α Townsend's first co-efficient of ionisation, simply referred to as the ionisation co-efficient. Defined as the number of ionising collisions for an electron per unit length of path in the direction of the field. Simply described as: if an electron moves a distance x there will be αx new electrons.

η The attachment co-efficient. Simply defined as: if an electron moves a distance x there will be ηx new negative ions.

n_e The number of free electrons in the gas.

From the above definitions and applying initial conditions one can obtain an expression showing the growth of the number of free electrons in an avalanche:

$$n_e = n_0 e^{(\alpha - \eta)x} \tag{A.3}$$

This leads to the following conclusions:
IF $\alpha > \eta \Rightarrow$ Instability $\Rightarrow$ Breakdown.
IF $\alpha < \eta \Rightarrow$ Avalanche vanishes $\Rightarrow$ NO Breakdown.
IF $\alpha = \eta \Rightarrow$ Threshold of Breakdown.

α and η both depend on the applied field because the field effects the acceleration of the electrons, the energy of the collisions and so ultimately the "production" of electrons. This means if Equation A.3 is applied to a uniform field then α & η can be assumed to be constants. If Equation A.3 is applied to a non-uniform field then α & η are functions of the field and as the field depends on distance, α & η will be functions of distance ie:

$$\alpha, \eta = f(\varepsilon) = f(x) \Rightarrow \alpha, \eta = f(x) \tag{A.4}$$

This implies that an integral needs to be preformed in order to calculate $(\alpha - \eta)$ and so in a non-uniform field we can write:

$$(\alpha - \eta) = \int_0^X (\alpha - \eta) dx \tag{A.5}$$

A.2.1   Development of avalanches into streamers

Streamer breakdown is the result of avalanche activity reaching a critical magnitude. Raether [7] proposed this critical level to be when:

$$\int_0^X \alpha \, dx = 20 \tag{A.6}$$

This equation can be interpreted to mean that if n_e in Equation A.3 is equal to $e^{20} \approx 1 \times 10^8$ then it is very likely breakdown will occur. In plain English: If you start with 1 electron and if it collides with molecules and produces 180 million(Approx.) electrons then it is very likely breakdown will occur.

An avalanche develops into a streamer because the space charge field from the electrons and ions in the head of the avalanche may cause an instability in the development of the avalanche resulting in the formation of fast moving anode and cathode directed streamers from the avalanche head.

These streamers form a highly conducting plasma channel across the gap and the voltage breaks down. Raether's criterion did not account for re-attachment of electrons and also only considered primary ionisation processes (Electron Collision) and did not consider secondary ionisation processes such as photoionisation. With increased understanding of electron processes the role of attachment became apparent and the criterion was modified to:

$$\int_0^X (\alpha - \eta) dx = 18 \tag{A.7}$$

This criterion still focuses on ionisation by collision as the significant process in avalanche growth. Simultaneous with Raether's work, Meek [8] identified the Streamer mechanism and formulated the following breakdown criterion:

$$\alpha_X e^{\int_0^X \alpha dx} = K E_X \left(\frac{x}{\rho}\right)^{\frac{1}{2}} \tag{A.8}$$

The basis for the this breakdown criterion was that Meek made the plausible assumption that cathode and anode directed streamers would develop when the radial space charge field from the avalanche head becomes of the same order of magnitude as the externally applied field.

Examining this criterion, shows that the exponent $\int_0^X \alpha dx = k$ is approximately constant, this reduces to Raether's criterion with $k = 20$.

Pedersen [42, 43] explored the role played by secondary processes, the most important of which is photo ionisation. This work draws on Townsend's early work which proposed the Townsend or Generation Mechanism, given by:

$$i = i_\circ \frac{e^{\alpha d}}{1 - \gamma \left(e^{\alpha d} - 1\right)} \tag{A.9}$$

Where:

$i \Rightarrow$ Current through the gap.

$i_0 \Rightarrow$ Initial current due solely to external ionising sources such as photoionisation.

$d \Rightarrow$ The gap length.

$\alpha \Rightarrow$ The number of ionising collisions for an electron per unit length of path in the direction of the field and is called Townsend's first ionisation co-efficient.

$\gamma \Rightarrow$ Townsend's second ionisation co-efficient which represents all the possible secondary processes of ionisation.

But because $e^{\alpha d} >> 1 \Rightarrow e^{\alpha d} - 1 \approx e^{\alpha d}$ therefore:

$$i = i_0 \frac{e^{\alpha d}}{1 - \gamma e^{\alpha d}} \tag{A.10}$$

and as $\gamma e^{\alpha d} \to 1, i \to \infty$ which defines the sparking threshold:

$$\gamma e^{\alpha d} = 1 \tag{A.11}$$

Pedersen proposes that the Townsend and Streamer processes merge into a single criterion:

$$\alpha_X e^{\int_0^X \alpha dx} = G\{X, \rho, E_X, \mu, \%H_2O......\} \tag{A.12}$$

Experience has shown that X and ρ are the dominant influences therefore:

$$\alpha_X e^{\int_0^X \alpha dx} = G\{X, \rho\} \tag{A.13}$$

It may seem that secondary effects have been ignored, but α is a surrogate for the production of electrons and hence secondary process associated with electrons at the stage that the avalanche reaches its critical length. For a given air density or pressure this criterion reduces to:

$$ln(\alpha_X) + \int_0^X \alpha dx = g(X) \tag{A.14}$$

Where (α_x) is the numerical value of α at the avalanche head. Pedersen argues that for uniform fields X is equal to the gap length and α is constant. This means that numerical values of the function $g(X)$ can be found by calculating the left-hand side of Equation A.2.1 from uniform field breakdown data. This the gives a breakdown criterion to which non-uniform predictions can be compared to.

In a sequel, Pedersen [44] extends the criterion to electronegative gases:

$$\frac{1}{2}ln(\alpha_X) + \int_0^X (\alpha - \eta)dx = g(X) \tag{A.15}$$

For highly electronegative gases like SF_6 this reduces to:

$$\int_0^X (\alpha - \eta)dx = k = 18 \tag{A.16}$$

A.2.2   Breakdown in SF$_6$

Pedersen in [44] gave expression for α/p and η/p for SF$_6$ as:

$$\frac{\alpha}{p} = 0.024\frac{E}{p} - 1,76 \tag{A.17}$$

$$\frac{\eta}{p} = -0.004\frac{E}{p} + 1,52 \tag{A.18}$$

$$\tag{A.19}$$

Where:

$\frac{\alpha}{p}$ and $\frac{\eta}{p}$ were measured in $.cm^{-1}.mmHg^{-1}$

$\frac{E}{p}$ was measured in $V.cm^{-1}.mmHg^{-1}$

By recalling the following conversions:

$$mmHg = Torr.$$
$$Torr \rightarrow Bar \div 760.$$
$$Torr^{-1} \rightarrow Bar^{-1} \times 760.$$
$$cm^{-1} \rightarrow m^{-1} \times 100.$$

The expressions can be re-written as [45]:

$$\frac{\alpha}{p} = 0.024\frac{E}{p} - 133.8 \times 10^3 \tag{A.20}$$

$$\frac{\eta}{p} = -0.004\frac{E}{p} + 115 \times 10^3 \tag{A.21}$$

$$\tag{A.22}$$

Where:

$\frac{\alpha}{p}$ and $\frac{\eta}{p}$ are measured in $.m^{-1}.Bar^{-1}$

$\frac{E}{p}$ was measured in $V.m^{-1}.Bar^{-1}$

Also:

$$\frac{\alpha - \eta}{p} = 0.028\frac{E}{p} - 249,3 \times 10^3 \tag{A.23}$$

$$\alpha - \eta = 0.028E - 249 \times 10^3 p \tag{A.24}$$

Figures A.1 and A.2 display air $\frac{\alpha}{p}$ versus $\frac{E}{p}$ and $\frac{\eta}{p}$ versus $\frac{E}{p}$ curves, and SF$_6$ $\frac{\alpha}{p}$ versus $\frac{E}{p}$ and $\frac{\eta}{p}$ versus $\frac{E}{p}$ curves.

The gradients of both $\frac{\alpha}{p}$ versus $\frac{E}{p}$ and $\frac{\eta}{p}$ versus $\frac{E}{p}$ are observed to be steep; $\frac{\alpha}{p}$ versus $\frac{E}{p}$ with a positive gradient and $\frac{\eta}{p}$ versus $\frac{E}{p}$ with a negative gradient. This means once the intercept of $\frac{\alpha}{p} = \frac{\eta}{p}$ has been achieved, the difference $\alpha - \eta$ rises rapidly which equates to
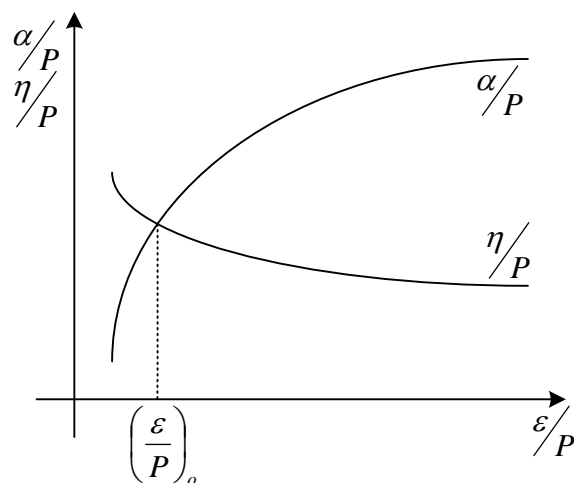
Figure A.1: A rough graph of $\frac{\alpha}{p}$ versus $\frac{E}{p}$ and $\frac{\eta}{p}$ versus $\frac{E}{p}$ for air.
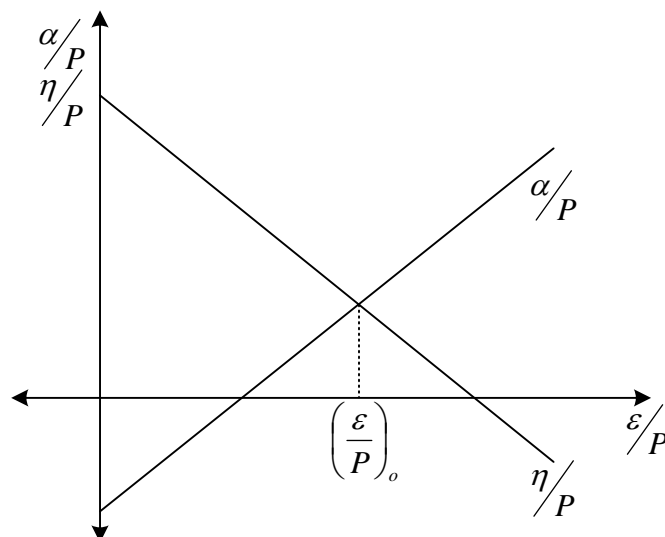
Figure A.2: A rough graph of $\frac{\alpha}{p}$ versus $\frac{E}{p}$ and $\frac{\eta}{p}$ versus $\frac{E}{p}$ for SF_6.

a rapid growth of the avalanche across the gap. It also leads to a rapid development of local space charge which is a major contributing factor to the conversion of an avalanche into a streamer. Once the avalanche converts into a streamer the process becomes self-propagating and the gap breaks down.

In SF_6, in particular, the point where $\frac{\alpha}{p} = \frac{\eta}{p}$ is very close to the cathode and so all the "action" takes place close to the inner conductor of a co-axial conductor system, the most common system where SF_6 is employed. Due to this fact any surface protrusion on the inner conductor can greatly affect the breakdown strength of the system and Pedersen in [46] investigates how one can predict breakdown strengths of systems where surface roughness is known.

For SF_6 $\alpha = \eta$ at $\left(\frac{E}{P}\right)_0$. For SF_6 $\left(\frac{E}{P}\right)_0 = 8,9 \times 10^6$ V.m^{-1}Bar^{-1}. The same principle applies for air where $\left(\frac{E}{P}\right)_0 = 2,39 \times 10^6$ V.m^{-1}Bar^{-1}. This implies at equal pressures SF_6 is approximately 3,5 times more insulating than air.

A.2.3   Streamer breakdown in gas mixtures

Baumgartner, in [40], sets out the streamer mechanism. Baumgartner's premise is the each gas contributes to the α and η in proportion to its partial pressure. For example if we mix SF_6 and N_2, such that the partial pressure of SF_6 is pS and the partial pressure of N_2 is pN:

$$(\alpha - \eta)_{\mathrm{mix}} = 0,028 \times pS \left(E - 8,89 \times 10^6 \times p\right) + 5,32 \times 10^5 \times p \times pN \exp^{\frac{-2,08 \times 10^7 \times p}{E}} \quad \text{(A.25)}$$

$$pN = \frac{\text{Pressure of N}_2}{(\text{Pressure of N}_2) + (\text{Pressure of SF}_6)} \quad \text{(A.26)}$$

$$pS = \frac{\text{Pressure of SF}_6}{(\text{Pressure of N}_2) + (\text{Pressure of SF}_6)} \quad \text{(A.27)}$$

Where: p is the total pressure in bar
pS is the partial pressure of SF_6
pN is the partial pressure of N_2
E is the electric field in V/m
α is the ionisation coefficient in ionisations/m
η is the attachment coefficient in attachments/m

Comment should be made that, in Baumgartner's work, the measurements are generally higher than the predictions. This suggests that there is synergy present in that the performance of the mixtures is not simply the sum of the contributions of each gas, but enhancing factors are present.

Minli's work, in [47, 48], on tailoring a gas mixtures shows the role of N_2 in retarding free electrons and enhancing capture by SF_6 molecules is significant. The differences between impulse and ac performance must also be noted.

Bibliography

[1] R. G. Baumgartner. "Dielectric characteristics of mixtures of Sulfurhexafluoride (SF_6) and Nitrogen (N_2)." *IEE conference publication No 115*, pp. 366 – 369, September 1974.

[2] M. Zhou and J. Reynders. "Synergy between SF_6 and other gases to enhance dielectric strength." *Proceedings of the 7th International Symposium of High Voltage*, vol. 7, August 1997.

[3] J. A. Ruiz, E. Melero-García, A. Kivimäki, M. Coreno, P. Erman, E. Rachlew, and R. Richter. "Synchrotron radiation induced fluorescence spectroscopy of SF_6." *Journal of Physics B: Atomic, Molecular and Optical Physics*, vol. 38, pp. 387 – 398, February 2005.

[4] A. H. Werbeagentur. "Sulphur Hexafluoride." Tech. rep., Solvay, Fluor and Derivate, 2001.

[5] ABB. "Questions and Answers about SF6." Online, January 2000. URL `http://www.abb.com/sf6`. Last accessed 8 January 2006.

[6] European Fluorocarbons Technical Committee. "Fluorocarbons and Sulphur hexafluoride." Online. URL `http://www.fluorocarbons.org/en/families/sf6.html`. Last accessed 3 January 2006.

[7] H. Raether. *Electron Avalanches and Breakdown in Gases*. Butterworths, 1964.

[8] J. M. Meek and J. D. Craggs. *Electrical Breakdown of Gases*. Clarendon Press, 1953.

[9] J. Kuffel, E. Kuffel, and W. Zaengl. *High Voltage Engineering: Fundamentals*. Butterworth-Heinemann, 2nd ed., 2003. pp. 368.

[10] I. P. on Climate Change ('IPCC'). "IPCC list of greenhouse gases." Online, 1998. URL `http://en.wikipedia.org/wiki/IPCC_list_of_greenhouse_gases`. Last accessed 3 January 2006.

[11] H. Human. "SF_6 Remote Detection." Tech. Rep. NLC-LTE14-REP-001, National Laser Centre, May 2003.

[12] D. H. Stone, J. Gonglewski, M. Fox, S. Czyzak, J. Dowling, D. Senft, and E. Herman. "Remote sensing measurements using a CO_2 laser." *Proceedings of the SPIE - Industrial Applications of Laser Radar*, vol. 2271, pp. 29 – 44, July 1994.

[13] P. Varanasi and A. Gopalan. "Infrared spectroscopic measurements relevant to atmospheric remote sensing." *Proceedings of the SPIE - Optical Methods in Atmospheric Chemistry*, vol. 1715, pp. 476 – 487, June 1993.

[14] National Institute of Standards and Technology. "Chemistry WebBook." Online. URL `http://webbook.nist.gov/chemistry`. Last accessed 1 July 2007.

[15] E. R. Schildkraut and R. F. Connors. "Standoff Wide Area Detection of SF_6 by Means of a Passive IR Imaging Spectrometer." Online, November 2000. URL `http://www.blockeng.com/sf6paper.htm`.

[16] B. Optics. "OPAG 22." Online. URL `http://www.brukeroptics.com/ftir/opag.html`. Last accessed 5 January 2006.

[17] G. Pickrell, W. Peng, and A. Wang. "Random-hole optical fiber evanescent-wave gas sensing." *Optics Letters*, vol. 29, no. 13, pp. 1476 – 1478, July 2004.

[18] R. Cregan, B. Mangan, J. Knight, T. Birks, P. Russell, P. Roberts, and D. Allan. "Single-mode photonic bandgap guidance of light in air." *Science*, vol. 285, pp. 1537 – 1539, 1999.

[19] H. J. Patrick, A. D. Kersey, and F. Bucholtz. "Analysis of the Response of Long Period Fiber gratings to external index of refraction." *Journal of Lightwave Technology*, vol. 16, no. 9, pp. 1606 – 1612, September 1998. Pdf Link.

[20] P. Lalanne, I. D. Villar, I. R. Matías, and F. J. Arregui. "Optimization of sensitivity in Long Period Fiber Gratings with overlay deposition." *Optics Express*, vol. 13, no. 1, pp. 56 – 69, January 2005.

[21] G. Keiser. *Optical Fiber Communications*. McGraw-Hill, third edition ed., 2000.

[22] A. M. Vengsarkar, P. J. Lemaire, J. Judkins, V. Bhatia, T. Erdogan, and J. E. Sipe. "Long-period fiber gratings as band-rejection filters." *Journal of Lightwave Technology*, vol. 14, no. 1, pp. 58 – 65, January 1996.

[23] V. Bhatia. *Properties and Sensing applications of Long-Period Gratings*. Ph.D. thesis, Virginia Polytechnic, November 1996.

[24] J.-N. Pang, S. Y. Kim, S.-W. Kim, and M.-S. Kim. "Temperature insensitive long-period fibre gratings." *Electronics Letters*, vol. 35, no. 24, pp. 2134 – 2136, November 1999.

[25] J. W. Fleming. "Material dispersion in lightguide glasses." *Electronics Letters*, vol. 14, no. 326, 1978.

[26] Corning Incorporated. *Corning product information sheet, SMF-28 CPC6 Single-Mode Optical Fiber*. New York, 1996.

[27] Corning Incorporated. *Corning product information sheet, Flexcor Specialized Single-Mode Optical Fiber*. New York, 1996.

[28] W. W. M. G. Meltz and W. H. Glenn. "Formation of Bragg gratings in optical fibers by transverse holgraphic method." *Optics Letters*, vol. 14, p. 823, 1989.

[29] V. Bhatia and A. M. Vengsarkar. "Optical fiber long-period grating sensors." *Optics Letters*, vol. 21, pp. 692 – 694, May 1996.

[30] K. Chiang, Y. Liu, M. Ng, and X. Dong. "Analysis of etched long-period fibre grating and its response to external refractive index." *Electronics Letters*, vol. 36, no. 11, pp. 966 – 967, May 2000.

[31] T. H. W. Johnstone, G. Stewart and B. Culshaw. "Surface plasmon polaritons in thin metal films and their role in fiber optic polarizing devices." *IEEE Journal of Lightwave Technology*, vol. 8, pp. 538 – 543, 1990.

[32] X. Shu, L. Zhang, and I. Bennion. "Sensitivity Characteristics of Long-Period Fiber Gratings." *Journal of Lightwave Technology*, vol. 20, no. 2, pp. 255 – 266, February 2002.

[33] S. W. James and R. P. Tatam. "Optical fibre long-period grating sensors: characteristics and application." *Measurement Science & Technology*, vol. 14, pp. R49 – R61, 2003.

[34] V. Bhatia, K. Murphy, A. Wang, R. Claus, and J. Greene. "Attometer resolution of wavelength shifts by use of fiber modal interferometers." *Optics Letters*, vol. 20, no. 97, 1995.

[35] Wikipedia. "Lorentz-Lorenz — Wikipedia, The Free Encyclopedia.", 2005. URL `http://en.wikipedia.org/w/index.php?title=Lorentz-Lorenz&old%id=16629823`. [Online; accessed 30-May-2006].

[36] D. Vukovic, G. Woolsey, and G. Scelsi. "Refractivities of SF_6 and SOF_2 at wavelengths of 632.99 and 1300 nm." *Journal of Physics D: Applied Physics*, vol. 29, pp. 634 – 637, 1996.

[37] Wikipedia. "Equation of state — Wikipedia, The Free Encyclopedia.", 2006. URL `http://en.wikipedia.org/w/index.php?title=Equation_of_state&oldid=55375425`. [Online; last accessed 30-May-2006].

[38] Y. Chung and U.-C. Paek. "Fabrication and performance characteristics of optical fibre gratings for sensing applications." *IEEE Transactions on Optical Fiber Sensors*, vol. 01, pp. 36 – 42, 2002.

[39] K. Hill and G. Meltz. "Fiber Bragg Grating Technology Fundamentals and Overview." *Journal of Lightwave Technology*, vol. 15, no. 8, pp. 1263 – 1276, August 1997.

[40] T. Erdogan. "Fiber Grating Spectra." *Journal of Lightwave Technology*, vol. 15, no. 8, pp. 1277 – 1294, August 1997.

[41] S. T. Lee, R. D. Kumar, P. S. Kumar, and C. P. G. Vallabhan. "Long period gratings in multimode optical fibers: application in chemical sensing." *Optics Communications*, vol. 224, no. 1, pp. 237 – 241, 2003.

[42] A. Pedersen. "Calculation of spark breakdown or corona starting voltages in non uniform fields." *IEEE Transactions on Power Apparatus and Systems*, vol. PAS-86, no. 2, pp. 200 – 206, February 1967.

[43] A. Pedersen. "Analysis of spark breakdown characteristics for sphere gaps." *IEEE Transactions on Power Apparatus and Systems*, vol. PAS-86, no. 8, pp. 975 – 978, August 1967.

[44] A. Pedersen. "Criterion for spark breakdown in sulfur hexafluoride." *IEEE Transactions on Power Apparatus and Systems*, vol. VPAS-89, no. 8, pp. 2043 – 2048, Nov/Dec 1970.

[45] J. Reynders. *Electrical Discharges in Gases*. School of Electrical and Information Engineering, University of the Witwatersrand, 2005. Lecture Notes.

[46] A. Pedersen. "The effect of surface roughness on breakdown in SF_6." *IEEE Transactions on Power Apparatus and Systems*, vol. PAS-94, no. 5, pp. 1749 – 1753, Sept/Oct 1975.

[47] M. Zhou, J. Reynders, and S. Nielsen. "The basic processes of gas breakdown." *Southern African Universities Power Engineering Conference*, vol. SAUPEC 96, pp. 5 – 8, 1996.

[48] M. Zhou and J. Reynders. "Synergy between SF_6 and other gases to enhance dielectric strength." *Proceedings of the 7th International Symposium of High Voltage*, vol. 7, August 1997.